Determination of the Ideal Gas Isobaric Heat Capacity of D4 using experimental speed of sound measurements

C.O.P van Weert

Technische Universiteit Delft

TU Delft

Cover image: Géraud Gordias `https://unsplash.com/photos/bNVbyBl870A`

Determination of the Ideal Gas Isobaric Heat Capacity of D4 using experimental speed of sound measurements

by

C.O.P. van Weert

to obtain the degree of Master of Science
at the Delft University of Technology,
to be defended publicly on Monday March 21, 2022 at 10:00 AM.

Student number:	4430158	
Project duration:	June 1, 2020 – March 21, 2022	
Thesis committee:	Prof. dr. ir. P. Colonna	TU Delft, Chair
	Prof. dr. ir. W. de Jong	TU Delft, Examiner
	Dr. ir. B.H. Mercier	TU Delft, Supervisor
	N.B. Chandrasekaran MSc.	TU Delft, Supervisor

Preface

This thesis marks the end of my student life In Delft, a vibrant period to which I always will look back on with a great smile. The many adventures and freedoms I have been able to explore during this period. Meeting many different people from all over the world and making a few good friends along the way. This been a period of growth, not only with great Aerospace knowledge but also as a person.

This thesis represents me as a person, as it provided me a challenge and a step outside my comfort zone by pursuing a theoretical study of thermodynamic properties. Therefore I would like to thank my supervisors Nitish Chandrasekaran and Bertrand Mercier for the guidance provided over last year and a bit.

Furthermore, I would like to thank my parents and my sister to always inspire me to continue with my studies also at times I was less motivated to do so. I want to thank my close group of high school friends, especially Ruben Tricoli for our diverse discussions on our trip to Poland of summer 2021. I want to thank my best friend in Delft, Bastiaan Bosman, with whom I will never walk alone. Finally, I want to thank my roommates who had to deal with some frustration from time to time when things didn't work out as planned.

Camille van Weert
Delft, March 2022

Summary

The research presented in this thesis regards the study of thermodynamic properties using speed of sound measurements of the substance Octamethylcyclotetrasiloxane, also referred to as D4. Through speed of sound measurements carried out in a box type acoustic resonator the ideal gas speed of sound is obtained. The ideal gas speed of sound is used to determine the ideal gas isobaric heat capacity. This thermodynamic property does not only provide valuable information for the formation of thermodynamic models, it is also used in this research to determine validity of these thermodynamic models. The measurements made in this research are at higher temperatures than the data used for the creation of the thermodynamic models, thus allowing for the validation of these models at temperatures that are relevant for ongoing research and engineering applications. The results presented in this thesis show that the thermodynamic models are qualitatively valid at these elevated temperatures. However, during the analysis of the experimental speed of sound data sensitivity problems were encountered with the conventional analysis method.

Therefore, this research also provides the development and the required verification and validation of an alternative analysis method, due to the high sensitivity to insignificant change in the speed of sound of the conventional analysis method. The conventional analysis method requires curve fitting of the measured speed of sound data to obtain the ideal gas speed of sound, before the ideal gas isobaric heat capacity can be obtained. Fitting errors are introduced through curve fitting, which lead to significantly large uncertainties due to the sensitivity of the method. The aim of the newly developed analysis method is to reduce the sensitivity to a fluctuation in the speed of sound. In order to achieve this, a numerical integration method developed by Trusler is modified such that it outputs the ideal gas isobaric heat capacity. This newly developed method is verified and validated for methane and altered such that it is can be used for the analysis of D4. The analysis with simulated experimental data for D4 reveals that this newly developed method does not provide the significant reduction in sensitivity that was aimed for. However, a reduction in discrepancies with respect to the conventional method are observed. These discrepancies are unrelated to the sensitivity towards a fluctuation in the speed of sound. Nevertheless, this does inspire confidence with regards to the application of the alternative method for the analysis of actual experimental data, as both the conventional method and alternative method show a similar sensitivity towards a speed of sound fluctuation. However, the alternative method shows better performance towards a realistic experimental data set. Furthermore, analysis presented in this research shows that this alternative method becomes more accurate at supercritical starting temperatures, which is a region for D4 that still requires analysis. A reflection on the experimental study is performed following the conducted sensitivity analysis of the alternative method for D4. This reflection reveals that the ideal gas isobaric heat capacity for D4 is inherently more sensitive towards a fluctuation in speed of sound, by comparing D4 to methane. Therefore, it is concluded that for D4 and other cyclosiloxanes highly accurate measurement devices are required.

Contents

List of Figures

List of Tables

Nomenclature

List of Symbols

α	Reduced Helmholtz energy	[-]
α^{IG}	Reduced ideal gas Helmholtz energy	[-]
α^{R}	Reduced residual Helmholtz energy	[-]
α_t	Thermal expansion coefficient	[1/K]
β_a	Second acoustic virial coefficient	[molm/N^2]
δ	Reduced density	[-]
δ_0	Reduced density, reference state	[-]
δ_a	Fourth acoustic virial coefficient	[molm^5/N^5]
ϵ	Non-dimensional specific heat	[-]
Γ	Fundamental derivative of gasdynamics	[-]
γ	Ratio of specific heats	[-]
γ^{IG}	Ideal gas ratio of specific heats	[-]
γ_a	Third acoustic virial coefficient	[molm^3/N^3]
$\mathcal{O}$	Truncation error	[-]
μ	Mean	[-]
ν	Specific volume	[m^3/kg]
ρ	Density	[kg/m^3]
σ	Standard deviation	[-]
τ	Reduced temperature	[-]
τ_0	Reduced temperature, reference state	[-]
a	Specific Helmholtz energy	[J/kg]
a^{IG}	Specific ideal gas Helmholtz energy	[J/kg]
a^{R}	Specific residual Helmholtz energy	[J/kg]
a_0	Mean linear expansivity coefficient	[1/mm]
A_n	Fitted coefficients	[-]
B	Second virial coefficient	[m^3/mol]
C	Third virial coefficient	[m^3/mol]
c	Speed of sound	[m/s]
c^{IG}	Ideal gas speed of sound	[m/s]

$C_{p,m}^{IG}$	Ideal gas isobaric molar heat capacity	[J/molK]
c_p	Isobaric specific heat capacity	[J/kgK]
c_p^{IG}	Ideal gas isobaric specific heat capacity	[J/kgK]
c_v^{IG}	Ideal gas isochoric specific heat capacity	[J/kgK]
cc	Calibration Constant	[-]
e_{fit}	Fitting error	[-]
$e_{\text{low,bnd}}$	Lower bound error	[-]
$e_{\text{std,ave}}$	Average standard error of experimental results	[-]
e_{tot}	Total error	[-]
$e_{\text{up,bnd}}$	Upper bound error	[-]
f	frequency	[Hz]
$f_{k,m,n}$	Resonance frequency modes	[Hz]
f_{max}	Maximum of the measured frequency peaks	[Hz]
g	Half width of the frequency	[Hz]
h^{IG}	Ideal gas specific enthalpy	[J/kg]
h_0^{IG}	Ideal gas specific enthalpy, reference state	[J/kg]
h_0	Resonator width at 273 K	[m]
k	Longitudinal mode number	[-]
k	Longitudinal resonance mode	[-]
$K_{n,1}$	First Runge-Kutta coefficient	[-]
$K_{n,2}$	Second Runge-Kutta coefficient	[-]
$K_{n,3}$	Third Runge-Kutta coefficient	[-]
$K_{n,4}$	Fourth Runge-Kutta coefficient	[-]
l	Length of resonator	[m]
l_0	Resonator length at 273 K	[m]
M	Molar Mass	[Kg/mol]
m	Radial resonance mode	[-]
n	Radial resonance mode	[-]
p	Pressure	[pa]
p_c	Critical pressure	[Pa]
PQ	Peak Quality	[-]
R	Universal gas constant	[J/molK]
s	Specific entropy	[J/kgK]
s^{IG}	Ideal gas specific entropy	[J/kgK]

s_0^{IG}	Ideal gas specific entropy, reference state	[J/kgK]
sf	Scaling Factor	[-]
T	Temperature	[K]
T_c	Critical temperature	[K]
u_{asy}	asymptotic speed of sound	[m/s]
V	Volume	[m^3]
Z	Compressibility factor	[-]

Acronyms

BZT	Bethe, Zel'dovich and Thompson
FAST	Flexible Asymmetric Shock Tube
IHE	Internal Heat Exchanger
MAD	Median Absolute Deviation
ORC	Organic Rankine Cycle
OVAR	Organic Vapour Acoustic Resonator
RSW	Rarefaction

1

Introduction

This thesis regards the study of thermodynamic properties using speed of sound measurements of the substance Octamethylcyclotetrasiloxane, also referred to as D4. Together with the substances D5 and D6 they form the family of cyclosiloxanes. These fluids are of interest for engineering applications involving heat recovery, due to their favourable thermodynamic and toxicological properties [2, 3, 12]. However, these fluids are not as widely studied as the standard monatomic and diatomic fluids, thus limited thermodynamic data is available for these fluids. This affects the development of thermodynamic models, which are used in the design of engineering applications, such as heat recovery. Furthermore, thermodynamic information is required with regards to the ongoing research on the topic of the formation rarefaction shockwaves at Delft University of Technology. This research also makes use of the thermodynamic models to determine experimental conditions.

The research of this thesis is initiated to gain a better understanding of these fluids and to determine the validity of the thermodynamic models. This thesis is not focused on proving the existence of rarefaction shockwaves, but focuses on the use of experimentally obtained speed of sound data so that the thermodynamic models can be verified for use in the region where these rarefaction shockwaves are predicted to occur.

This introduction provides a background to the research conducted in this thesis. Firstly, the effects of climate change, the contribution of aviation and the proposed integration of heat recovery systems is discussed in Sec. 1.1. Secondly, ongoing research regarding the cycloxiloxanes is discussed in Sec. 1.2. Thirdly, the theory of the formation of rarefaction shockwaves and motivation for this research is introduced in Sec. 1.3. This is followed by stating the research goals and questions in Secs. 1.4 and 1.5, respectively. The contributions to science of this thesis are given in Sec. 1.6. Finally, the structure of this thesis report is given in Sec. 1.7.

1.1. Climate change and the role of aviation

Humanity is facing one of the biggest problems it has encountered since the dawn of mankind in the form of man-made climate change. This is caused by the release of greenhouse gases into the atmosphere, mainly due to the combustion of fossil fuels. Change is required in the way transport is conducted, to reduce the emission of greenhouse gases into the atmosphere. This could result in a limitation to the climate change effects caused by these greenhouse gases. While the automotive industry is already undergoing a drastic switch to electric powered vehicles, the aviation industry is continuing with the development of fossil fuel powered aircraft. Small electric vehicles with distributed propulsion are being developed at this moment in time, and even a few fully electric aircraft exist today, albeit general aviation aircraft. Therefore, the most polluting sector in aviation, civilian aviation, remains in essence untouched [11, 42, 46] by this revolution for more sustainable transport. The jet engine developed through the 1950's into turbofan in 60's and 70's is being improved upon till this day. The state of the art in turbofan development is the GE9X engine for Boeing's latest twin-engine long-haul aircraft the Boeing 777x [27]. The development of this engine shows that still gains can be made with regards to efficiency of turbofan engines.

However, in order to reduce emissions caused by aviation in a fast-growing market, where more of China, India and South-East Asia will gain access to flying, more drastic measures need to be taken in order to reduce the total emissions caused by flying [1, 8]. One of such proposals is the introduction of heat recovery. Even though turbofans are one of the most efficient fossil fuel based engines, most of the energy released through combustion is emitted into the environment. By recovering this waste heat after the turbine of the engine, the total thermodynamic efficiency of the engine can be drastically improved. This heat recovery is not just a heat exchanger placed in the harmful environment of the jet exhaust, but requires also an entire system of piping, pumps, carrier fluid and a turbine itself. The development of the heat exchanger, turbines and system architecture are outside the scope of this study, which will mainly focus on the carrier fluids intended for these systems [47]. The proposed systems for waste heat recovery are Organic Rankine Cycle (ORC) systems.

The ORC follows the Rankine cycle, only the working fluid is changed from water to an organic fluid. By using an organic fluid instead of water allows for the adaptation of the Rankine cycle to a much wider range of applications and heat sources. This is advantageous, because it allows for better tailoring of the system to the operating temperatures. For example, an organic fluid with a lower boiling temperature allows for lower temperature heat sources, such as in solar power or geothermal applications [29]. Therefore, Colonna [14] mentions that an ORC system can be virtually applied to any external thermal energy source, as the temperature differences required for the heat exchanger ranges approximately from 30 to 500 °C [9].

The application of waste heat recovery in a turbofan engine is a high temperature application, which is one of the reasons why the mentioned siloxanes are being studied. The siloxanes D4, D5 and D6 have a boiling temperature higher than that of water and due to their molecular complexity, these fluids also have larger heat capacity than water, making it an ideal candidate fluid for high temperature ORC systems [4, 12, 20]. Furthermore, these substances are non-toxic and are widely used in cosmetic applications already[12, 20]. With regards to the environment, a study performed by the Dutch government proved that there was no acute toxicity caused by the siloxane D4 in open water [48].

In Fig. 1.1 the architecture of the standard Rankine cycle system is shown in Fig 1.1a, accompanied by the T-S diagram shown in Fig. 1.1b. The architecture of the Rankine cycle systems consists for four separate stations. The outlet of each station is numbered and corresponds to the numbered conditions shown in the T-S diagram. In Fig 1.1b the standard and super-heated Rankine cycle are indicated.

The Rankine Cycle starts at station 1, where the fluid enters the pump or compressor. This increases the pressure and temperature of the fluid isentropically before entering the boiler or heat exchanger in case of heat recovery. Station two indicates the inlet conditions of the boiler or heat exchanger. The addition of heat within the boiler is an isobaric process and the fluid undergoes a phase transition from liquid to vapour. The conditions at the outlet of the boiler, at station 3, are such that the fluid is a saturated vapour before entering the turbine. In the turbine the work is extracted and the fluid is expanded, resulting in a lower pressure fluid. Moving from station 3 to 4. The expansion in the turbine is also an isentropic process. The remaining heat within the fluid is then rejected in the condenser[44].

In Fig. 1.1b two different cycles are displayed. The standard Rankine cycle is indicated by the station numbers 1-2-3'-4' and the super-heated Rankine cycle indicated by station numbers 1-2-3-4. The standard Rankine cycle shows that the expansion occurs within the two-phase region, resulting in condensation throughout the expansion process in the turbine. The super-heated Rankine cycle increases the temperature of the vapour further, so that the two-phase region is avoided during expansion. This is favourable, because it reduces wear and tear on the turbine blades [4]. The architecture shown in Fig. 1.1a gives the most basic form of a Rankine cycle system, which can be expanded to include Internal Heat Exchangers (IHE), or regenerative heating between two turbines.

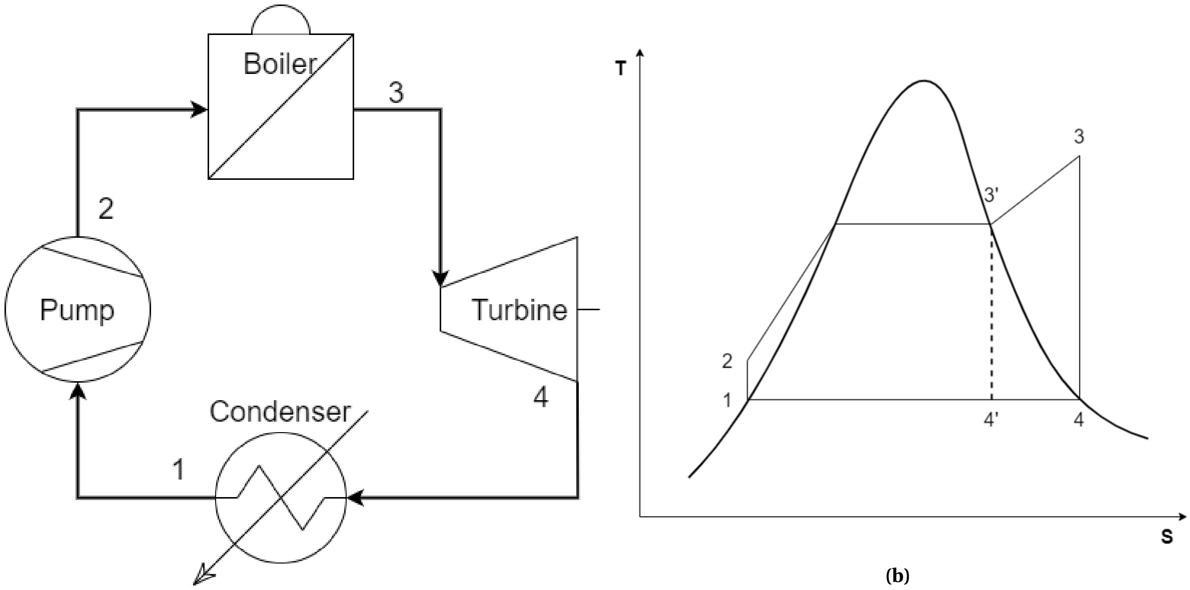

(a)

(b)

Figure 1.1: (a) General architecture of a Rankine cycle system (b) The T-S diagram belonging to the Rankine cycle shown in Fig. 1.1a. The figure indicates both the standard (3'-4') and super-heated steam cycle (3-4). The figure is adapted from Reddy [44].

1.2. Ongoing research on siloxanes

Even though the applicability of the cyclosiloxanes for ORC systems is a driver for this research, the main reason for conducting this research is to support the efforts undertaken at Delft University of Technology to prove the existence of Rarefaction shockwaves. These shockwaves, unlike classical shockwaves, show a static pressure decrease across the shock. Therefore, these shocks are also described as negative or expansion shocks, in contrast to the widely studied classical compression shock. However, rarefaction shockwaves have not been proven experimentally for a saturated vapour yet. Therefore, the rarefaction shockwaves remain a theoretical concept developed by Bethe [6].

The Asymmetric Shock Tube for Experiments in Rarefactions (ASTER) is a Ludwieg-type shock tube designed at the Propulsion & Power group at Delft University of Technology with the specific aim of demonstrating for the first time, the existence of these shocks in the single-phase vapour region of these so-called Bethe Zel'dovich Thompson (BZT) fluids. This set up is the successor of the Flexible Asymmetric Shock Tube (Fast), initially developed for the same purpose as FAST [30].

Bethe also observed that the behaviour of the shockwave formation was governed by the term $\left(\frac{\partial^2 p}{\partial v^2}\right)_s$. Thompson further developed this with the introduction of the fundamental derivative of gasdynamics [52, 53]. The fundamental derivative of gasdynamics is given by:

$$\Gamma \equiv -\frac{v}{2}\left(\frac{\partial^2 p}{\partial v^2}\right)_s \Big/ \left(\frac{\partial p}{\partial v}\right)_s = 1 - \frac{v}{c}\left(\frac{\partial c}{\partial v}\right), \tag{1.1}$$

where Γ is the fundamental derivative of gasdynamics, v is the specific volume, p the pressure and c the speed of sound. The term studied by Bethe is also recurring in the definition of the fundamental derivative of gasdynamics. The sign of the fundamental derivative of gasdynamics and therefore the type of shock is governed by the term $\left(\frac{\partial^2 p}{\partial v^2}\right)_s$, because the term $\left(\frac{\partial p}{\partial v}\right)_s < 0$ for every fluid. When the value for $\left(\frac{\partial^2 p}{\partial v^2}\right)_s > 0$ the fundamental derivative is larger than zero and the pressure change across the shock is larger than zero, indicating that the shock is a classical shock. For the situation where $\left(\frac{\partial^2 p}{\partial v^2}\right)_s < 0$, the fundamental derivative is smaller than zero and the observed pressure jump across the shock is also negative, therefore the shock is a rarefaction shock.

It is shown that the formation of the shockwaves requires the fundamental derivative of gasdynamics to be less than zero, which is not possible for every fluid. For a saturated vapour the conditions at which $\Gamma < 0$, is a small region close to the critical point on the vapour side of the saturation dome [13]. According to Bethe [6] and Thompson [53] the sign of $\left(\frac{\partial^2 p}{\partial v^2}\right)_s < 0$ is influenced by the sign of ϵ, where $\epsilon \equiv \frac{R}{c_v}$. In order for $\left(\frac{\partial^2 p}{\partial v^2}\right)_s < 0$, ϵ should be minimised, which requires maximising c_v for the fluid at hand. A factor that affects the heat capacity of a substance is the molecular complexity, a molecule that is more complex has more degrees of freedom to store energy, resulting in a higher heat capacity. Thus, achieving the feat of reducing R/c_v, becomes a quest of finding molecules with high complexity. Of the mentioned cyclosiloxanes, D5 and D6 are BZT fluids, meaning they belong to the group of large and high complex molecules suitable to achieve a region where $\Gamma < 0$.

1.3. Motivation of the research conducted

The research carried out in ASTER uses the fluids D5 and D6, because these belong to the BZT fluids. D4 does not belong to the BZT fluids, because it is not able to achieve a region of $\Gamma < 0$. However, it does have a region of $\Gamma < 1$, which also unlikely for the standard monatomic and diatomic gases. As is mentioned earlier this chapter, the region where $\Gamma < 0$ for a single-phase vapour is located close to the critical point [13]. In order to determine these conditions for experimental runs, thermodynamic models are utilised. Equations of state based on the Helmholtz energy are the state of the art in the development of thermodynamic models. Equations of state based on Helmholtz energy exist of two terms; an ideal gas term and a residual term. The Helmholtz equation of state is given by the following equation [50]:

$$\frac{a(T,\rho)}{RT} = \frac{a^{IG}(T,\rho) + a^{R}(T,\rho)}{RT} = \alpha^{IG}(\tau,\delta) + \alpha^{R}(\tau,\delta), \tag{1.2}$$

where a and α represent the specific and reduced Helmholtz energy respectively, the superscripts IG and R represent the ideal gas and residual terms. The terms R and T, represent the universal gas constant and temperature, respectively. Furthermore, the term τ represents the inverse reduced temperature $\tau = \frac{T_c}{T}$ and the term δ represents the reduced density, $\delta = \frac{\rho}{\rho_c}$. The ideal gas term of the Helmholtz energy equation of state is given by:

$$a^{IG} = h^{IG} - RT - Ts^{IG}, \tag{1.3}$$

where h and s represent the specific enthalpy and entropy. Reducing and rearranging of the terms on the right-hand side results in

$$\alpha^{IG} = \frac{h_0^{IG}\tau}{RT_c} - \frac{s_0^{IG}}{R} - 1 + \ln\left(\frac{\delta\tau_0}{\delta_0\tau}\right) - \frac{\tau}{R}\int_{\tau_0}^{\tau}\frac{c_p^{IG}}{\tau^2}\mathrm{d}\tau + \frac{1}{R}\int_{\tau_0}^{\tau}\frac{c_p^{IG}}{\tau}, \tag{1.4}$$

where the subscript 0 indicates the reference state and subscript c indicates the critical value.

The real gas term of the Helmholtz energy equation of state requires a reference equation. The most commonly used reference equation for this purpose is the Span-Wagner reference equation [50]. This equation is given by:

$$\begin{aligned}\alpha^{R}(\tau,\delta) = {} & n_1\delta\tau^{0.250} + n_2\delta\tau^{1.125} + n_3\delta\tau^{1.500} + n_4\delta^2\tau^{1.375} + n_5\delta^3\tau^{0.250} + n_6\delta^7\tau^{0.875} + \\ & n_7\delta^2\tau^{0.625}e^{-\delta} + n_8\delta^5\tau^{1.750}e^{-\delta} + n_9\delta\tau^{3.625}e^{-\delta^2} + n_{10}\delta^4\tau^{3.625}e^{-\delta^2} + n_{11}\delta^3\tau^{14.5}e^{-\delta^3} + \\ & n_{12}\delta^4\tau^{12.0}e^{-\delta^3}.\end{aligned} \tag{1.5}$$

The terms $n_1 - n_{12}$ are fluid specific and determined by a multi-parameter optimization of thermodynamic data of the fluid. These data are provided through experimental studies or different models. In the process of optimization these data are all considered and weighted according to their relative accuracy. The weighing of data is a critical step in the fitting procedure for technical equations. Usually, highly accurate data tend to be weighted such that their effect overshadows the less accurate data points. Causing certain regions to be represented overly accurately by the fitted equation, while the data points with reduced accuracy shows increased inaccuracy [49].

The conditions where $\Gamma < 0$ are outside of the region of data available used to generate the equation of state for the cyclosiloxanes. Therefore, it is unknown whether the models are valid at these increased temperatures. The main objective for this research is to identify if the thermodynamic models of D4, D5 and D6 are valid at increased temperatures, so that the conditions for the experiments in ASTER can be confidently determined with the use of these models. Furthermore, this research aims to provide new and accurate experimental data, that could be further used for the development of the equation of state.

1.4. Research goals of this thesis

In order to identify whether the thermodynamic models are still valid at increased temperatures the main research goal is to identify the ideal gas isobaric heat capacity through speed of sound measurements. The ideal gas isobaric heat capacity does not only provide for a direct comparison with the model data, it also provides thermodynamic data which can be used in the ideal gas term of the Helmholtz energy equation of state. This is especially applicable to the ideal gas term of the equation of state, given by Eq. 1.4. In this equation the ideal gas isobaric heat capacity is one of the variables in the equation.

The model used to identify the conditions for the experiments conducted in ASTER is RefProp and is based on the Helmholtz energy equation of state. Thus, this model is validated with the experiment conducted in this thesis. Due to the similarities between the three mentioned siloxanes, conclusions of the experiment conducted with D4 are also qualitatively valid. This saves time and effort by not repeating the same experiment for a different fluid, for which the results regarding the validation of the model would be of similar nature.

Besides the validation of the thermodynamic models, another goal of this thesis is to develop an alternative analysis method for analysing the ideal gas isobaric heat capacity from the speed of sound. The most commonly used analysis method for this type of analysis is sensitive to a change in measured speed of sound, leading to large uncertainty bounds for the experimental results. The goal of the newly developed method is to be less sensitive to a change in measured speed of sound. The basis of this alternative method is found in the numerical analysis approach created by Trusler [54]. Adaptations to this method are made so that the ideal gas isobaric heat capacity are obtained.

1.5. Research questions of this thesis

As the goals of this thesis are not only to validate the thermodynamic models, but also to develop an alternative analysis method, there are two sides two this thesis. The first part regards the experimental study and validation of the models. For this part of the thesis, the research question to be answered is as follows:

"What is the validity of the existing thermodynamic models when utilized outside the region of accurately available data used for the creation of the model?"

The second part of the thesis regards the development of an alternative analysis method. There are two research questions to be answered in this part. The first question regards the development of the alternative method:

"What are the steps required in order to determine the ideal gas heat capacity from speed of sound data using numerical integration, which can be applied to the analysis of experimental data?".

By answering this question not only a set of equations is provided, but also a methodology of setting up and analysing an experiment.

The second question regards the sensitivity of the newly developed method, as the goal of this method is to reduce this sensitivity. Thus, the research question required to be answered is:

"What improvement in sensitivity is achieved with the usage of the numerical method over the conventional method?"

In order to answer this question a sensitivity analysis of both the conventional and alternative method is required.

1.6. Thesis contributions to science

The main contributions of this research to science are not only limited by the validation of thermodynamic models or an alternative way to calculate the ideal gas heat capacity from speed of sound data. The experimental data obtained can be used in the improvement or development of thermodynamic models, if deemed accurate enough. Furthermore, the conclusions drawn for the validation of the models with the data for D4 are qualitatively valid for D5 and D6 due to similarity of the fluids. This research also provides new insights on the behaviour of D4 with regards to a change in the measured speed of sound, by performing of an extensive sensitivity analysis. This sensitivity analysis reveals that D4 is much more sensitive towards a fluctuation in the measured sound speed, when compared to methane.

The alternative method is developed so that a coherent approach is given to the reader on how to apply the method to experimental data. Unlike the conventional method, the several isotherms measured are used together to numerically determine the ideal gas isobaric heat capacity. Due to this connection between the several measured isotherms, it is beneficial to design the experiment with the methodology of this method in mind.

1.7. Report Structure

The report is structured as follows: Chapter 2 gives a background for speed of sound measurements in gases. This chapter provides the backbone of information required for performing and analysing the acoustic speed of sound experiment, as well as information required for the development of the alternative analysis method. Chapter 3 provides an overview of Organic Vapour Acoustic Resonator (OVAR) and description of the experimental methodology. In Chap.4 the post processing and analysis of the experimental data is discussed. This chapter introduces the mentioned formation of the asymptote for D4. Chapter 5 introduces the alternative analysis method requiring numerical integration adapted from the method by Trusler. In this chapter the steps required for the method are shown and the method is verified and validated for D4, using the data from Trusler [54]. This is followed by Chap. 6, where the previously developed method is adapted for D4 and a sensitivity analysis for both the conventional and newly developed alternative method is discussed. Chapter 7 concludes this thesis and provides recommendations for future research.

2

Speed of sound measurements in gases

This chapter provides an overview of speed of sound measurement techniques for gases. Firstly, in Sec. 2.1 the relevance of speed of sound measurements is established, by giving an overview of the thermodynamic data that can be obtained from the speed of sound measurements. This thermodynamic data can be obtained for both the ideal and real gas case. Secondly, an overview of various speed of sound measurement techniques is given in Sec. 2.2. Which is followed by an in-depth discussion on acoustic resonators resonators given in Sec. 2.3.

2.1. Importance of speed of sound data

The discussion presented in this section introduces the relevance for performing speed of sound measurements. Speed of sound data is a valuable source of thermodynamic data, especially for the ideal gas isobaric heat capacity. This is relevant to the research conducted in this thesis, because the validation of the models is done using the ideal gas isobaric heat capacity. Furthermore, the ideal gas isobaric heat capacity provides useful data for the generation of those models. The focus of the discussion presented in this section is not only limited to obtaining the ideal gas heat isobaric capacity, but also to other real and ideal gas properties.

2.1.1. Obtaining the ideal gas isobaric heat capacity

In Sec. 1.4 the value of the ideal gas isobaric heat capacity was briefly discussed. It was shown that c_p^{IG} is not only required for the validation of the models, it also is of use for generating equations of state. The research conducted by Nannan [40] for D4 and D5 is of interest, due to the fact that the ideal gas isobaric heat capacity is obtained from speed of sound measurements. This is similar to the experiment conducted in this research. The methodology and analysis procedure as conducted by Nannan is also adhered to in this research, because of the similarity between the experiments.

The methodology used by Nannan is not only applicable to D4, it is also used by Trusler [54] for the analysis of CH4. This forms a conventional method for ideal gas analysis using speed of sound data [17, 26, 40, 54]. This conventional analysis method forms a relation between the measured speed of sound and pressure to extrapolate to the ideal gas conditions. This is done, because the ideal gas conditions cannot be directly measured. This relation is obtained through polynomial fitting of the measured speed of sound data and the pressure. As a result, the acoustic virial equation of state is obtained, which is given by:

$$c = c^{IG}\left[1+\left(\frac{\beta_a(T)}{RT}\right)p+\left(\frac{\gamma_a(T)}{RT}\right)p^2+\left(\frac{\delta_a(T)}{RT}\right)p^3+\dots\right], \tag{2.1}$$

where β_a, γ_a and δ_a represent the second, third and fourth acoustic virial coefficients and p represents the pressure. The acquired acoustic virial coefficients can be related to the virial coefficients for the virial equation of state. In the research conducted by Nannan, the speed of sound data is fitted such that the second and third acoustic virial coefficients are obtained. This means that the experimental data is fitted to a second order polynomial. A similar approach is taken as the experiment carried out by Nannan, because the experiment conducted in this thesis and Nannan's experiment are closely related. The second, third and fourth virial coefficients are not of value for the ideal gas analysis, but can be used to determine the virial equation of state. Obtaining the ideal gas conditions requires $p \rightarrow 0$, which reduces Eq. 2.1 to $c = c^{IG}$. This shows that through fitting of the experimentally obtained speed of sound the ideal gas speed of sound is obtained. The ideal gas isobaric heat capacity is then determined from the ideal gas speed of sound by applying:

$$c_p^{IG} = \frac{(c^{IG})^2 M}{T\left[\frac{(c^{IG})^2 M}{RT} - 1\right]}, \tag{2.2}$$

which provides accurate results for the ideal gas heat capacity, if accurately available data has been obtained.

2.1.2. Other thermodynamic properties obtained with speed of sound data

Even though the focus of this thesis is on the analysis of the ideal gas isobaric heat capacity, the use of speed of sound data is not only limited to ideal gas isobaric heat capacity. The universal gas constant can also be obtained through acoustic speed of sound experiments as demonstrated by Moldover [36]. The experimental study conducted by Moldover reduced the uncertainty of the universal gas constant with a factor of 5, resulting in an uncertainty of 1.7 ppm. Even though the gas constant can be simply obtained through different experiments as described in [39], Moldover's results show that highly accurate data can be obtained through acoustic measurements, not only for the universal gas constant but also different thermodynamic properties. This is because the ideal gas data originates from the same method. Moldover uses Argon gas to acoustically obtain the speed of sound to determine the universal gas constant. The universal gas constant is obtained from the speed of sound using the following relation:

$$R = \frac{(c^{IG})^2 M}{T\gamma^{IG}} = \frac{1}{T}\left(\frac{f_{0,n}}{\nu_{0,n}}\right)^2 V^{2/3}\frac{M}{\gamma^{IG}}, \tag{2.3}$$

where in the utmost right-hand term $\nu_{0,n}$ is a known eigenvalue of the substance, $f_{0,n}$ represents the radial mode, M the molar mass of the substance, γ^{IG} the ideal gas ratio of specific heats and V represents the volume.

The ideal gas speed of sound data can further be used to determine temperature scales. Secondary thermometers such as thermocouples and platinum resistance thermometers require calibration using accurate temperature data. The act of acquiring this accurate temperature data is defined as primary thermometry. One method of obtaining this data is through the ideal gas speed of sound. Likewise for the analysis of the universal gas constant, the temperature is obtained by rewriting Eq. 2.3 and knowing the ideal gas speed of sound and the ratio $\frac{R\gamma^{IG}}{M}$. The speed of sound is obtained using fitting of experimental data to a polynomial function. For well-studied mono-atomic gases, such as argon, the values for γ^{IG} are well researched, while for the mentioned siloxanes these values possess larger uncertainty. According to Benedetto [5], acoustic thermometers can be accounted for the development of the sub 20 K temperature scales suitable for practical applications and have revealed errors in the internationally used temperature scales IPTS-68 and ITS-90.

Besides obtaining thermodynamic properties of an ideal gas, the speed of sound data can also be used for obtaining thermodynamic properties of a real gas. Related to the ideal gas isobaric heat capacity is real gas isobaric heat capacity, which can be obtained using the same speed of sound data as for obtaining c_p^{IG}. Obtaining c_p from the speed of sound requires numerical integration as is described by Benedetto [5], Trusler[54] and Estrada-Alexanders [17]. The method presented by these studies requires the solving of

$$c_p = \left[\frac{M}{R}\frac{\left(Z - p\left(\frac{\partial Z}{\partial p}\right)_T\right)}{\left(Z + T\left(\frac{\partial Z}{\partial T}\right)_p\right)^2} - \frac{TZ^2}{c^2\left(Z + T\left(\frac{\partial Z}{\partial T}\right)_p\right)^2}\right]^{-1}, \tag{2.4}$$

and

$$\left(\frac{\partial^2 Z}{\partial T^2}\right)_p = -\frac{Mp}{RT^2}\left(\frac{\partial c_p}{\partial p}\right)_T - \frac{2}{T}\left(\frac{\partial Z}{\partial T}\right)_p, \tag{2.5}$$

simultaneously. These equations are expressed in terms of the compressibility factor, Z, due to its reduced fluctuation to temperature changes. Solving of Eq. 2.4 requires the initial conditions of Z and $\left(\frac{\partial Z}{\partial T}\right)_p$ along the starting isotherm. These values are determined from thermodynamic models or by interpolation of reference data. Knowing Z along the starting isotherm allows for the differentiation of Z with pressure, resulting in $\left(\frac{\partial Z}{\partial p}\right)_T$ required for solving Eq. 2.4. The value obtained for c_p is then differentiated with pressure along the isotherm to obtain $\left(\frac{\partial c_p}{\partial p}\right)_T$. This differential is then used in Eq. 2.5 to obtain $\left(\frac{\partial^2 Z}{\partial T^2}\right)_p$, which is required for integration to determine the conditions at $T + \mathrm{d}T$. Trusler and Estrada-Alexanders use Euler integration accurate to the second order to determine the starting conditions for the next isotherm. The integration of Z is performed with scheme shown below:

$$Z_{n+1} = Z_n + \mathrm{d}T \left(\frac{\partial Z}{\partial T}\right)_{p,n} + \frac{1}{2}\mathrm{d}T^2 \left(\frac{\partial^2 Z}{\partial T^2}\right)_{p,n}. \tag{2.6}$$

The term $\left(\frac{\partial Z}{\partial T}\right)_p$ is integrated by using the following scheme:

$$\left(\frac{\partial Z}{\partial T}\right)_{p,n+1} = \left(\frac{\partial Z}{\partial T}\right)_{p,n} + \mathrm{d}T \left(\frac{\partial^2 Z}{\partial T^2}\right)_{p,n}. \tag{2.7}$$

This method can also be used to determine the density of a fluid from the speed of sound data. This requires c_p to become an initial value instead of Z, because Z is related to the density via

$$Z = \frac{Mp}{\rho R T}. \tag{2.8}$$

This can also be obtained by using the method introduced in Sec. 2.1.1, using the obtained acoustic virial coefficients to determine the second and third virial coefficients to acquire the virial equation of state. The second acoustic virial coefficient by

$$\beta_a = 2B + 2(\gamma^{IG} - 1) T \frac{\mathrm{d}B}{\mathrm{d}T} + \frac{(\gamma^{IG} - 1)^2}{\gamma^{IG}} T^2 \frac{\mathrm{d}^2 B}{\mathrm{d}T^2}. \tag{2.9}$$

The third virial coefficient is related to the third acoustic virial coefficient

$$\begin{aligned}\gamma_a = \frac{1}{RT}&\left[\frac{1+2\gamma^{IG}}{\gamma^{IG}} C + \frac{(\gamma^{IG})^2 - 1}{\gamma^{IG}} T \frac{\mathrm{d}C}{\mathrm{d}T} + \frac{(\gamma^{IG} - 1)^2}{2\gamma^{IG}} T^2 \frac{\mathrm{d}^2 C}{\mathrm{d}T^2}\right] \\ &- \frac{1}{RT}\left[B\beta_a - \frac{\gamma^{IG} - 1}{\gamma^{IG}}\left(B + (2\gamma^{IG} - 1) T \frac{\mathrm{d}B}{\mathrm{d}T} + (\gamma^{IG} - 1) T^2 \frac{\mathrm{d}^2 B}{\mathrm{d}T^2}\right)^2\right].\end{aligned} \tag{2.10}$$

Increasing the fitting order, more acoustic virial coefficients can be obtained, but the equations relating the acoustic virial coefficient to the virial coefficients become increasingly more complex as seen by these two relations.

2.2. Overview of speed of sound experiments

This section provides an overview of the various measurement techniques available to obtain the speed of sound of a fluid. The discussion in this section is not only limited to the state of the art, but also proposed measurement techniques using light to measure the speed of sound are discussed.

2.2.1. Acoustic resonators

The most commonly used method for obtaining speed of sound data in vapours and gases is through acoustic resonators, this method can be considered a traditional method in speed of sound research and resonators are used by many authors [17, 18, 34–37, 40, 54]. Even though resonators differ in geometry and size, the working principle is the same for all. All acoustic resonators possess a cavity filled by a vapour or gas of interest. The fluid inside the resonator is excited by the actuation of a membrane at a certain frequency. Depending on the frequency of the membrane the fluid inside the cavity starts resonating. Resonance of the fluid results in an increase of the measured pressure signal. By applying a Fourier transform on the measured pressure signal the resonance frequency is obtained by observation of a resonance peak. For highly accurate resonators a direct link between the measured frequencies and thermodynamic properties can be made. The speed of sound of the fluid at the prescribed temperature and pressure conditions is obtained by relating the observed resonance frequency with the geometry of the resonator.

2.2.2. Pulse-echo method

The pulse-echo method is another traditional speed of sound method. This technique measures the time of flight of the signal across a known distance. Unlike the acoustic resonators, which require a conversion of the frequency data into sound speed data, this method provides the speed of sound directly by dividing the distance over the measured time. This method is mainly used for obtaining the speed of sound in the liquid phase, whereas acoustic resonators are used for vapours and gases [33]. The main reason acoustic resonators are mainly used for vapours, is due to the large difference in acoustic impedance between the wall and vapour. This allows for an efficient reflection of the sound waves, resulting in more accurate results [22].

2.2.3. Brillouin light scattering and laser-induced thermal acoustics

The acoustic resonator and pulse-echo techniques make use of an electronically driven membrane to emit a signal through the fluid. However, this is not the only method that is applied for measuring the speed of sound. The usage of light for speed of sound measurements is a promising development in this field of research. Brillouin light scattering is a method using light, which has produced promising results. This technique makes use of the Brillouin components of the scattered light. Brillouin components are two peaks in the light spectrum that are symmetrical around the Rayleigh peak. The observed shift in frequency between the Brillouin and Rayleigh peak is used to obtain the speed of sound [58].

2.2.4. Photo-acoustic effect for speed of sound measurements

The photo-acoustic effect was first discovered by Bell in 1880. Bell described the generation of sound waves on a material through excitation by a pulsated or modulated source of light. The generation of this sound wave can be applied to speed of sound measurements for solids, as described by Hussein [24]. Besides speed of sound measurements for solids, the photo-acoustic effect is also applicable to speed of sound research for vapours and gases. Suchenek [51] designed an experimental set-up which used the photo-acoustic effect, as a means of signal generation for acoustic resonator measurements. The photo-acoustic effect is used as a signal generation application instead of using an electro-mechanically driven membrane, producing the acoustic waves. In the designed experiment the cavity featured two windows placed on the optical axis of the resonator. By covering one of these windows with carbon black, strong light absorption can be expected. Through pulsating LED light, this blacked out window is excited to produce a photo-acoustic signal. The signal is transmitted because of the direct contact between the fluid and the photo-acoustically excited window. Through this signal, resonance frequencies can be measured, comparable to the acoustic resonators discussed earlier this section.

2.3. Resonators in detail

Section 2.2 gave an overview of the different speed of sound measurement techniques. It is clear that the use of acoustic resonators is the traditional and most commonly used method for measuring the speed of sound in a vapour. Furthermore, due to the presence of a resonator at Delft University of Technology this technique is also used in the conducted experiment. Therefore, this section elaborates on the acoustic resonators, focusing on the geometry, location of transducers, thermal control and measurement procedure

2.3.1. Resonator geometry

The three main resonator geometries present in literature [25] are: spherical resonators [18, 19, 35–37, 43, 54], cylindrical resonators [40] and cuboid resonator [34]. The geometry of an acoustic resonator influences the measured resonance modes of the experiment. For example, the box type resonator available in the lab at Delft University of Technology mainly uses the longitudinal modes, due to the large difference in length compared to width and height [34]. The radial modes are mainly used in spherical resonators and provide several advantages over longitudinal modes. The radial resonance modes have a high-quality factor, meaning the damping of the signal is low. This allows for smaller pressure transducers in the shell, resulting in less imperfections to the geometry [35]. Furthermore, the radial modes are less susceptible to imperfections to the geometry, therefore requiring smaller correction compared to longitudinal modes [43]. This reduced susceptibility to geometrical imperfections allows for less strict tolerances during manufacturing [35]. Moreover, Moldover [35] specifies another advantage of using the radial modes which is caused by the nondegenerate nature of these modes, allowing the measured resonances to be directly interpreted as thermodynamic properties of the measured substance. Besides the advantages of spherical resonators, other geometries exist due to ease of manufacturing [57]. Nannan [40] describes that both radial and longitudinal modes were measured. Furthermore, Nannan measured redundant modes, in order to distinguish between the modes that have been measured. This is not a problem for the OVAR used during the experiments conducted in this thesis, because the length is much larger than the width and height of the resonator. This results in much larger frequencies measured for longitudinal modes than for radial modes.

2.3.2. Requirements and location for placing pressure transducers

In order to perform the measurements, transducers are required to emit and receive the signal. The size and location of these transducer affect the accuracy of the measurements. Goodwin describes five criteria required for transducers [22]:

1. The transducers should have a high acoustic impedance to the gas. Therefore, the transducer is required to respond differently to the vibrations compared to the gas, thus reducing the interference of potential resonance of the transducer on the resonance measurement.
2. The transducers should only be a small fraction of the cavity's surface area. This reduces the imperfections to the geometry, which is a source of error.
3. The transducers should have a low power dissipation. Therefore, the thermal equilibrium within the cavity is preserved, such that no specific areas of large temperature fluctuations are present within the gas
4. The transducers are able to operate within the harmful temperature and pressure range, while providing the right frequency range needed for the experiment.
5. The transducers should be chemically inert. Therefore, they should not react with the fluid. Otherwise, perturbations to the results are introduced, caused by the created impurities.

Besides adhering to these requirements, the placement of the transducers can play a role in reducing interference of different modes. This is shown by Mondejar [37] and Perkins [43], the transducers are spaced apart with an angular separation of 90° to reduce the effect of interference on radial and longitudinal resonance modes. The same angular separation is seen for the resonator used by Moldover [35]. A peculiar location for the transducers is observed for the resonator used by Nannan [40]. The transducers of this resonator are located outside of the resonator and connected with acoustic wave guides, shown in Fig. 2.1. The reason for this choice is related to the heating mechanism of the cavity. The cavity is placed inside of a stirred thermal bath. The conditions surrounding the cavity were considered harmful towards the transducers. These could not be placed outside of the cavity, inside the thermal bath. Furthermore, no significant effect to the accuracy of the results was observed by locating the transducers in this manner. Regarding the resonator present in the lab, the transducers are located on opposite ends of the length of the transducer, optimizing for the measurement of the longitudinal modes.

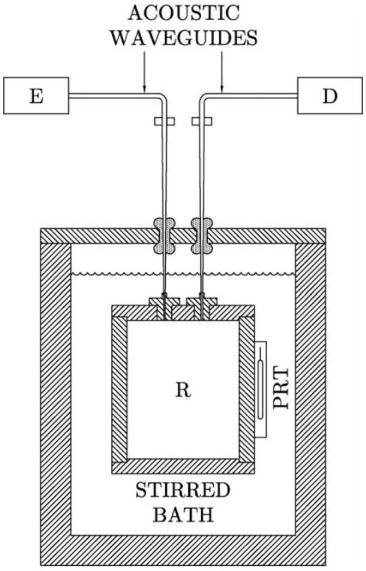

Figure 2.1: Cross section of the resonator used by Nannan [40]. The transducers are located outside of the whole experimental set up and connected to the cavity with acoustic waveguides.

2.3.3. Thermal control

Using acoustic resonators for speed of sound measurements requires the substance to be in a vapour state. For many of the studied substances this requires heating, which is also the case for the experiment with D4. In the previous subsection the stirred bath for the resonator used by Nannan [40] and Moldover [36] was briefly mentioned. This method submerges the resonator cavity in a thermal bath, which heats the walls of the cavity resulting in a gradual heating of the fluid inside the cavity. According to Nannan [40], this method allows for a good temperature stability and achieves a fast thermal equilibrium. The limited temperature range that can be measured is the major disadvantage of these types of resonators. The temperature limit for the speed of sound measurement conducted by Nannan for D4 is 495K.

Mondejar [37] used the resonator described by Perkins [43], which features an electronic heating system through copper encapsulating the spherical cavity so that the entire surface area receives heating. This is done to reduce the temperature gradients in the cavity. The Organic Vapor Acoustic Resonator (OVAR), is the resonator available for the speed of sound measurement for D4 at Delft University of Technology [34]. The OVAR also uses electronic heating, but differs from the copper capsule described before. Instead, four copper pads are placed on top of an aluminium cast, which encapsulates the stainless steel cavity. This aluminium cast has the same function as the copper capsule of Perkins' resonator and provides a more equal temperature distribution to the cavity, resulting in lower temperature gradients. Even though the heating methods differ, a set of requirements is obtained. By applying an equal temperature distribution to the cavity, thermal gradients are reduced. Furthermore, the system requires fast thermal equilibrium and thermal stability.

2.3.4. Measurement procedure

Even though the fluids analysed the mentioned studies differ, a common measurement procedure is deduced. A frequency sweep is performed around the resonance centre frequency, f. The interval of the sweep is denoted by g, which represents the half-width. The half width is determined as the width of the frequency of the signal at which the amplitude is $2^{-1/2}$-times the maximum amplitude of the signal [40]. The measured frequencies range from $f-g$ to $f+g$. For a box type resonator, such as the OVAR, the centre frequency is obtained by

$$f_{k,m,n} = \frac{c}{2}\sqrt{\left(\frac{k}{l_0}\right)^2 + \left(\frac{m}{h_0}\right)^2 + \left(\frac{n}{h_0}\right)^2}, \tag{2.11}$$

where $f_{k,m,n}$ indicates the frequency measured for the specific modes. k, m and n are the longitudinal and two radial modes, respectively. l_0 and h_0 are the length and height of the resonator at 273 K, respectively. Knowledge on the geometry and modes measured result in the measured frequencies. The speed of sound in Eq. 2.11 can be obtained through thermodynamic models. Because of the significant difference between the length compared to the width and height of the OVAR, Eq. 2.11 can be reduced to

$$f_k = k\frac{c}{2l_0}, \tag{2.12}$$

allowing for a fast estimation of the centre frequencies for the experiment.

A feature of working with fluids under increased temperature is decomposition of the fluids, resulting in increased impurities within the test fluid, affecting the speed of sound measurements. Mondejar [37] solves this problem by evacuating the fluid after and purging the resonator for remnants of the decomposed fluid. Besides, extensive purging of the fluid, corrections for impurities can be applied as mentioned by Nannan [40].

2.3.5. Perturbations

For speed of sound measurements several perturbations can affect the results of the measurements, these perturbations are:

- Condensation causes the formation of liquid drops sticking to the wall. This results in a non-zero normal fluid velocity, due to an oscillating temperature and pressure field at the wall. The effects of condensation are primarily of a concern for the determination of the acoustics virial coefficients, which is a potential source of error for obtaining the ideal gas heat capacity through the speed of sound. However, condensation does not affect obtaining the ideal gas speed of sound, according to Goodwin [22]. The effects of condensation can be avoided by keeping a margin between saturation conditions and refraining from using low frequency measurements [23].

- Impurities in the fluid alter the measured speed of sound by either increasing or decreasing its value, dependent on speed of sound of the fluid being studied and the speed of sound for the impurities. Impurities have several sources of origin. The three main sources of impurities mentioned in literature are as follows: the supplier, mixing with left over fluid from a different experiment using the same equipment and due to decomposition [40, 43, 54].

- Imperfect geometry influences the frequencies that are being measured as well is inducing slight errors in the determined speed of sound. Equation 2.11 shows that minor changes in dimensions of the OVAR result in an altered speed of sound. Sources of imperfections to the geometry are caused by production, the presence of transducers and inlet ports for the fluid. Goodwin [22] states five criteria for placing the transducers, which were previously mentioned in Subsec. 2.3.2.

- Shell motion is caused by the elastic deformation of the resonator walls due to minor pressure fluctuations. These deformations affect the measured frequencies, by causing a shift of frequencies leading to errors in the speed of sound values. The effect of shell motion is proportional to ρc^2 for frequencies located far away from the wall. Higher gas pressures increase the effect of the shell wall motion [21, 22]. Mehl [32] states that the correction for the shell is one of the most important corrections to be performed on speed of sound measurements, with the correction becoming more prominent for higher density gases.

- Formation of boundary layers is an inevitable effect of the interaction between the fluid and the wall. Both thermal and viscous boundary layers are formed separately from each other and have a different thickness. However, both boundary layers have an effect on the measured frequencies, with the boundary layer effect being proportional to $(f\rho)^{-1/2}$. This results in the effect of the boundary layers becoming stronger at low density and low frequency [22].

- Molecular thermal relaxation is a potential source of systematic error in the acoustic speed of sound measurements. This occurs when measurements are performed at frequencies that are low compared to the inverse of the relaxation time. The effect of molecular relaxation is observed as dispersion and attenuation of the sound. Molecular relaxation affects the frequencies due to absorption of the sound, causing a shift in measured frequencies. The thermal relaxation time influences the behaviour of the fluid, which is dominated by the transfer of energy from translational modes to the vibrational modes. A molecule requiring a large number of collisions to dampen out the vibrations, results in a long molecular relaxation time compared to the acoustic cycle leading to a significant amount of dispersion on the signal.

2.4. Summary

The discussion presented in this chapter gives insight into methods of measuring the speed of sound of a fluid can be measured. Sec. 2.2 showed the various different methods available of measuring the speed of sound of the fluid. Furthermore, it was shown that the use of acoustic resonators is the standard approach for a vapour, which is the case for the experiment carried out in this thesis. Section 2.3 elaborated on the working of acoustic resonator, highlighting the different type of acoustic resonators found in the literature and indicating the measurement procedure and perturbations. This gives insight on how the speed of sound of a vapour like D4 can be measured and what approach should be taken in order to obtain useful results, with regard to the ideal gas analysis.

Besides the experimental section the analysis phase of the speed of sound data was addressed. Section 2.1.1 showed how the ideal gas isobaric heat capacity should be obtained from the measured speed of sound data by obtaining the ideal gas speed of sound and the use of Eq. 2.2. In addition to the analysis of the ideal gas isobaric heat capacity, Sec. 2.1.2 discussed the other properties that can be determined from the speed of sound data. The other thermodynamic properties and data discussed in this section are the universal gas constant, temperature scales, isobaric heat capacity, the density and the virial coefficients for the virial equation of state. This shows the value of speed of sound measurements, because other thermodynamic properties can be obtained through the derivation of the virial equation of state.

3

The Organic Vapour Acoustic Resonator and methodology

This chapter features the experimental preparation and methodology for the acoustic speed of sound measurement experiment conducted for D4. An overview of the proposed experiment for D4 is given in this chapter in combination with the accompanying goals of the experiment. Furthermore, a detailed overview of the resonator used is provided.

This chapter is structured as follows. In Sec. 3.1 the OVAR is elaborately discussed. Focusing on the measurement conditions that can be attained as well as the determination of the speed of sound from the obtained frequencies. This is followed by Sec. 3.2, where the design and experimental methodology is discussed. This chapter is finalized with a summary, given in Sec. 3.3

3.1. The Organic Vapour Acoustic Resonator

The device used for the Experiment is the OVAR. It is a box type resonator, present at the propulsion and power group at the faculty of aerospace engineering at Delft University of Technology. The OVAR is especially designed for speed of sound measurements for the cyclosiloxanes D4, D5 and D6. In order to improve the thermodynamic properties of these gases.

A cross section of the OVAR is shown in Fig. 3.1 the inner casing of the OVAR is made from a machined block of stainless steel 316L, closed off with a stainless steel lid. The entire casing is then covered by a 10 mm thick aluminium shell, to provide a sufficiently homogeneous temperature spread along the stainless steel casing. This is done with aluminium because of its higher thermal conductivity. The aluminium shell is heated by four electric heating pads delivering 50 W each, the listed accuracy of these pads is ±0.1°C up to 400°C, more specific design features can be found in [34].

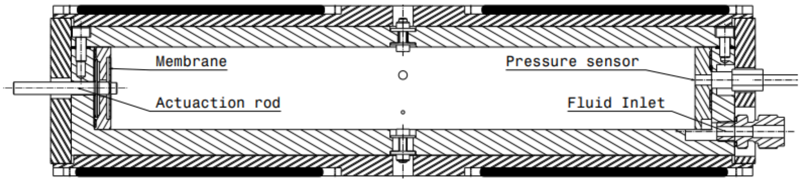

Figure 3.1: Cross section of the OVAR, obtained through Mercier [34]

In order to excite the fluid within the cavity, an acoustic signal is transferred into the gas. The signal is transferred to the gas through a thin membrane on one of the end caps of the resonator, capable of producing a frequency up to 600 Hz. This membrane is attached to an actuator rod and is located on the left-hand side of Fig. 3.1. The receiving pressure sensor is mounted on the opposite end cap and is capable of withstanding temperatures up to 500°C. On this side the fluid inlet port is also located, which is attached to a hand operated syringe. With this syringe the amount of fluid within the cavity is controlled. Therefore, the hand pump is able to alter the density within the cavity, which results in a change of pressure of the vapour. The fluid inlet port is a small imperfection to the geometry of the resonator, which causes slight perturbations to the measured frequency and should be accounted for.

Three resonant modes can be observed within the OVAR. One longitudinal and two radial modes, represented by the letters k, m and n respectively. The measured frequency is related to the sound speed by the following relation

$$f_{k,m,n} = \frac{c}{2}\sqrt{\left(\frac{k}{l_0}\right)^2 + \left(\frac{m}{h_0}\right)^2 + \left(\frac{n}{h_0}\right)^2}. \tag{3.1}$$

If the longitudinal length is significantly larger than the width and height of the end caps and longitudinal modes are being measured which do not overlap with the radial modes, this relation can be simplified to Eq. 3.3. For the OVAR it has been established that this Eq. 3.3 is valid, when modes $k \leq 6$ are being measured [34]. This reduced relation is given by Eq. 3.2, which is reordered to determine the centre frequencies for every pressure point.

It was seen that the geometry of the cavity is of importance for determining the speed of sound from the measured frequency data. Therefore, the effects of thermal expansion should be considered. Since the temperatures of the experiment will be up to 330°C, the change in dimensions due to thermal expansion are significant enough to alter the measured results. The effects of thermal expansion are included by rewriting of Eq. 3.3, resulting in

$$c = \frac{2l_0(1+\alpha_t T)f_k}{k}, \tag{3.2}$$

where $\alpha_t \approx 17 \cdot 10^{-6} K^{-1}$ for the stainless steel casing.

3.2. Experimental design and methodology

This section describes the design and methodology of the experiment. Furthermore, an overview of the actual measured data points is given, for which the discrepancies with the proposed cases are discussed. It should be noted that due the circumstances regarding the ongoing corona virus, the experiment was not carried out first hand by the author.

3.2.1. Experimental background

The experiment conducted in this thesis regards the fluid D4. D4 belongs to the family of cyclosiloxanes, to which D5 and D6 also belong. Due to their thermodynamic and toxicological properties these fluids interesting for ORC applications. Furthermore, D5 and D6 are candidate BZT fluids, meaning that these fluids possess a region where Γ becomes negative. This is a condition required for the formation of rarefaction shockwaves [52, 53], as was mentioned in the Chap. 1.

The experiment carried out in this research is not aimed at proving the existence of RSWs. Rather, this thesis is aimed at providing an answer to a supporting question to that research, namely whether the existing models can correctly predict the thermodynamic state at higher temperatures. Furthermore, this thesis aims at providing new thermodynamic data for D4 as well as discover new insights regarding the sensitivity of D4. The main question of the experimental section is related to the validity of these thermodynamic models. If the models deviate significantly from the experimental results, steps should be undertaken in order to create more accurate models. The validation of these models will be conducted by performing an acoustic speed of sound experiment, through which the ideal gas isobaric heat capacity can be obtained. This is similar to the experiment carried out by Nannan [40] for the fluid D4.

3.2.2. Proposed experiment

The proposed experiment acts as a continuation of the experiment performed by Nannan, wherein measurements are made at higher temperatures than the maximum isotherm studied by Nannan. The isotherm at 495 K has been measured by Nannan and is measured again to serve as a calibration point. This allows for the removal of the systematic error from the entire data set. It is known that the OVAR is able to sustain temperatures up to 670K and pressures limited to 10 bar. Thu,s the OVAR allows for the acquisition of the supercritical data, which provides helpful information on the validity of the models at these higher temperature regions. Especially regarding the isotherms where the admissibility region for RSWs occurs.

Even though the OVAR allows for the analysis of a pressure range up to 10 bar, Nannan [40] suggests that the measurements should be conducted for a more limited pressure range. The first suggestion made by Nannan is to set the lower limit at 0.3 bar, due to the increased noise-to-signal ratio at lower pressures.

The second suggestion made by Nannan is to set the upper pressure limit at 80% of the saturation pressure for the subcritical isotherms. For the design of this experiment these suggestions were adhered to, because the measured temperature range features both sub and supercritical isotherms, as $T_c \approx 585$ K,[31, 56]. For supercritical isotherms, the saturation effects do not exist, which enables the entire pressure range of the OVAR to be used. However, for the sake of the homogeneity of the entire experiment these pressure ranges will be limited to 1.6 bar.

More importantly, measurements at higher pressures are not of interest for the analysis of the ideal gas component of the speed of sound. In order to obtain the ideal gas speed of sound, fitting of the speed of sound and pressure data is required so that the ideal gas component can be obtained through extrapolation. This is required, due to the fact that at pressures below 0.3 bar highly accurate measurements are not possible, due to the increase of noise. Because of the interest in the ideal gas point, $p \to 0$, accurate data in the lower pressure region is more valuable than the data obtained several tens of bars removed from the ideal gas point. Using data points obtained far away from the ideal gas point can induce extra inaccuracies in the fitted curve, because the curvature of the isotherms can vary with increasing pressure. This requires the fitting of a more complex curve, which does not benefit the overall accuracy of determining the ideal gas conditions.

Even though the OVAR is capable of reaching higher temperatures. The temperature range is chosen not only because it extends on the research by Nannan, but also because a safe margin is held with respect to the decomposition of D4. There is no specific temperature at which decomposition starts for D4, however it is known that at a temperature of 670 K, the decomposition rate is 1.1% per 1000 hours [3, 15]. Even though the experiment lasts around 8 hours, these conditions should be avoided due to the significant influence of impurities on the accuracy of the results. In order to avoid the region where significant degradation occurs, the upper temperature bound is set at 600 K. Between the minimum and maximum temperatures, two extra isotherms are measured at 520 K and 560 K. This results in four isotherms roughly spaced by 40 K along the entire temperature range.

An overview of the proposed test cases is given in both Tabs. 3.1 and 3.2. Table 3.1 gives the frequency around which the experiments should be centred. The frequency values are obtained by applying

$$f_k = k\frac{c}{2l}, \tag{3.3}$$

to speed of sound data obtained from RefProp [41], which are given in Tab 3.2. In Eq. 3.3, f_k indicates that only the longitudinal mode is being tested, which for the OVAR is the most predominant resonance mode, c the speed of sound and l indicates the length of the OVAR.

Table 3.1: The frequencies [Hz] at which the measurements should be centred, data obtained through RefProp [41]

Temp. [K] / Pres. [Bar]	495	520	560	600
0.5	202.9	208.6	217.4	225.6
0.75	200.1	206.3	215.5	224.2
1	197.3	203.9	213.6	222.7
1.25	194.4	201.4	211.7	221.2
1.5	191.4	198.9	209.8	219.7

Table 3.2: Expected values for the speed of sound [m/s] obtained through RefProp

Temp. [K] / Pres. [Bar]	495	520	560	600
0.5	115.8404	119.2080	124.2947	129.3590
0.75	114.3220	117.9329	123.3112	128.5361
1	112.7488	116.6226	122.3100	127.7071
1.25	111.1160	115.2748	121.2902	126.8715
1.5	109.4177	113.8868	120.2512	126.0294

3.2.3. Experimental procedure

A day before the experiment is conducted, the fluid is injected into the syringe, that controls the amount of fluid within the cavity, is degassed three times. Degassing of a fluid aims to remove all the air that is inside of the fluid, which acts as a form of impurity if not removed properly. The fluid is then maintained at a vacuum overnight. This syringe is degassed for a fourth time before the start of the experiment, to further remove the amount of air in the fluid. Before the fluid is injected into the resonator, the resonator is heated to the temperature of the first isotherm to be measured, at 495 K. The first tests of the prepared batch of D4 showed a slight offset of 1% with the estimated values, without a known cause. This batch of D4 was replaced with a different batch and was inserted and degassed. It should be noted that with the new batch of D4 a discrepancy of 1.7% with the expected value was still observed, finding the cause of this discrepancy is outside of the scope of this study. Even though this discrepancy exists, the entire experiment was conducted with this new batch.

For each of the red points shown in Fig. 3.3, the measurements were conducted by performing a frequency sweep around the centre frequency. First the centre frequency is found and is based on the estimates given in Tab 3.1. From the centre frequency measurements are taken by increasing and decreasing the frequency at the emitting transducer by 0.5 Hz per step, covering a span of 10 Hz per measurement point. This allows for the observation of the entire resonance span for most of the measurements. For a limited number of measurements this span was extended to 15 Hz, because not the entire resonance was observed within the 10 Hz range.

In order to alter the pressure of the fluid within the cavity, the hand operated syringe is used. Altering the pressure is done by removing or adding extra fluid from the cavity of the OVAR, until the right pressure points have been met. After the experiment is done, the resonator and D4 inside is cooled, and the D4 is extracted from the resonator. The post processing of the measurements and the results of the experiment are discussed in Chap. 4.

3.2.4. Measured experimental data

The actual experimental measurements obtained follow from the experimental methodology and the proposed conditions specified earlier this chapter. Slight deviations occurred during the execution of the experiment, with respect to the proposed experimental data points. The actual measurements conducted in the experiment are shown in Fig. 3.2. It should be noted that during the experiment the isotherm at 603 K is measured instead of the proposed isotherm at 600 K. This figure shows the saturation dome for D4 in the $P-v$ plane, in conjunction with the isotherms that have been analysed by Nannan and those analysed in this thesis. This figure has been created using the thermodynamic model RefProp. From the figure it can be observed that the analysis is conducted, highlighted by the red box, on the vapour side of the saturation dome at subcritical pressures, p_c = 13.20 bar. Furthermore, the results of the experiment and the data obtained by Nannan are present in this figure.

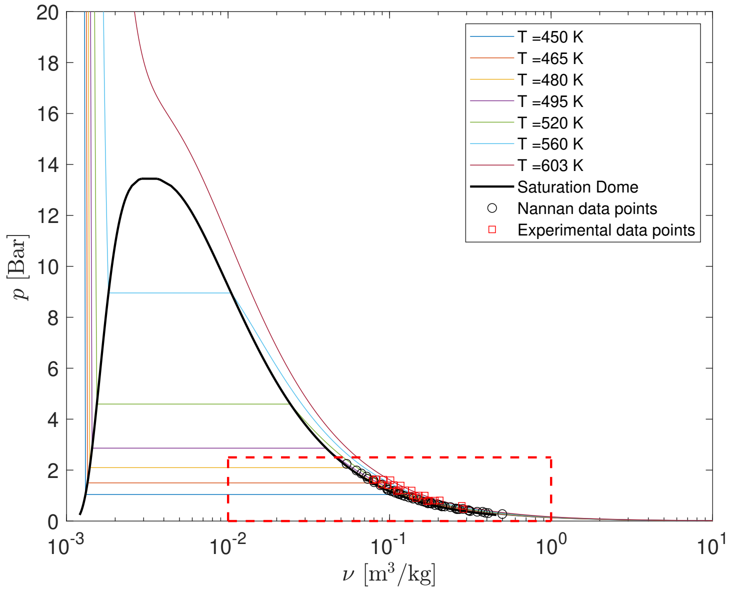

Figure 3.2: Saturation dome in the $p-v$ plane. The highlighted red box indicates the region where the acoustic experiments are performed.

In Fig. 3.3 the area indicated by the dashed red box is enlarged to gain a clearer picture of the location of the test cases. In the figure, the black circles indicate the experimental data points that were obtained by Nannan, while the red squares indicate the measurements of the carried out experiment. Differences with between the experimental cases and Nannan's cases are visible, the test results by Nannan do not show nearly isobaric measurements, since the results are scattered across the various isotherms. For the carried out experiment, this nearly isobaric alignment stems from the proposed test cases given in Tabs. 3.2 and 3.1. Furthermore, it can be observed in the figure that for the isotherm at 495 K, three measurement points overlap exactly with Nannan's data. Those are the points at 1.608, 1.438 and 0.4727 bar.

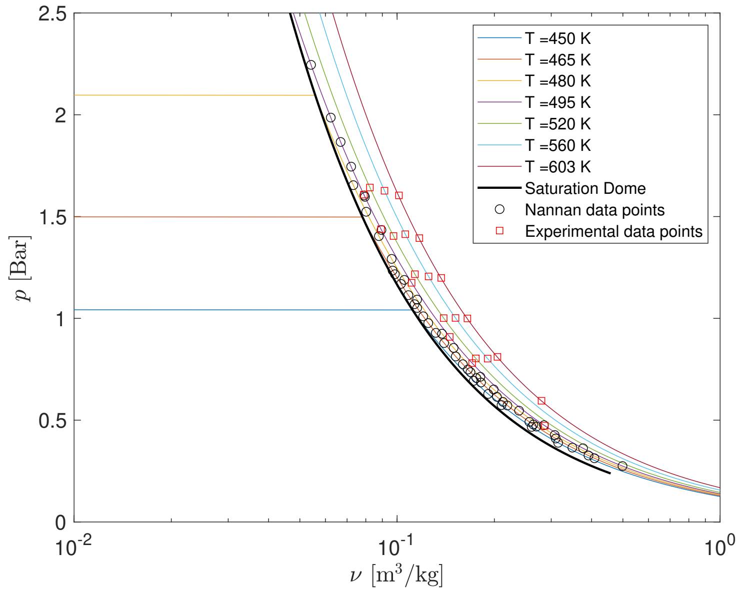

Figure 3.3: The highlighted red box area of Fig. 3.2, the proposed test cases and experimental cases by Nannan are clearly visible.

3.3. Summary

An overview of the methodology and design of the experiment was given in this chapter. The experiment conducted for thesis is designed for D4 for the temperature and pressure range of 495 K - 603 K and 0.4-1.6 bar respectively. The actual results differed slightly from these design values, due to considerations made regarding overlapping certain results with the results of Nannan. Furthermore, the resonator used for the experiment is described in detail. This is a box type resonator, for which the analysis is straight forward using Eq. 3.3, because of the geometry of the OVAR.

The experimental procedure requires degassing of the fluid multiple times before being injected by a hand operated syringe. This also controls the pressure of the fluid during the experiment, as fluid can be injected or extracted using this hand pump. The measurements are conducted by performing a frequency sweep with a span of 10 Hz around a centre frequency determined by the data given in Tab 3.1. The step size of the sweep is 0.5 Hz providing enough resolution to determine the resonance peak per point measured.

4

Results and analysis of the speed of sound experiment

This chapter features the analysis of the experimental data and a discussion of the results. The goal of this chapter is to clearly illustrate the steps taken to process the raw data and transform it into a form that can be used to answer the research question of the experimental study. Furthermore, a sensitivity analysis is conducted with regards to a change of the measured speed of sound data.

The chapter is organized as follows: In Sec. 4.1, the post processing of the experimental data is performed. This is followed by Sec. 4.2, where the initial analysis of the quadratic fitted speed of sound data is presented. An alternative fitting method is introduced in Sec. 4.3. In Sec. 4.4, the analysis of the ideal gas isobaric heat capacity is addressed, with comparisons made to thermodynamic models and literature data. A sensitivity analysis is performed on the method used to obtain the ideal gas isobaric heat capacity in Sec. 4.5. This chapter is concluded in Sec. 4.6.

4.1. Post-processing of raw data

In this section, the post-processing of the raw experimental data is addressed. The OVAR is an acoustic resonator available at the Propulsion & Power group at Delft University of Technology, used specifically for performing speed of sound measurements in the dense vapours of organic fluids. The thermodynamic properties measured using the OVAR are the static pressure and temperature of the fluid within the cavity and a static pressure measuring the resonance induced pressure increase.

The frequencies of the resonance peaks are obtained by applying a Fourier transform on the resonance induced static pressure measurement. From the acquired frequency data, the speed of sound is obtained. The resulting speed of sound data in combination with the measured temperature and pressure are then used to determine the ideal gas heat capacity. Before in-depth analysis on the speed of sound and ideal gas heat capacity data can be performed, the experimental data requires a degree post processing.

4.1.1. Preliminary data selection

The OVAR experiment was conducted over 57 separate runs at different temperatures and pressures. Based on observations during the experiment, several of these runs were neglected either due to incomplete measurements or because of the use of an incorrect centring frequency during the experiment.

4.1.2. Selection based on the quality of the resonance peak

Following this initial pre-selection of runs based on the experimental observations, the next step undertaken during the post processing phase is the selection based on the quality of the peaks. For the measured signal the quality of the resonance peak determines whether the intended resonance frequency is accurately measured or not, and can be affected by phenomena such as the overlapping of resonance modes. Poor quality in the resonance peak can be observed in the form of an increased width of measured frequencies, or by multiple measured peaks spaced apart. This is clearly seen in Fig. 4.1a and Fig. 4.1b, which show the measured resonance pressure as a function of the frequency. In Fig. 4.1a, a more pronounced resonance peak with smaller widths and larger heights can be observed, compared to the resonance peak of Fig. 4.1b. Based on this, it can be concluded that the resonance peak of Fig. 4.1a is better than that of Fig. 4.1b. In order to numerically quantify the quality of the peaks, a numerical expression is introduced for the Peak Quality, given by:

$$PQ = \frac{\mu(f_{\max})}{\sigma(f_{\max})}. \tag{4.1}$$

where $\mu(f_{\max})$ is the mean of the maximum of the measured frequency peaks and $\sigma(f_{\max})$ is the corresponding standard deviation. This is the inverse of the coefficient of variation often used in statistics to determine the precision or quality of a measurement [28]. In this case a higher value of PQ corresponds to a higher the quality of the resonance peak. Using Eq. 4.1 yields a PQ of 208.45 for the run shown in Fig. 4.1a , while for the run shown in Fig. 4.1b PQ is 49.67. Even though this is four times lower, the latter run is still considered for further analysis, since the limiting value for PQ has been set at 10. This can be justified as the resonance peak is still visible as a single peak in Fig. 4.1b. It should also be noted that the case shown in Fig. 4.1b resulted in the lowest value for PQ for all the experimental data points considered for the analysis. Since all other runs exceeded the lower indicated limit for PQ, no additional runs were excluded from further post processing.

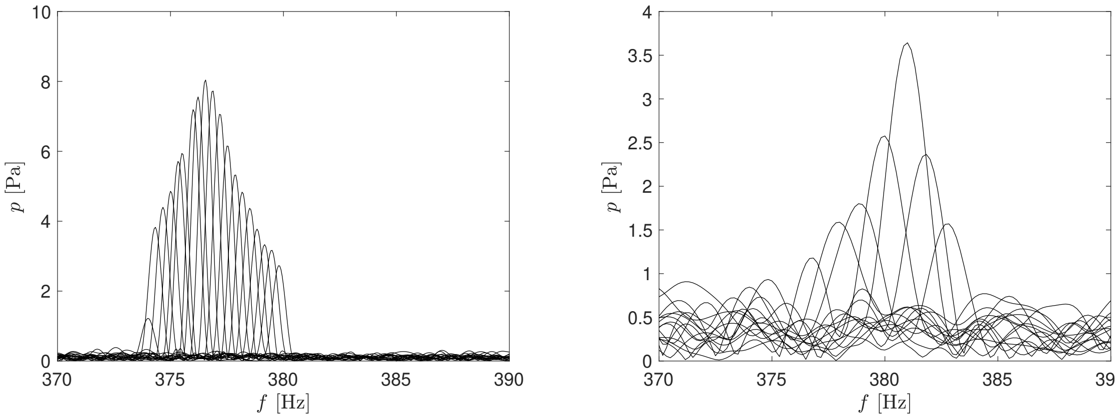

(a) Measurement of a resonance peak at T = 495K, p = 1.604 bar and PQ = 208.45

(b) Measurement of a resonance peak at T = 495K, p = 1.43 bar, PQ = 49.67

Figure 4.1: Resonance peaks for two sample measurements taken from the speed of sound measurement experiment for the substance D4

4.1.3. Acquiring the speed of sound from the frequency data

The frequency data is converted to speed of sound data using the following relationship for a cuboid shape,

$$f_{k,m,n} = \frac{c}{2}\sqrt{\left(\frac{k}{l_0}\right)^2 + \left(\frac{m}{h_0}\right)^2 + \left(\frac{n}{h_0}\right)^2}, \tag{4.2}$$

where k, m, n represent the longitudinal and two radial modes respectively. Recalling from Chap. 3, $l_0 \gg h_0$ for the OVAR, Eq. 4.2 reduces to

$$c = \frac{2 f_k l_0}{k}. \tag{4.3}$$

This equation therefore relates only the longitudinal resonance modes to the speed of sound of the substance at the prescribed temperature and pressure conditions.

4.1.4. Detecting outlier data

The next step in the process procedure involves the identification of outlier data points within the data set. The raw data set is shown in Fig. 4.2, which displays the spread of the data points at each of the measurement conditions. In order to accurately determine the ideal gas speed of sound outliers are numerically identified and removed from the data set. For the data set at hand, it is required to determine the outliers for measurements of the same temperature and pressure combination. However, for several of these measurement points only one or two data points are available. This is problematic as a minimum of three data points are required to determine an outlier in the data set. In order to provide the minimal amount of data points to determine the outliers for all measurement points, the thermodynamic models RefProp and StanMix are consulted. Data from both models at the same temperature and pressure conditions as the experimental results were included in the outlier detection procedure, in order to meet the minimal limit of data points required. These additional data points from the thermodynamic models were only included for this step of the post processing.

The outliers in the data were detected using a built in Matlab function. This function deems a value an outlier if the value is more than three times the scaled value of the Median Absolute Deviation (MAD) away from the median value of the data set. The MAD is defined as

$$MAD = \text{median}(A_i - \text{median}(A)), \tag{4.4}$$

where median(A) is the median of the dataset. The scaling factor is given as

$$sf = \frac{1}{\sqrt{2} \cdot \text{erfcinv}\left(\frac{3}{2}\right)}, \tag{4.5}$$

where *erfcinv* is the Inverse Complementary Error Function. The bounds to determine whether a data point is an outlier or not is given by

$$\begin{gathered} A_i < \text{median}(A) - 3 \cdot sf \cdot MAD \\ , A_i > \text{median}(A) + 3 \cdot sf \cdot MAD. \end{gathered} \tag{4.6}$$

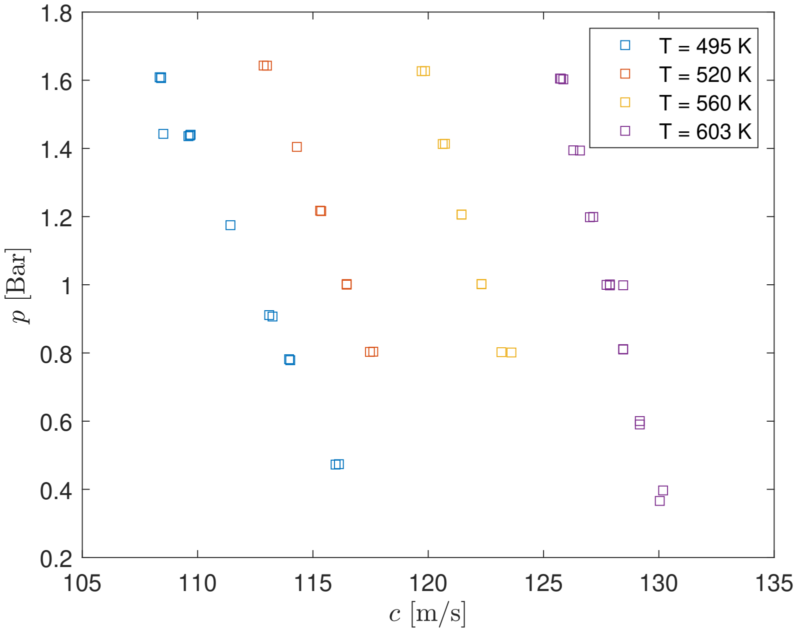

Figure 4.2: Speed of sound vs pressure for all individual experimental data points before the removal of outliers

4.1.5. The uncertainty of the raw data

In order to obtain a clearer overview of the experimental data points, the average of the data points for each of the measurement conditions is shown in Fig. 4.2. Furthermore, the experimental uncertainty, which was neglected thus far, is also included. The known uncertainty of OVAR was used as a basis for uncertainty, since not enough data points were measured to determine the random error at each of the measurement conditions. The measurement uncertainty of the OVAR is $\approx 0.3\%$, which is applied to the speed of sound data [34].

Prior to detection of outliers, the systematic error was removed by application of the calibration constant, $cc = 1.0139$. The calibration constant is determined from the average error obtained from the overlapping measurements with Nannan's data points at T = 495 K.

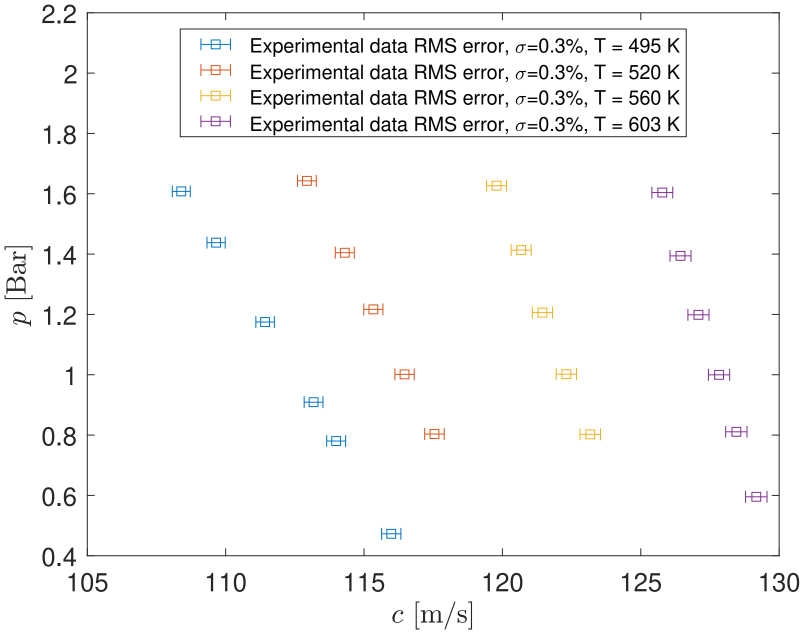

Figure 4.3: The refined data set after completing the post processing phase, with a standard error of $\sigma = 0.3\%$

4.2. Analysis of linear and quadratic fit of the experimental data

In the previous section, the post processing of the data set was discussed. This resulted in a refined data set, shown in Fig. 4.3, to be used for the ideal gas analysis. This section features the initial analysis of the linear and quadratic fit of the experimental data set. The analysis is followed by a discussion on the observed errors found for the fitted curves.

4.2.1. Methodology of fitting

Speed of sound measurements are a valuable source of thermodynamic data for a substance. The isobaric and isochoric heat capacities, as well as the compressibility factor are obtained using speed of sound data [5, 17, 54]. Furthermore, the ideal gas analysis for speed of sound data is not only limited to the ideal gas heat capacity, but are also used to determine the universal gas constant [36], and has been used to define temperature scales [5]. However, for this research the experimental analysis is limited to the ideal gas heat capacity. This is done, so that the research question regarding the validity of the thermodynamic models can be answered.

In order to answer this research question, the ideal gas isobaric heat capacity, c_p^{IG}, is required. This requires an approximation of the ideal gas conditions, where $p \rightarrow 0$, as it is physically impossible to measure at these conditions. The most commonly used method found in literature requires the extrapolation of experimentally determined speed of sound data to $p \rightarrow 0$, such that the ideal gas speed of sound is obtained. From the ideal gas speed of sound, the ideal gas isobaric heat capacity is calculated, using Eq. 2.4.

The ideal gas speed of sound is obtained from the experimental data through a second order curve fitting, as was done by Nannan. This is done in order to provide the best comparison with the data in literature. Thus, a quadratic relation between the pressure and the experimentally determined speed of sound is established. This relation is used to extrapolate to the ideal gas point.

The fitted results of the conducted experiment are shown in Fig. 4.4. For every isotherm, a linear and quadratic fit are performed. For the isotherm at T = 495 K, shown in Fig. 4.4a, the experimentally determined data by Nannan are also included (in green). The error bounds were established at every experimental point, as described in Sec. 4.1. The error bound at the ideal gas condition is obtained as an output of the fitting function used to obtain the curves. The bounds are only present for the quadratic curves, because the results of the linear fits are only used to contrast with the quadratic lines. This simplifies the identification of errors in the curvature of the quadratic lines. Furthermore, at the temperature and pressure conditions of the conducted experiment, real gas effects affect the measured speed of sound. This results in a concave curvature for the relation between pressure and speed of sound. This is in contrast with the ideal gas assumption, for which the pressure and speed of sound follow a linear relation. Because of the real gas effects, the measured speed of sound data should result in a slight concave curvature as demonstrated by the line obtained from Nannan, shown in green in Fig. 4.4a. The real gas effects have a larger influence at lower temperatures compared to higher temperatures, because the saturation pressure is lower at lower temperatures. This results in an increased curvature for the lower temperature isotherms.

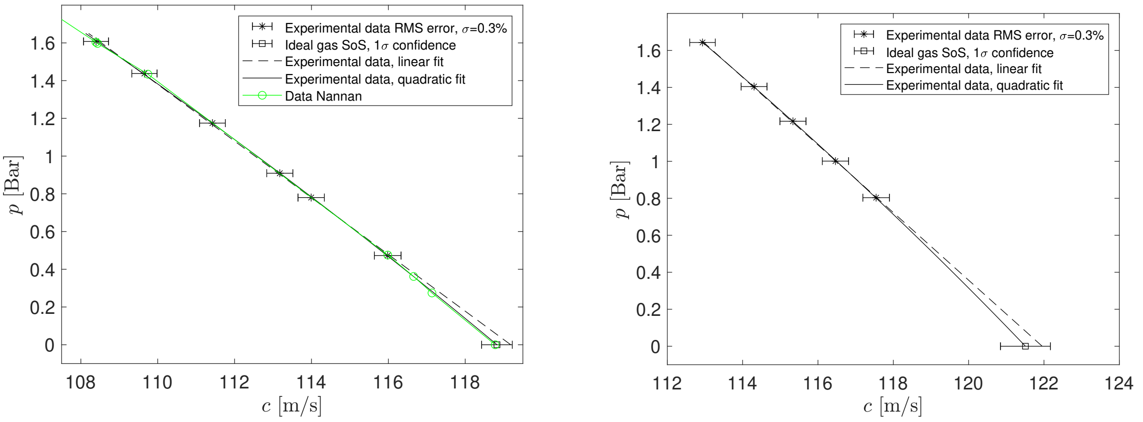

(a) T = 495 K, green line refers to Nannan's data at T = 495K [40]

(b) T = 520 K

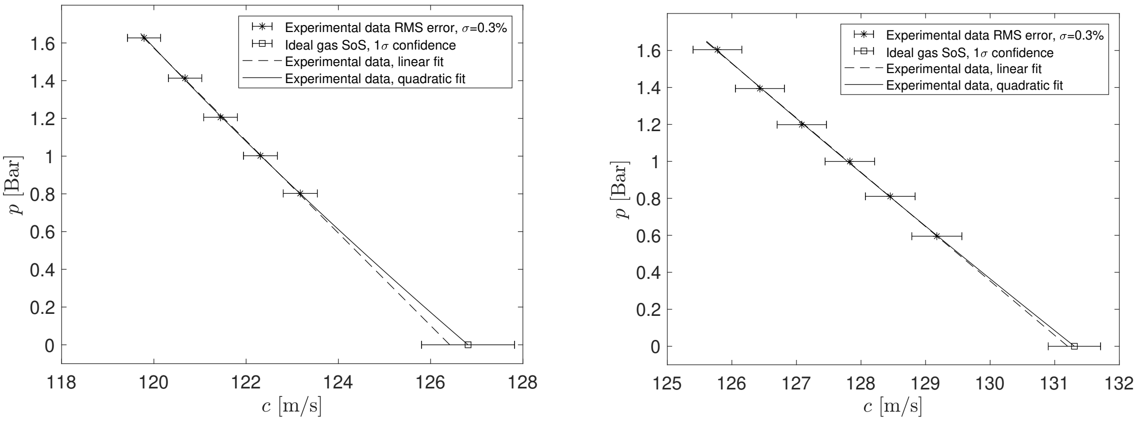

(c) T = 560 K

(d) T = 603 K

Figure 4.4: Linear and quadratic fit of the speed of sound data at the four measured isotherms

4.2.2. Discussion on observed errors in curvature

In the previous subsection, the expected curvature of the isotherms is discussed. It is expected that the curvature of these isotherms is concave, as was shown by the example taken from Nannan's data [40]. For Figs. 4.4a and 4.4b, this concave curvature is shown by the leftward diverging quadratic line away from the linear solution at lower pressures. Furthermore, Tab. 4.1 provides values for the second partial derivative of the speed of sound with pressure along each isotherm, based on a quadratic fit of data by Nannan. The second partial derivative of these fitted curves indicates the curvature of the isotherms, thus providing numerical information on the validity of the isotherms. For all four measured isotherms by Nannan the second derivative is negative, indicative of the concave curvature of the relation between speed of sound and pressure. Another previously mentioned criterion concerns the decrease of the curvature coefficient with increasing temperature. For the data by Nannan this criterion is also met, as the absolute value of the curvature coefficients decreases with increasing temperature.

Table 4.1: The second derivative based on a quadratic fit using the experimental data obtained by Nannan [40]

Temperature $[K]$	$\left(\frac{\partial^2 c}{\partial p^2}\right)_T \left[\frac{m}{sPa^2}\right]$
450	-1.946
465	-1.916
480	-1.669
495	-1.301

Contrary to Figs. 4.4a and 4.4b, where a clear concave curvature can be observed for the quadratic fits, Figs. 4.4c and 4.4d show a deviation from the expected curvature. In these two figures and most notably for Fig. 4.4c, it is observed that the quadratic fitted curve diverges to the right of the linear solution. Therefore, it can be concluded that the curvature of these two lines is of convex nature. This point is further supported by Tab. 4.2, where the second partial derivative of the speed of sound with pressure is given for the quadratic fitted lines of the experimental results. For the cases T = 560 K and T = 603 K the second partial derivative is positive, diverging from Nannan's results and thus confirming the convex curvature of these two quadratic fitted curves observed in Figs. 4.4c and 4.4d. Moreover, an increase in the absolute value of the second derivative with increasing temperature is observed between the two concave cases, T = 495 K and T = 520 K. This is in contrast with the earlier explanation regarding the reduction at higher temperatures due to a reduced influence of real gas effects.

Table 4.2: The second derivative based on a quadratic fit using the data from the conducted speed of sound measurement experiment

Temperature $[K]$	$\left(\frac{\partial^2 c}{\partial p^2}\right)_T \left[\frac{m}{sPa^2}\right]$
495	-0.465
520	-0.632
560	0.571
603	0.190

The observed errors in curvature and the unexpected increase of the curvature with increasing temperature leads to the following conclusion: by quadratic fitting of the experimentally determined speed of sound data, no consistent and physically coherent result can be obtained. Therefore, the explained fitting method does not provide enough confidence to proceed with the analysis of the experimental data following this approach. In order to confidently analyse the ideal gas data, a different approach is therefore required to obtain the ideal gas speed of sound via extrapolation of the experimental data.

4.3. Alternate approach for fitting of experimental data

In order to acquire a more physically accurate and consistent solution for the fitting, an alternative fitting function is developed to fit the experimental data. In Sec. 4.2, the main problem with the fitting was caused by the curvature coefficient of the quadratic relation. The methodology of the alternative fitting method is addressed in this section, followed by a discussion of the results obtained using this alternative fitting method.

4.3.1. Methodology for the alternative fit

The alternative fitting function is still a quadratic polynomial, but with a fixed curvature coefficient. The curvature coefficient is obtained from the thermodynamic model RefProp, by applying a quadratic fit to data obtained from the model for the same temperature and pressure range as in the experiment. A second order polynomial is expressed as

$$y = ax^2 + bx + c,$$

where a represents the curvature coefficient. In a normal fitting procedure, all three coefficients are determined, but for the alternative fitting procedure the term a is determined from the model data. The remaining terms, b and c, are then obtained by fitting the experimental data. Similar to Sec. 4.2, this provides a quadratic function used to obtain the ideal gas speed of sound for each of the experimentally studied isotherms. These ideal gas speed of sound values are then used Sec. 4.4 to determine the ideal gas isobaric heat capacity.

4.3.2. Analysis of the alternative fitted results

Similar to Fig. 4.4 shown in Sec. 4.2, Fig. 4.5 shows the experimental data in combination with the quadratic lines determined using the alternative fitting method. The linear fitted line of the experimental data is included as a form of contrast with the quadratic solution, used to identify the correctness of the curvature. The error bounds for the experimental data points shown in Fig. 4.5, are obtained using the known standard deviation of the OVAR, as previously discussed in Sec. 4.1. The error bounds for the ideal gas conditions are determined as a combination of several deviations that can influence on the extrapolation of the ideal gas point. These deviations are:

- The average deviation between the experimental results and the fitted curve, called the fitting error e_{fit}
- The upper bound deviation provided by the fitting function, $e_{\text{up,bnd}}$
- The lower bound deviation provided by the fitting function, $e_{\text{low,bnd}}$
- The average of the known standard deviation per data point of the experimental results, $e_{\text{std,ave}}$

The total error for the ideal gas point was determined by:

$$e_{\text{tot}} = \sqrt{e_{\text{fit}}^2 + e_{\text{up,bnd}}^2 + e_{\text{low,bnd}}^2 + e_{\text{std,ave}}^2}. \tag{4.7}$$

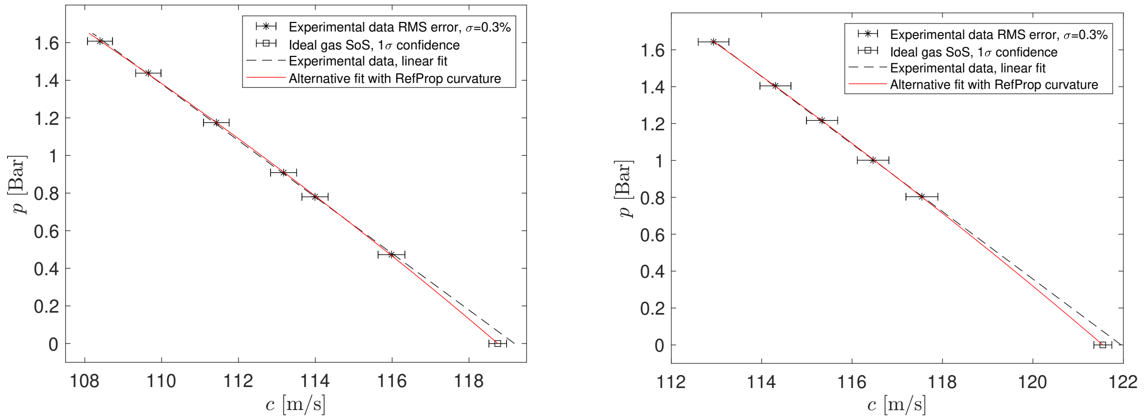

(a) $T = 495$ K **(b)** $T = 520$ K

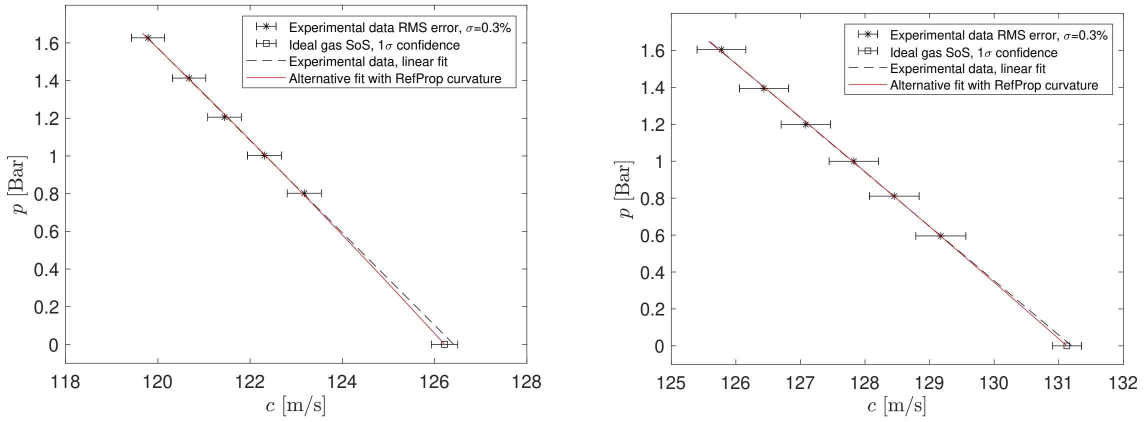

(c) $T = 560$ K **(d)** $T = 603$ K

Figure 4.5: Alternative fitted curves based on the speed of sound data at the four measured isotherms

For the curvature coefficients obtained via RefProp, it can be assumed that these adhere to the two criteria established earlier. Again, these two criteria are as follows: the relation between the speed of sound and pressure should have a concave curvature and the curvature should decrease with increasing temperature. Numerically, this concave curvature is represented by a negative partial second derivative of the speed of sound with pressure. Furthermore, the absolute values of this partial second derivative should decrease with increasing temperature. In Fig. 4.5, it can be observed that both of these requirements are satisfied. The concave requirement is met by the observed leftward divergence of the red line from the linear dashed line in all four figures. The requirement regarding the decrease in curvature with increasing temperature is also observed in Fig. 4.5, by comparing the reduction in magnitude of the divergence of the red line at the different temperatures analysed.

Numerically, this is also supported by Tab. 4.3, where the second partial derivative of the speed of sound with respect to pressure is tabulated. This table shows that the criterion for concave curvature is met, because all values are negative. The second criterion is also met, because the decrease of the absolute value of the curvature coefficient with increasing temperatures is shown in Tab. 4.3.

Table 4.3: The second derivative based on a quadratic fit using the data from the conducted speed of sound measurement experiment

Temperature $[K]$	RefProp $\left(\frac{\partial^2 c}{\partial p^2}\right)_T \left[\frac{m}{sPa^2}\right]$
495	-1.0639
520	-0.6684
560	-0.3349
603	-0.1639

The results of the alternative fitting method satisfy both criteria for the expected results of the analysis, providing an improved solution over the results obtained in sec. 4.2. This results in greater confidence in the accuracy of the results produced by the alternative method over the conventional method. However, it would have been more beneficial if the experimental data could have been correctly analysed using the conventional method.

4.4. Ideal gas heat capacity analysis

The final phase in the analysis of the experimental data focuses on the analysis of the ideal gas heat capacity. The ideal gas heat capacity is obtained from the ideal gas speed of sound, determined through fitting of experimentally determined speed of sound data. This section details the methodology used to obtain the ideal gas heat capacity from the ideal gas speed of sound, followed by the analysis of both extrapolated literature data and the model data.

4.4.1. Obtaining the ideal gas heat capacity

The ideal gas isobaric heat capacity is determined from the obtained ideal gas speed of sound using the method described in the previous section. The ideal gas heat capacity is computed using the following equation:

$$C_{p,m}^{IG} = \frac{(c^{IG})^2 M}{T\left[\frac{(c^{IG})^2 M}{RT} - 1\right]}. \tag{4.8}$$

This relation was also implemented by Nannan [40] to determine the ideal gas heat capacity for D4, and is also found in other studies for determining $c_{p,m}^{IG}$ for other substances [17, 54]. Through this process of fitting, the acoustic virial equation is obtained. The acoustic virial equation of state is given by:

$$c = c^{IG}\left[1 + \left(\frac{\beta_a(T)}{RT}\right)p + \left(\frac{\gamma_a(T)}{RT}\right)p^2 + \left(\frac{\delta_a(T)}{RT}\right)p^3 + \dots\right], \tag{4.9}$$

where β_a, γ_a and δ_a are the second, third and fourth acoustic virial coefficients respectively. The polynomial series can be expanded to higher orders to obtain more acoustic virial coefficients, but this is beyond the scope of the conducted research. Thus, the focus remains on the analysis of a second order polynomial. Through the quadratic fitting of the experimental data, the second and third acoustic virial coefficients can be determined. Eq. 4.8 is derived from an alternative but similar method implemented by Trusler [54]. The entire derivation of Eq. 4.8 is given in Appendix C. Trusler relates the speed of sound to pressure with the following relation:

$$\left(\frac{c}{a_0}\right)^2 = \frac{A_0 + A_1 p + A_2 p^2 + \dots}{a_0^2}, \tag{4.10}$$

where A_n are the coefficients to be fitted and a_0 is the mean linear expansivity coefficient. In the ideal gas limit of $p \to 0$, this results in

$$\left(c^{IG}\right)^2 = A_0, \tag{4.11}$$

where A_0 is given by:

$$A_0 = \frac{RT\gamma^{IG}}{M}, \tag{4.12}$$

and γ^{IG} is defined as

$$\gamma^{IG} = \frac{c_p^{IG}}{c_v^{IG}}. \tag{4.13}$$

Furthermore, it is known that

$$c_v^{IG} = c_p^{IG} - R. \tag{4.14}$$

Combining the right-hand sides of Eqs. 4.12, 4.13 and 4.14, and reordering the terms results in

$$\left(c^{IG}\right)^2 = \frac{RT}{M}\frac{c_p^{IG}}{c_p^{IG} - R}. \tag{4.15}$$

This equation needs to be rewritten, using the following steps in order to obtain Eq. 4.8

Finally, this results in the corresponding relation given by Eq. 4.8

$$c_p^{IG} = \frac{\left(c^{IG}\right)^2 M}{T\left[\frac{(c^{IG})^2 M}{RT} - 1\right]}. \tag{4.16}$$

Therefore, demonstrating that the ideal gas isobaric heat capacity can be obtained from a polynomial fit of the speed of sound data.

The ideal gas speeds of sound for the four experimentally measured isotherms are tabulated in Tab. 4.4. The lower and upper bounds of the absolute speed of sound values corresponding to the error bounds in Fig. 4.5 are also included.

Table 4.4: The experimentally determined ideal gas speed of sound using the alternative fitting method with the curvature coefficient based on data from RefProp

Temperature [K]	c^{IG} = [m/s]	lower bound [m/s]	upper bound [m/s]
495	118.7487	118.5174	118.9800
520	121.5468	121.3479	121.7457
560	126.2147	125.9279	126.5014
603	131.1257	130.9001	131.3514

The values for the ideal gas isobaric heat capacity are tabulated in Tab. 4.5. These values are determined from the ideal gas speed of sound data using Tab. 4.4 and Eq. 4.8. It should be noted that the upper bound values in Tab. 4.5 are determined from the lower bound values for the speed of sound in Tab. 4.4 and vice versa.

Table 4.5: The experimentally determined ideal gas isobaric heat capacity using the alternative fitting method with the curvature coefficient based on data from RefProp

Temperature [K]	c_p^{IG} = [J/molK]	upper bound [J/molK]	lower bound [J/molK]
495	519.5177	683.7919	419.3581
520	622.7240	821.9972	501.6957
560	569.6510	822.9550	436.2776
603	491.3030	614.4603	409.6241

Besides the values obtained using the alternative fitting method, the conventional quadratic fitted results are also included in the figures presented in the analysis. This is done to further indicate the improvements made using the alternative method. The values of both the ideal gas speed of sound and ideal gas isobaric heat capacity are tabulated in Tabs. 4.6 and 4.7 respectively.

Table 4.6: The experimentally determined ideal gas speed of sound using the conventional fitting method.

Temperature [K]	c^{IG} = [m/s]	lower bound [m/s]	upper bound [m/s]
495	119.0259	118.6593	119.3925
520	121.5074	120.8452	122.1695
560	126.8122	125.8039	127.8205
603	131.3048	130.8994	131.7102

Table 4.7: The experimentally determined ideal gas isobaric heat capacity using the conventional fitting method.

Temperature [K]	c_p^{IG} [J/molK]	upper bound [J/molK]	lower bound [J/molK]
495	403.9838	572.6305	312.7285
520	654.0865	4464.2226	355.5508
560	348.4588	1020.0821	212.1022
603	424.1381	614.9323	324.4114

4.4.2. Comparison of experimental results with literature data

The research performed by Nannan[40] on D4 provides a direct point of comparison for both the ideal gas speed of sound as well as the ideal gas isobaric heat capacity. The former was already discussed in Sec. 4.2, while the latter is presented in this subsection. It should be noted that the values from the article of Nannan were obtained at lower temperatures than the experiment conducted in this thesis. Therefore, the data by Nannan is extrapolated to the experimental conditions in order to gain an insight on the accuracy of the experimental data. The ideal gas speed of sound and ideal gas isobaric heat capacity obtained by Nannan are shown in Tab. 4.8. The actual speed of sound and pressure values measured by Nannan [40] used to obtain the results in Tab. 4.8, are given in Appendix A.

Table 4.8: The experimentally determined ideal gas speed of sound and ideal gas isobaric heat capacity obtained by Nannan [40]

Temperature [K]	c^{IG} [m/s]	c_p^{IG} [J/molK]
450	113.320	469.466
465	115.169	480.646
480	116.988	491.826
495	118.780	503.005

The previously presented ideal gas heat capacity data is plotted in a c_p^{IG} vs T graph in Fig. 4.6. The blue dotted line indicates the c_p^{IG} values in the study by Nannan. The orange line originating from the data from Nannan is the result of the linear extrapolation. This linear extrapolation was performed on the data obtained from Nannan, because in the article the assumption was made that the ideal gas isobaric heat capacity varied linearly with the temperature. According to Nannan, this assumption is valid due to the small temperature range covered in the experiment [40]. This small temperature range assumption might no longer be valid when extrapolating the data to the elevated temperatures at which the experiment is conducted. However, the data by Nannan already follows a linear trend, thus higher order extrapolation methods do not add a significant difference to the extrapolation. Therefore, the linear extrapolation is shown in Fig. 4.6.

The results of the quadratic and the alternative fitting procedures are plotted in black and red, respectively. The results are superimposed on each other to show the improvement made using the alternative fit over the conventional quadratic fit. Particularly, for the cases at 520 K and 560 K, this improvement can be observed as a significant reduction of the error bounds. This is because the upper error bounds determined by the conventional fitting method are significantly larger than those determined by the alternative method. The values for the error bounds are shown in Tabs. 4.5 and 4.7, for the alternative and conventional case respectively. Comparing these tables, it can be seen that the error bounds reduce in size through usage of the alternative fitting method. A striking example is found at T = 520 K, for the conventional method this results in an upper bound of c_p^{IG} = 4464.2226 J/molK, while for the alternative case the upper bound is c_p^{IG} = 821.9972 J/molK.

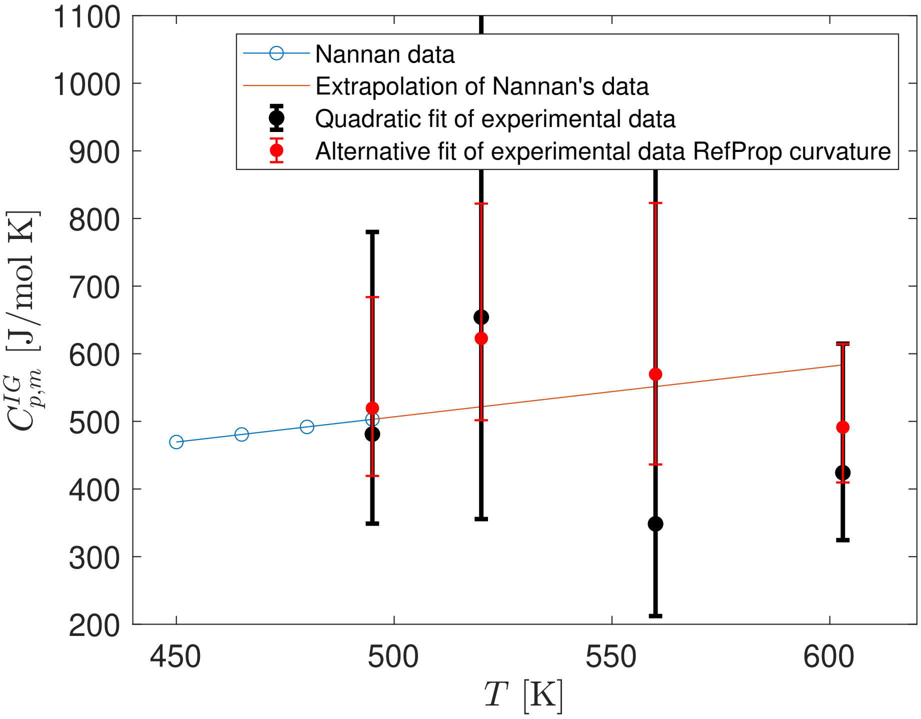

Figure 4.6: Comparison of the ideal gas isobaric heat capacity varied with temperature. A comparison between the experimentally obtained data and the data experimentally determined by Nannan[40] is shown. The error bounds indicate one standard deviation interval bound.

Besides comparing the different methods for obtaining the ideal gas heat capacity with each other, it is of interest to make a comparison between the different data sets. This is required because it will assure the validity of the experimental data before being compared to the model data. In Fig. 4.6, it is observed that the experimentally determined points follow the same trend as outlined by the linear extrapolation of the data from Nannan. This is especially true for the points measured at T = 495 K, T = 520 K and T = 560 K. This shows there are no large and unexpected deviations are present in the experimental results, supporting the model's validity. This inspires confidence for the further analysis, because Nannan's data is used in the determination of the thermodynamic models for D4. In Sec. 4.4.3 the analysis continues with a comparison between the experimental data and the thermodynamic model data.

4.4.3. Comparison of experimental results with model data

The comparison between the experimental and model data is given in Fig. 4.7. The model data is obtained from the thermodynamic models RefProp and StanMix. The ideal gas isobaric heat capacity values for these models are obtained using the same method as used for the experimentally determined ideal gas heat capacity, since the models have no output for c_p^{IG}.

From Fig. 4.7, it is observed that both the thermodynamic models and the experimental results don't show significant deviations at elevated temperatures. This is especially true for the measurements at T = 495 K, T = 520 K and T = 560 K. Though the measurement at T = 603 K does deviate slightly from the trend set by the other three experimental data points, both models intersect at the one sigma uncertainty bound of this measurement point.

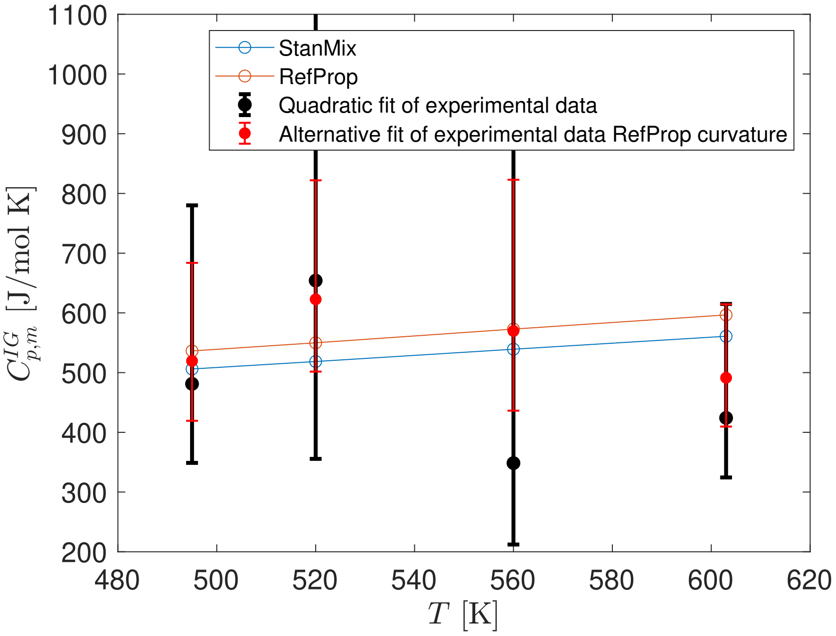

Figure 4.7: Comparison of the experimental results with the thermodynamic models RefProp and StanMix

In Fig. 4.8, it is clearly observed that there is no deviation in the trend between the experimental data and model data. In this figure, a linear trend is shown for the experimental data based on the first three experimental points at T = 495 K, T = 520 K and T = 560 K. The figure shows a nearly identical slope to the comparative model data. In Tab. 4.9 the values for the slope of each of the lines are given, showing that the difference in slope between RefProp and StanMix is only 2.8%. The point T = 603 K was left out, because the point made regards the slope of the subcritical data points. This point is the only supercritical isotherm measured. Furthermore, it is the only experimentally determined point to deviate from the trend of the subcritical points. However, the model data is still within the error bounds displayed for this point, hence the difference could be attributed to the uncertainty of the data point. For future research, it would be interesting to perform the same experiment exclusively for supercritical temperatures to determine whether the deviation of T = 603 K could be attributed to measurement error or not.

The research question to be answered in this chapter regards the validity of the thermodynamic models at elevated temperatures. The results presented in this section show that the models are able to qualitatively predict the thermodynamic properties of D4 at these elevated temperatures. However, the experimental results cannot be used to draw conclusions about the accuracy of the results predicted with the thermodynamic models, since the accuracy of the experimental results is not high enough for this. The data obtained from the experiment can therefore not be used to improve the thermodynamic models.

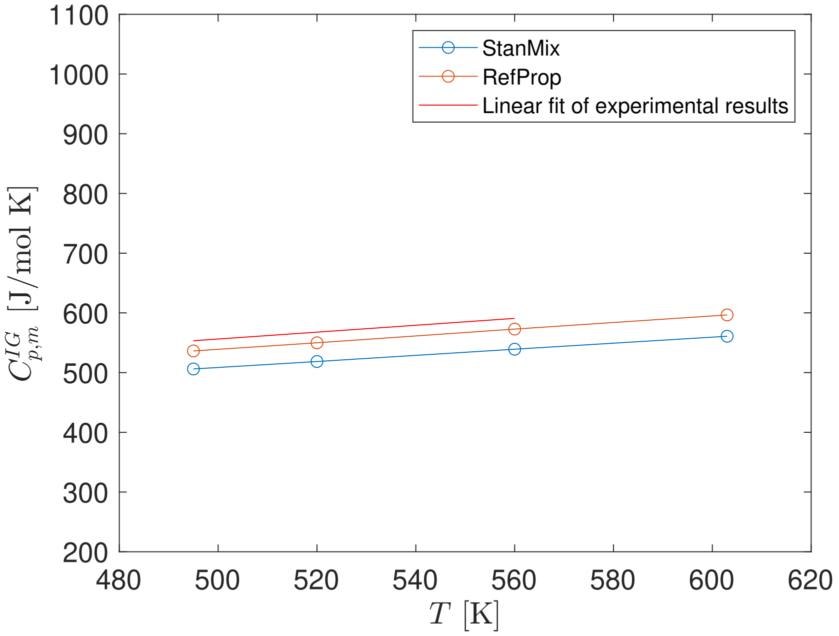

Figure 4.8: Comparison between the linear trend obtained from the experimental values measured at T = 495 K, T = 520 K and T = 560 K and the results obtained through the two thermodynamic models, RefProp and StanMix.

Table 4.9: The slope of the lines shown in Fig. 4.8

Case	$\left(\frac{\partial c_p^{IG}}{\partial T}\right)_p$ [J/molK^2]
StanMix	0.5082
RefProp	0.5602
Experimental data	0.5761

4.5. Sensitivity analysis of the method

The uncertainty bounds for the experimentally determined ideal gas isobaric heat capacity shown in Figs. 4.6 and 4.7, and in Tabs. 4.5 and 4.7 are significant, especially considering the size for the error bounds specified for the speed of sound in Tabs. 4.4 and 4.6. From this data it can be observed that the method utilized to determine the ideal gas isobaric heat capacity is quite sensitive to fluctuations in ideal gas speed of sound. This section provides a sensitivity analysis to investigate the extent to which this phenomenon could affect the method and its results.

4.5.1. Asymptotic behaviour of the method

The values shown in Tabs. 4.4 - 4.7 indicate that a minor change in ideal gas speed of sound results in a significant change in ideal gas isobaric heat capacity. This shows that the sensitivity in the method originates from Eq. 4.8. In Tab. 4.10 an example calculation is shown, indicating the sensitivity to a change in speed of sound. In the example the temperature is taken to be 495 K, while all other parameters besides the speed of sound are kept constant. For the first case, c is determined to be 119 m/s and this results in $c_p^{IG} = 412.52 \ \frac{\text{J}}{\text{molK}}$. In the second case, c is lowered by 0.5 m/s, so $c = 118.5$ m/s, resulting in $c_p^{IG} = 700.51 \ \frac{\text{J}}{\text{molK}}$. The difference in speed of sound between case 1 and case 2 is -0.42%, but the change in the ideal gas isobaric heat capacity between the two cases is 69.81%. For the example, the magnitude of the error is increased by 166 times the original error, due to Eq. 4.8.

Table 4.10: Example calculation showing the degree of sensitivity of Eq. 4.8 for T = 495 K

	Case 1	Case 2	Δ[%]
c^{IG} [m/s]	119	118.50	-0.42
c_p^{IG} $\left[\frac{\mathrm{J}}{\mathrm{molK}}\right]$	412.52	700.51	69.81

Further investigations were conducted by varying the speed of sound along a set range, for the four temperatures analysed during the speed of sound measurement experiment. The results of this analysis are shown in Fig. 4.9. Because an asymptote is observed for each of the isotherms investigated, the origin of the sensitivity is identified. This asymptotic behaviour explains the significant size of the uncertainty bounds. Furthermore, it also explains why the downward extending bounds in Figs. 4.6 and 4.7 differ in magnitude. It should be noted that these bounds for c_p^{IG} are obtained using the bound data for c^{IG}, given in Tabs. 4.4 and Tab. 4.6, in Eq. 4.8. The difference from the centre value for the upper and lower bound, expressed in c^{IG}, is equal in magnitude. However, due to the steepening of the asymptote shown in Fig. 4.9, these bounds differ in magnitude when expressed for c_p^{IG}.

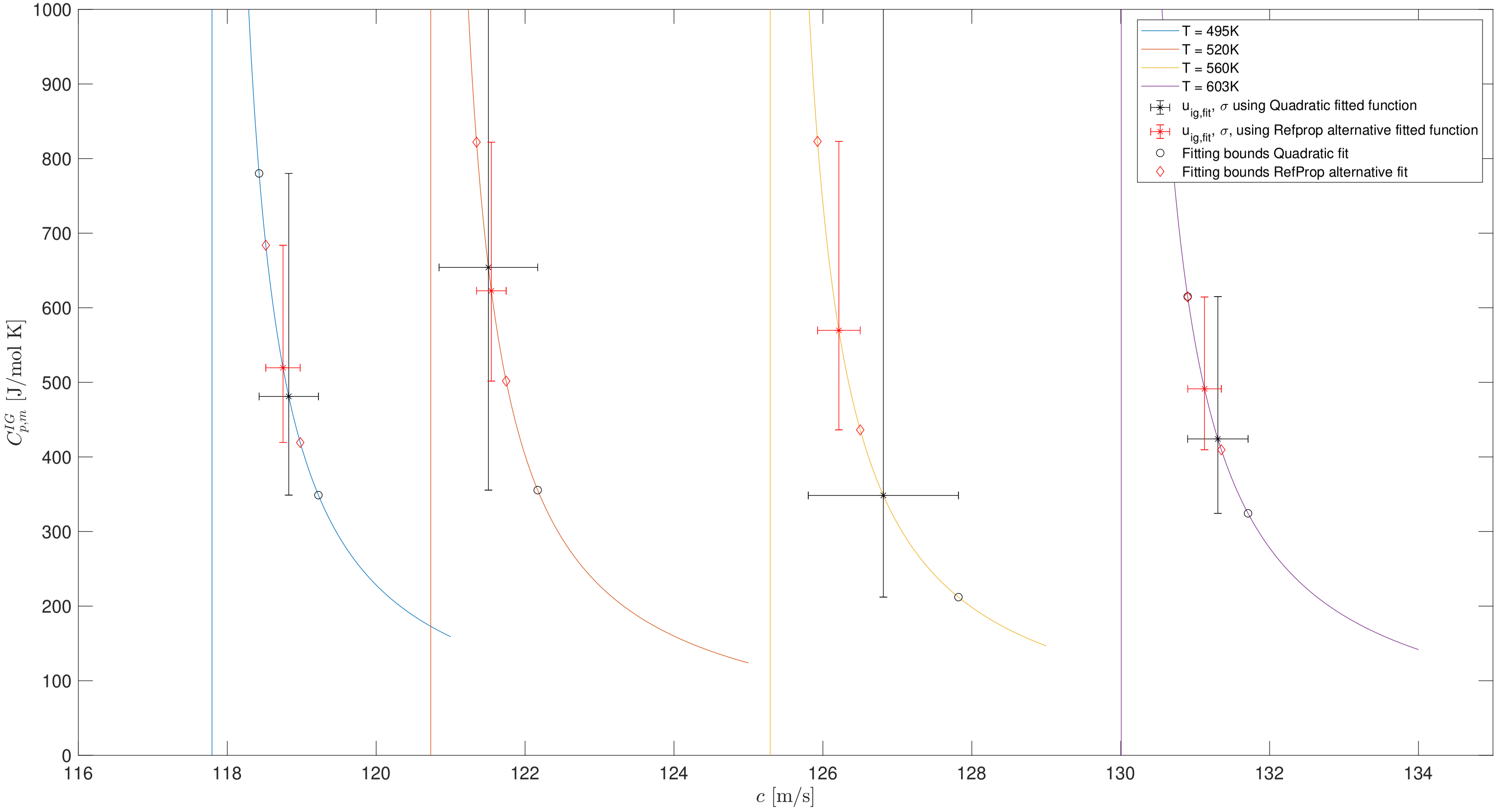

Figure 4.9: c_p^{IG} vs c^{IG} for the temperatures T = 495 K, T = 520 K, T = 560 K and T = 603 K. The sensitivity is caused by the displayed asymptotes for each of the isotherms, resulting in a variation of the uncertainty bounds.

4.5.2. Differences found between the experiment and literature

In the introduction of Sec. 4.4, it was mentioned that the method used was the most commonly used method to accurately obtain the ideal gas isobaric heat capacity from experimental data [17, 40, 54]. The results presented in these articles are of higher accuracy, which is mainly attributed to the measurement equipment used. It is known that a spherical resonator, used by Trusler [54] for the speed of sound analysis in methane, is more accurate than the box type resonator used to perform the measurements of this thesis. A similar statement is made for the accuracy of the resonator used by Nannan for the research on D4. However, the disadvantage of the resonator used by Nannan is the operating temperature which was limited compared to the temperature limit of the OVAR, as explained by Mercier [34]. The results of this thesis show that the OVAR provides results which are accurate enough to provide a qualitative assessment of the ideal gas isobaric heat capacity data at these elevated temperatures.

Because the conventional method is highly sensitive towards a change in the measured speed of sound, it is recommended to investigate an alternative analysis method for obtaining the ideal gas isobaric heat capacity from the speed of sound. This is the topic of discussion in Chaps. 5 and 6.

4.6. Summary

The focus of this chapter was to answer the answer the question whether the models are still valid when used at higher temperatures than the data used to formulate those models. From the analysis presented in this chapter it can be concluded that the three research goals have been met. The data and analysis presented in Sec. 4.1 and Sec. 4.2, show that the speed of sound of D4 is measured at higher temperatures than available in literature as well as for a supercritical isotherm, T = 603K. Furthermore, the analysis presented in Secs. 4.2, 4.3 and 4.4 show how the ideal gas analysis was performed. The ideal gas isobaric heat capacity is determined from the experimental data using Eq. 4.8. The research goal regarding the validity of the models was met in Sec. 4.4, through the comparison between experimental data with literature or model data. From this analysis, it was shown that the thermodynamic models RefProp and StanMix do not deviate from the experimental data at the measured conditions. Furthermore, the comparison between the trends of the experimental and model data showed that both were similar.

The work has thus led to the conclusion that the models are able to qualitatively predict the thermodynamic properties of D4 at these elevated temperatures. However, the high sensitivity of the method used to obtain the ideal gas isobaric heat capacity results in large uncertainties. This reduces the accuracy of the experimental measurements results. The method as explained in this chapter is suitable for analysis of data obtained using highly accurate resonators, but results in large uncertainties when data is obtained through less accurate devices. Therefore, the second part of this thesis focuses on the development of an alternative analysis method for obtaining the ideal gas isobaric heat capacity. The goal is to attain a method less sensitive to fluctuations in the speed of sound, providing accurate results without requiring highly accurate and expensive equipment to measure the speed of sound.

5

Determining an alternative analysis method

The analysis conducted in Chap. 4 discussed the commonly used methodology for obtaining the ideal gas isobaric heat capacity for a fluid using experimentally determined speed of sound data. The sensitivity analysis discussed in Sec. 4.5, revealed the formation of an asymptote in the c_p^{IG} vs c^{IG} plane. This asymptote forms close to the obtained values for the ideal gas speed of sound for D4. This results in a significant deviation for the ideal gas isobaric heat capacity due to an insignificant fluctuation in the obtained ideal gas speed of sound, demonstrated by the example given in Tab. 4.10. Furthermore, this means that for measurements with an uncertainty similar to OVAR, the results possess large error bounds.

Because of the asymptotic behaviour of Eq. 4.8, a new method is created with the goal of reducing the sensitivity between the speed of sound data and ideal gas heat capacity. The overview of acoustic measurement techniques provided in Chap. 2, mainly focused on the conventional analysis method, which is used for the analysis of the experimental data in Chap 4. However, in Sec. 2.1.2 a numerical method is introduced, which is used to obtain the real gas isobaric heat capacity from speed of sound measurements. This method is created by Trusler [54, 55] and was used to determine c_p for methane in Trusler's research. This method is investigated as an alternative analysis method to obtain the ideal gas isobaric speed of sound in this chapter, because the results of this method allow for the establishment of a relation between the isobaric heat capacity and the pressure. This part of the thesis investigates how this established relation can be used to determine the ideal gas isobaric heat capacity. Therefore, a test on the accuracy of the newly developed method is also provided.

This chapter starts with the derivation of the equations required to solve the numerical method, given in Sec 5.1. This is followed by Sec. 5.2, where the additional step required to obtain the ideal gas isobaric heat capacity is introduced and verification of this additional step is performed. Section 5.3 focuses on the development of the program required for numerical integration and addresses several numerical differentiation and integration techniques. Section 5.4 discusses the validation of the newly developed method for obtaining c_p^{IG}. This chapter is finalized by a chapter summary given in Sec. 5.5

5.1. Derivation of the equations used to solve for the heat capacity

The method originated from a study by Trusler, in which a speed of sound experiment similar to the one discussed in Chap. 4 is conducted using a resonator for the substance methane [54]. Besides performing the same ideal gas analysis for the ideal gas isobaric heat capacity, the actual isobaric heat capacity is also obtained using a numerical integration method. The essence of the method revolves around two equations, which must be solved simultaneously. The first equation relates the heat capacity to the speed of sound, given by

$$c^{-2} = \frac{M}{RTZ^2}\left[\left(Z - p\left(\frac{\partial Z}{\partial p}\right)_T\right) - \frac{R}{c_p M}\left(Z + T\left(\frac{\partial Z}{\partial T}\right)_p\right)^2\right], \tag{5.1}$$

where Z is the compressibility factor and c_p is the isobaric heat capacity. The second equation in the system of equations is given by

$$\left(\frac{\partial c_p}{\partial p}\right)_T = -\frac{R}{Mp}\left[2T\left(\frac{\partial Z}{\partial T}\right)_p + T^2\left(\frac{\partial^2 Z}{\partial T^2}\right)_p\right]. \tag{5.2}$$

This equation relates the second partial derivative of the compressibility factor with temperature to the first partial derivative of the isobaric heat capacity with temperature. The solving of this system of equations, requires appropriate initial values. For the initial values a choice must be made between c_p, Z and $\left(\frac{\partial Z}{\partial T}\right)_p$. Since the objective of using this method is to obtain c_p^{IG} through c_p, Z and $\left(\frac{\partial Z}{\partial T}\right)_p$ must be selected as initial values. Numerical integration is required to determine the initial values for the next temperature to be analysed and makes use of the results obtained by Eq. 5.2.

5.1.1. Derivation of the equations

The most important steps of the derivation of Eqs. 5.1 and 5.2 are provided in this subsection. The complete derivation can be found in Appendix D. The derivation starts with the definition of the speed of sound given by [45, 55]:

$$c^2 \equiv \left(\frac{\partial p}{\partial \rho}\right)_s. \tag{5.3}$$

Using algebraic and thermodynamic manipulations it follows that the speed of sound can be expressed as:

$$c^2 = \left[\left(\frac{\partial \rho}{\partial p}\right)_T - \frac{T}{\rho^2 c_p}\left(\frac{\partial p}{\partial \rho}\right)_T^2\left(\frac{\partial \rho}{\partial T}\right)_p^2\right]^{-1}. \tag{5.4}$$

It is convenient to eliminate the ρ in Eq. 5.4, by introducing the compressibility factor, Z, as this factor varies less than the density. The compressibility factor is given by

$$Z = \frac{Mp}{\rho R T}. \tag{5.5}$$

Completion of this manipulation results in the following relation corresponding to Eq. 5.1.

$$c^{-2} = \frac{M}{RTZ^2}\left[\left(Z - p\left(\frac{\partial Z}{\partial p}\right)_T\right) - \frac{R}{c_p M}\left(Z + T\left(\frac{\partial Z}{\partial T}\right)_p\right)^2\right]. \tag{5.6}$$

The derivation of Eq. 5.2 originates from the need of an expression for the heat capacities, in order to relate the speed of sound to an equation of state [7, 55]. For the isobaric heat capacity, the following relation is used:

$$c_p = c_{p,0} + \int_{p,0}^{p}\left(\frac{\partial c_p}{\partial p}\right)_T \mathrm{d}p, \tag{5.7}$$

where the partial differential $\left(\frac{\partial c_p}{\partial p}\right)_T \mathrm{d}p$ is expressed as:

$$\left(\frac{\partial c_p}{\partial p}\right)_T = -T\left(\frac{\partial^2 \rho^{-1}}{\partial T^2}\right)_p. \tag{5.8}$$

Further introducing the compressibility factor, results into

$$\left(\frac{\partial c_p}{\partial p}\right)_T = -\frac{R}{Mp}\left[2T\left(\frac{\partial Z}{\partial T}\right)_p + T^2\left(\frac{\partial^2 Z}{\partial T^2}\right)_p\right]. \tag{5.9}$$

Relations 5.6 and 5.9 need to be rewritten in order to be of use in the integration process. Equation5.6 is used in this process to determine the isobaric heat capacity. Rewriting Eq. 5.6 requires c_p to be isolated on the left-hand side, this is given by:

$$c_p = \left[\frac{M}{R}\frac{\left(Z - p\left(\frac{\partial Z}{\partial p}\right)_T\right)}{\left(Z + T\left(\frac{\partial Z}{\partial T}\right)_p\right)^2} - \frac{TZ^2}{c^2\left(Z + T\left(\frac{\partial Z}{\partial T}\right)_p\right)^2}\right]^{-1}. \tag{5.10}$$

Similarly, Eq. 5.9 requires isolation of $\left(\frac{\partial^2 Z}{\partial T^2}\right)_p$ on the left-hand side, in order to provide data for the integration steps, required for the determining the initial conditions at the next temperature step. This rewritten relation is given by:

$$\left(\frac{\partial^2 Z}{\partial T^2}\right)_p = -\frac{Mp}{RT^2}\left(\frac{\partial c_p}{\partial p}\right)_T - \frac{2}{T}\left(\frac{\partial Z}{\partial T}\right)_p. \tag{5.11}$$

The relations given by Equations 5.10 and 5.11 are used in the integration process to not only determine the values for c_p and $\left(\frac{\partial^2 Z}{\partial T^2}\right)_p$, but also for Z and $\left(\frac{\partial Z}{\partial T}\right)_p$ for the next temperature step.

5.1.2. The process of solving the equations

Solving the system of equations given by Eqs. 5.10 and 5.11 requires not only the initial values, but also the experimentally obtained speed of sound data, and the temperature and pressure data. The study conducted by Trusler [54] for methane used data from literature to determine the initial conditions for Z and $\left(\frac{\partial Z}{\partial T}\right)_p$ along the starting isotherm. It should be noted that the integration process is required to start at the lowest measured isotherm to the highest isotherm. Knowing the term Z along an isotherm, allows for differentiation with respect to pressure, resulting in $\left(\frac{\partial Z}{\partial p}\right)_T$. The measured speed of sound, the initial conditions and the derived term $\left(\frac{\partial Z}{\partial p}\right)_T$, provides enough information to determine c_p using Eq. 5.10.

The resulting values for c_p along the calculated isotherm are then differentiated with pressure, obtaining $\left(\frac{\partial c_p}{\partial p}\right)_T$. Equation 5.11 can then be solved with the known information of the specific isotherm at hand, resulting in $\left(\frac{\partial^2 Z}{\partial T^2}\right)_p$. In Trusler's article it is mentioned that the Euler method is suitable for integration, but other higher order methods can also be used. For the sake of simplicity, the Euler integration scheme is used to demonstrate the integration process. Integration for Z requires the use of both $\left(\frac{\partial Z}{\partial T}\right)_p$ and $\left(\frac{\partial^2 Z}{\partial T^2}\right)_p$. Therefore, Z_{n+1} is determined via a second order Taylor expansion, while $\left(\frac{\partial Z}{\partial T}\right)_p$ is only determined with a first order Taylor expansion, following a standard forward Euler integration scheme. The integration procedure for Z is shown by:

$$Z_{n+1} = Z_n + \mathrm{d}T\left(\frac{\partial Z}{\partial T}\right)_{p,n} + \frac{1}{2}\mathrm{d}T^2\left(\frac{\partial^2 Z}{\partial T^2}\right)_{p,n}. \tag{5.12}$$

$\left(\frac{\partial Z}{\partial T}\right)_p$ is integrated by:

$$\left(\frac{\partial Z}{\partial T}\right)_{p,n+1} = \left(\frac{\partial Z}{\partial T}\right)_{p,n} + \mathrm{d}T\left(\frac{\partial^2 Z}{\partial T^2}\right)_{p,n}. \tag{5.13}$$

These integration schemes are introduced by Trusler [54] and Estrada-Alexanders [17]. A more elaborate discussion on the integration schemes can be found in Sec. 5.3, where the implementation of several integration schemes is discussed.

5.2. Additional step to determine the ideal gas isobaric heat capacity

In Sec. 5.1, the two equations that need to be solved for the alternative analysis for the speed of sound data were introduced, together with the derivation of these relations. The equations and process introduced thus far have followed the method created by Trusler for the analysis of methane. However, the step required to determine c_p^{IG} has not been introduced yet. Therefore, this section addresses the additional step required to determine the ideal gas isobaric heat capacity from the relations specified previously.

This additional step is derived from the method to obtain the ideal gas speed of sound as shown in Chap. 4. In Chap. 4, the experimentally measured speed of sound data was fitted to a quadratic function, in order to extrapolate to the ideal gas region, $p \rightarrow 0$. The output obtained from Eq. 5.10 allows a similar relation to be established along the specific isotherm, namely between pressure and the isobaric heat capacity. Following a polynomial fit the following relation can be obtained:

$$c_p = a + b \cdot p + c \cdot p^2 + d \cdot p^3 + \ldots. \tag{5.14}$$

In this equation the coefficients a, b, c, d, etc. are obtained through the fitting procedure. In the ideal gas limit (where $p \rightarrow 0$) this relation reduces to:

$$c_p^{IG} = a. \tag{5.15}$$

Such that the coefficient obtained for a directly equals the ideal gas isobaric heat capacity for the specific isotherm measured.

5.3. Building the program

In Subsec. 5.1.2, a brief overview of the steps required to solve the equations was given. In this section the entire process from the experimental data to the ideal gas isobaric heat capacity is described, further elaborating on the steps described in Subsec. 5.1.2. The steps described in this section, show the steps the Matlab program follows for solving of Eqs. 5.10 and 5.11. Several differentiation and integration methods are addressed, indicating the influence these have on solving the equations. This section concludes with a discussion on the stability conditions of the program when used for methane.

5.3.1. Algorithm of the computational model

The method devised earlier in this chapter is intended for the analysis of experimentally obtained speed of sound data for a given substance. The method requires a homogeneous data set in order to work as intended. The same pressure range should be analysed for all isotherms, spaced by a constant pressure step size. The isotherms should also be separated with a constant step size. This results in a "square" domain for which the integration will be performed. It should be noted that this can only be done for a saturated vapour and no mixed phase data points should be used.

In Fig. 5.1 the "square" domain for methane is shown. In the figure the vertical lines represent the isotherms of the experimentally determined speed of sound data by Trusler [54]. From the experimentally obtained data, the homogeneous data set is created by a third order fitting of the speed of sound and pressure data.

This polynomial was then used to determine the speed of sound along a homogeneous spaced pressure range, ranging from 10 bar up to 100 bar with a pressure step of 2 bar. This results in the square domain shown in Fig. 5.1.

The homogeneity of the fitted isotherms is used to determine the isobars indicated by the horizontal lines.

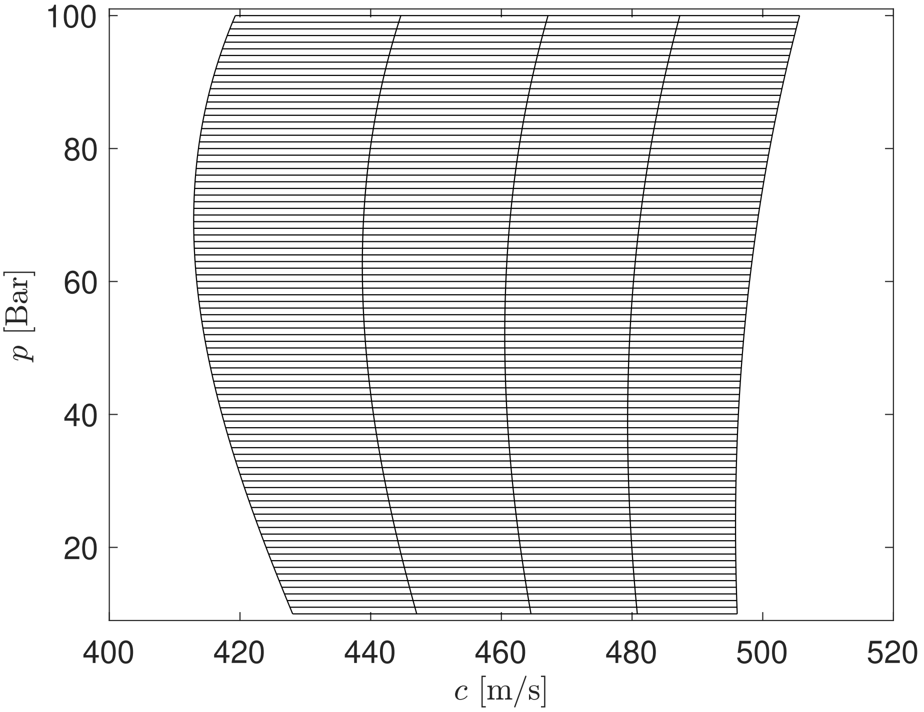

Figure 5.1: Speed of Sound vs. pressure for methane, obtained via data from Trusler [54]. The "square" domain is shown used for the integration process. The vertical lines represent the isotherms at T = 275 K to T = 375 K, respectively. The data for these isotherms are taken from Trusler and fitted to a third order polynomial

For the integration process a relatively small temperature step size is required $\mathrm{d}T \leq 1K$. These isobars are used to determine the speed of sound values for the isotherms that fall in between the measured isotherms. Trusler's method makes use of Lagrangian interpolation for this procedure, but a similar result can be achieved with polynomial fitting. Trusler made use of a fourth order interpolation method, therefore a fourth order polynomial is fitted for the results. This results in a fourth order relation between speed of sound and temperature for each isobar. This is shown in Fig. 5.2, where the red lines indicate the original isotherms analysed, determined from Trusler's data via fitting. The vertical black lines indicate the isotherms required to accurately integrate the data set. The temperature step shown in the figure is $\mathrm{d}T = 1K$.

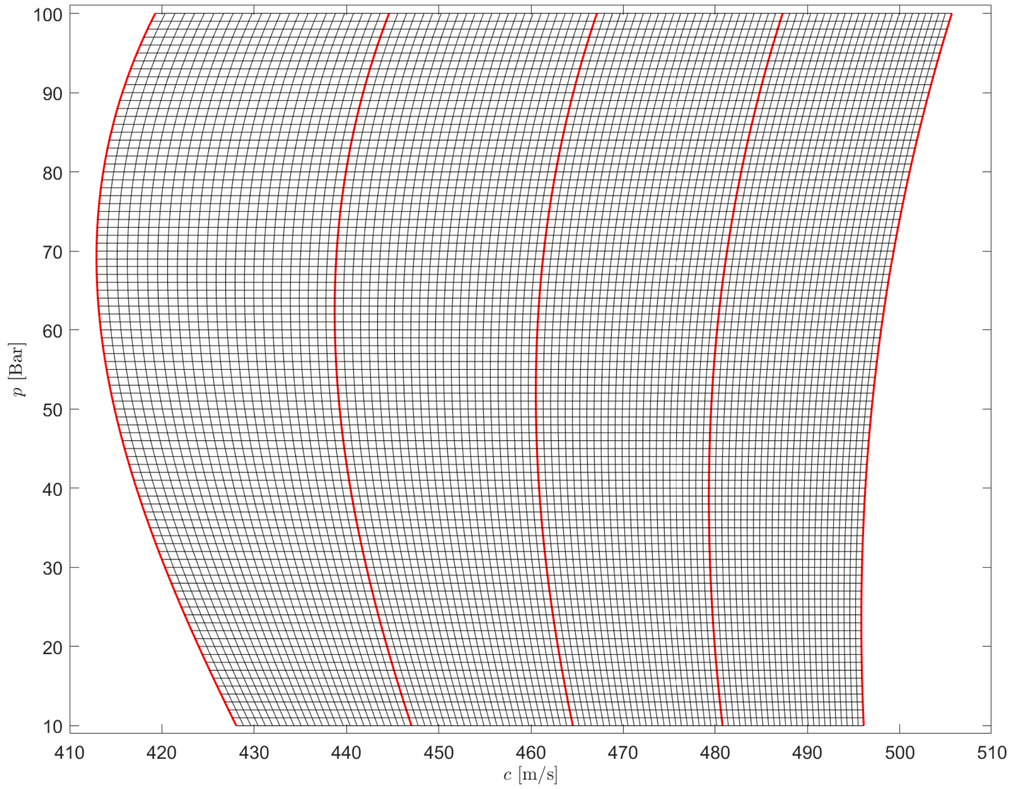

Figure 5.2: Speed of Sound vs. pressure obtained for methane via data from Trusler [54]. The red lines indicate the isotherms shown in Fig. 5.1, obtained using a quadratic fit on Trusler's data, the remaining vertical black lines show the isotherms obtained from quadratically fitting of the isobars.

The process described is performed before the integration of the data occurs, because the temperature and pressure ranges are known prior to integration. The speed of sound data for each isotherm can be determined *a priori* as well. The next step in the process is to determine the first set of initial values. In order to determine c_p, the terms Z and $\left(\frac{\partial Z}{\partial T}\right)_p$ are the initial values. The initial values for Z also provide the initial values for the partial derivatives of Z with respect to temperature and pressure. Therefore, Z is the only value obtained from the thermodynamic model RefProp. However, this model does not directly output the compressibility factor. Thus, the density of the fluid is obtained from the model for a certain temperature and pressure combination. The combination of density, temperature and pressure allows for the determination of Z, applying Eq. 5.5.

From Z, $\left(\frac{\partial Z}{\partial T}\right)_p$ is obtained through differentiation between two isotherms. For the second isotherm, spaced by $\mathrm{d}T$ as required for this differentiation, RefProp is also used to determine Z. The values obtained for Z from RefProp are only used to obtain the initial values for $\left(\frac{\partial Z}{\partial T}\right)_p$. Knowing Z for the initial isotherm, the term $\left(\frac{\partial Z}{\partial p}\right)_T$ is obtained by differentiation with respect to pressure along the starting isotherm.

With the known initial values and the speed of sound data for all isotherms, the integration loop is entered. The first step in this loop is to solve Eq. 5.10 in order to obtain c_p. Numerical differentiation of c_p results in $\left(\frac{\partial c_p}{\partial p}\right)_T$, which provides enough information to determine $\left(\frac{\partial^2 Z}{\partial p^2}\right)_T$, using Eq. 5.11. This is used for the integration for the next isotherm given by the temperature, $T_{n+1} = T_n + \mathrm{d}T$. The integration results in new values for Z and $\left(\frac{\partial Z}{\partial T}\right)_p$ and Z is required to be differentiated with pressure to obtain $\left(\frac{\partial Z}{\partial p}\right)_T$. This provides enough information to use Eqs. 5.10 and 5.11. In the same integration loop the ideal gas heat capacity is also determined, using the step introduced in Sec. 5.2. The determined data for c_p along each specific isotherm is then fitted accordingly, resulting in c_p^{IG} per isotherm.

5.3.2. Differentiation methods used and influence on the process

The method described earlier in this chapter requires numerical differentiation to obtain $\left(\frac{\partial Z}{\partial T}\right)_p$, $\left(\frac{\partial Z}{\partial p}\right)_T$ and $\left(\frac{\partial c_p}{\partial p}\right)_T$. Numerical differentiation techniques can introduce errors that can grow with each iteration, which causes the integration process to explode to unrealistic values after a certain number of iterations. This is problematic for the differentials determined using numerical differentiation in the integration loop.

The values for $\left(\frac{\partial Z}{\partial p}\right)_T$ and $\left(\frac{\partial c_p}{\partial p}\right)_T$ are most affected by this, because these values are determined by numerical differentiation in each iteration. The term $\left(\frac{\partial Z}{\partial T}\right)_p$ is only determined once during the initiation of the integration process via numerical differentiation. Therefore, the analysis presented in this subsection is relevant for the derivatives $\left(\frac{\partial Z}{\partial p}\right)_T$ and $\left(\frac{\partial c_p}{\partial p}\right)_T$.

The simplest form of numerical differentiation, is determining the slope between two discrete points. The problem with this method is that differentiation of n number of points results in $n-1$ amount differentiated points. Inevitably, this reduction of data points per differentiation steps results to a point that no data is left. Therefore, different differentiation schemes are tried to remove this effect of the deprivation of data. One of such methods tried is the built-in numerical differentiation function of Matlab, called the gradient function. Even though this solves the problem regarding the reduction of data points, it was observed that the derivatives for $n = 1$ and $n = n$ differ from the rest of the derivatives. The difference was observed by a sudden change of curvature shown for the derivatives of $n = 2$ and $n = n-1$. Figure 4.8 shows the partial derivative of the molar heat capacity with respect to pressure for the initial isotherm at T = 275 K. The derivative is determined using the gradient function embedded in Matlab (Version R2020a). The red circles in the figure indicate the region where the gradient function is insufficient in computing the correct derivative, observed as a sudden change in slope at both ends of the isotherm. For the initial few steps this effect causes insignificant errors in the calculations. However, in order to cover the entire temperature range with $\mathrm{d}T \leq 1K$ at least 100 steps are required. Resulting in an increasingly larger error per step, causing unstable results for the integration sequence. For this reason, the built-in gradient function was discarded as the differentiation method.

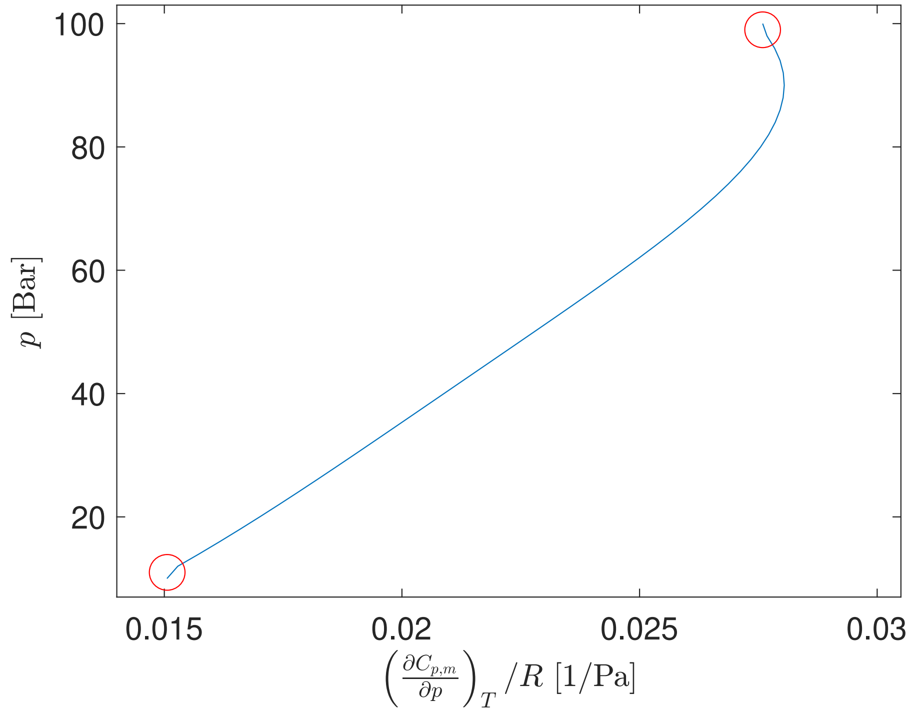

Figure 5.3: $\left(\frac{\partial C_{p,m}}{\partial p}\right)_T$ vs p, indicating the error caused by the gradient function embedded in Matlab at the tips of the isotherms.

The final method considered for numerical differentiation is that of Finite differences. Finite differences provide highly accurate results and the variation between forward, central and backward schemes allow n outputs. The method of determining the slope between two points is in essence the first order forward finite difference. However, in this thesis the term finite differences refers to the use of central, forward and backward finite differences, using the higher order accuracy coefficients. Initially it was decided that only the forward and backward finite differences would be used. The forward finite difference method would determine the derivatives for points $n = 1...n/2$, while the backward finite difference scheme was used to determine the derivatives for the second half, $n = n/2+1...n$.

Implementing the finite difference in this way causes an unstable response, which originates from a minute discontinuity between the solutions of the forward and backward schemes at the midway point. This difference between the two schemes only becomes visible when the $\left(\frac{\partial^2 c_p}{\partial p^2}\right)_T$ is determined for the initial conditions. In Fig. 5.4 $\left(\frac{\partial^2 c_p}{\partial p^2}\right)_T$ is shown for the initial isotherm determined by using of the method described above, using forward and backward finite difference to determine the derivative. From the figure it is clear the oscillations are centred around the midpoint of the isotherm, corresponding to the cross-over point where the switch between forward to backward finite difference is located. Even though the oscillations are only visible for $\left(\frac{\partial^2 c_p}{\partial p^2}\right)_T$ at the initial isotherm, after several integration steps these oscillations will have gained in magnitude. This results in an unstable response for the integration process.

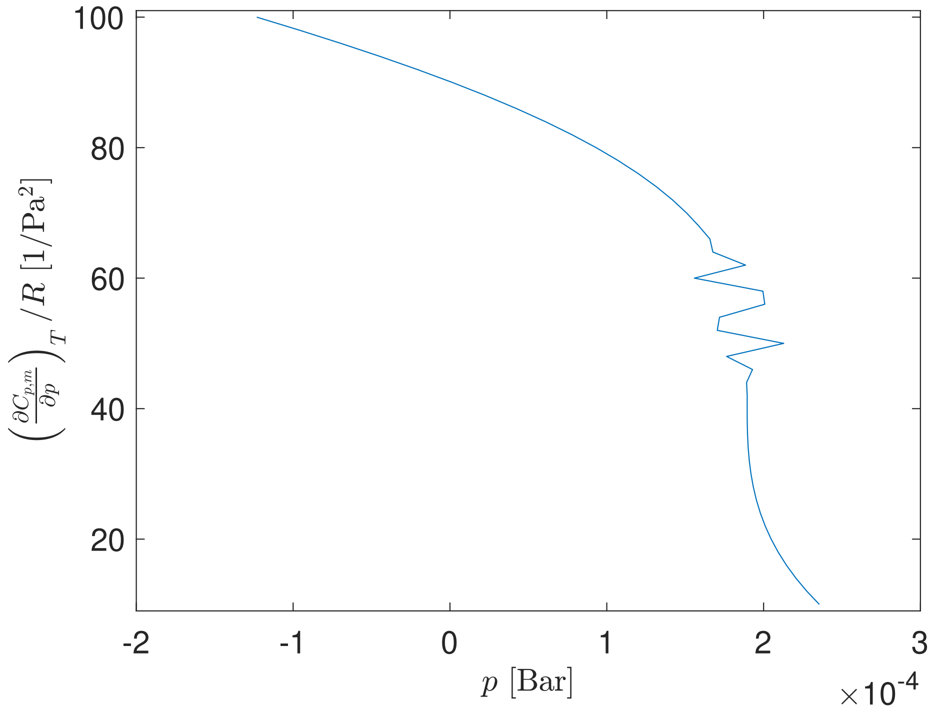

Figure 5.4: $\left(\frac{\partial^2 c_p}{\partial p^2}\right)_T$ for the initial isotherm of methane at T = 275 K. Oscillations are observed centred around the midpoint of the isotherm, corresponding to the cross-over point between the forward and backward finite difference scheme.

The method using only forward and backward method results in an unstable response. As such a switch was made to a second order central finite difference scheme, applied for all points except the first and last point of each isotherm. The end points of the isotherm are determined using forward and backward finite differences. The forward finite difference is used to determine the lowest pressure point, uses the standard coefficients for second order accuracy, given by:

$$\frac{\mathrm{d}y}{\mathrm{d}x} = \frac{-\frac{3}{2}f_n + 2f_{n+1} - \frac{1}{2}f_{n+2}}{\mathrm{d}x} + \mathcal{O}(\mathrm{d}x^2). \tag{5.16}$$

The second order accurate central order finite difference is given by:

$$\frac{\mathrm{d}y}{\mathrm{d}x} = \frac{-\frac{1}{2}f_{n-1} + \frac{1}{2}f_{n+1}}{\mathrm{d}x} + \mathcal{O}(\mathrm{d}x^2). \tag{5.17}$$

The subscripts $n-1$ and $n+1$ refer to the points that come before and after the point that is being determined. A modified version of the second order backward finite difference scheme is used to determine the final pressure point per isotherm. This modified version was obtained from Estrada-Alexanders [17] and is still of second order, but uses different coefficients compared to the standard coefficients. The formula used to determine the backward finite difference of the highest pressure point is given by:

$$\frac{\mathrm{d}y}{\mathrm{d}x} = \frac{2f_n - \frac{7}{2}f_{n-1} + 2f_{n-2} - \frac{1}{2}f_{n-3}}{\mathrm{d}x} + \mathcal{O}(\mathrm{d}x^2). \tag{5.18}$$

In all three formula's the term $\mathcal{O}(\mathrm{d}x^2)$ represents the truncation error. These are neglected in the analysis process. The three equations shown produce a numerically stable solution for methane. It should be noted that the pressure step size for each isotherm also governs the stability of the solution. The stability conditions of the model are the topic of discussion in Subsec. 5.3.4.

5.3.3. Integration schemes used and influence on the process

In Subsec. 5.1.2 the integration scheme defined by Trusler was briefly discussed, showing the simple Euler scheme used for integration. This integration method can be improved by the introduction of a predictor-corrector algorithm [54]. This predictor-corrector algorithm makes use of an intermediate calculation for a temperature located between T_n and T_{n+1}, resulting in an improvement of the truncation error, from $\mathcal{O}(\mathrm{dT}^3)$ to $\mathcal{O}(\mathrm{dT}^4)$.

The known sensitivity of D4 (shown in Chap 4) requires a robust integration scheme and the use of a predictor-corrector algorithm as recommended by Trusler. Therefore, the standard Runge-Kutta integration scheme is implemented in the program. The standard Runge-Kutta integration scheme is given by [10]

$$y_{n+1} = y_n + \left(\frac{K_{n,1} + 2K_{n,2} + 2K_{n,3} + K_{n,4}}{6}\right)\mathrm{d}T, \tag{5.19}$$

where

$$K_{n,1} = f(T_n, y_n), \tag{5.20}$$

$$K_{n,2} = f(T_n + \frac{1}{2}\mathrm{d}T, y_n + \frac{1}{2}\mathrm{d}TK_{n,1}), \tag{5.21}$$

$$K_{n,3} = f(T_n + \frac{1}{2}\mathrm{d}T, y_n + \frac{1}{2}\mathrm{d}TK_{n,2}), \tag{5.22}$$

$$K_{n,4} = f(T_n + \mathrm{d}T, y_n + \mathrm{d}TK_{n,3}). \tag{5.23}$$

The Runge-Kutta integration scheme requires the computation of Eqs. 5.10 and 5.11 and their accompanying terms four times per step. The values for $K_{n,1}$ are determined using the initial values. For $K_{n,2}$, $\left(\frac{\partial Z}{\partial T}\right)_p$ is determined $y_n + \frac{1}{2}\mathrm{d}TK_{n,1}$ and using $\left(\frac{\partial^2 Z}{\partial T^2}\right)_p$ determined at $K_{n,1}$. The value just obtained for $\left(\frac{\partial Z}{\partial T}\right)_p$ is used to determine Z for $K_{n,2}$, again using $y_n + \frac{1}{2}\mathrm{d}TK_{n,1}$. This acquires the intermediate values of the initial conditions required to solve Eqs. 5.10 and 5.11 , following the described process. This process is repeated for $K_{n,3}$ and $K_{n,4}$, using their respective equations for approximating the intermediate values.

After determining the values for $K_{n,1}$-$K_{n,4}$, the integration is performed using Eq. 5.19. For the initial values Z and $\left(\frac{\partial Z}{\partial T}\right)_p$ Eq. 5.19 changes into

$$Z_{n+1} = Z_n + \left(\frac{Z_{n,1} + 2Z_{n,2} + 2Z_{n,3} + Z_{n,4}}{6}\right)\mathrm{d}T, \tag{5.24}$$

and

$$\left(\frac{\partial Z}{\partial T}\right)_{p,n+1} = \left(\frac{\partial Z}{\partial T}\right)_{p,n} + \left(\frac{\left(\frac{\partial Z}{\partial T}\right)_{p,n,1} + 2\left(\frac{\partial Z}{\partial T}\right)_{p,n,2} + 2\left(\frac{\partial Z}{\partial T}\right)_{p,n,3} + \left(\frac{\partial Z}{\partial T}\right)_{p,n,4}}{6}\right)\mathrm{d}T, \tag{5.25}$$

respectively.

5.3.4. Defining the stability conditions for the alternative method

The stability of the integration method is influenced by various factors. The differentiation and integration methods, discussed previously, are two of these influencing factors. Another factor influencing the stability of the introduced method is the step size. For the described method, there are two step sizes that influence the stability and results of the integration process. The first one is the temperature step size along which the integration occurs. The second one is the pressure step used in the differentiation process to obtain $\left(\frac{\partial Z}{\partial p}\right)_T$ and $\left(\frac{\partial c_p}{\partial p}\right)_T$. In this subsection the effects of changing both is addressed.

The temperature step governs the integration process, described by Equations 5.24 and 5.25, as well as the initial derivative of $\left(\frac{\partial Z}{\partial T}\right)_p$. Trusler analysed the difference between a temperature increment of 0.1 K and 0.05 K. This resulted in identical results for the integration process described in this chapter [54]. This analysis is extended and ranges from $\mathrm{d}T$ = 10 K to $\mathrm{d}T = 1 \cdot 10^{-3}$ K, separated by a factor of 10. The pressure step size was kept constant at 5 bar. During this test the temperature increment of 0.1 K is used as a baseline value. Decreasing the temperature step size resulted in the same conclusion as drawn by Trusler, as no significant change in the results is observed. The results of the integration procedure using a temperature increment in the range $\mathrm{d}T$ = 0.1 K to $\mathrm{d}T = 1 \cdot 10^{-3}$ K are identical to each other. The only difference was found in the computation time, which increased from 20 seconds for $\mathrm{d}T$ = 0.1 K to 7 hours, for $\mathrm{d}T = 1 \cdot 10^{-3}$ K. By increasing the step size from 0.1 K to 1 K and to 10 K gave mixed results. For $\mathrm{d}T$ = 1 K, slight deviations are observed, while the temperature increment of dT = 10 K resulted in an unstable solution. The figures for c_p^{IG} for the temperature increments of dT = 10 K, dT = 0.1 K, d$T = 1 \cdot 10^{-3}$ K are shown in Fig. 5.5. In this figure it can be observed that the results for c_p^{IG} are similar when, dT = 0.1 K and d$T = 1 \cdot 10^{-3}$ K are used. The data required to draw the black lines are obtained from Trusler and are given in Appendix B, in Tab. B.6. Furthermore, the unstable solution obtained using a step size of 10 K, is shown in Fig. 5.5a. Due to the similarity in results several runs were left out of Fig. 5.5

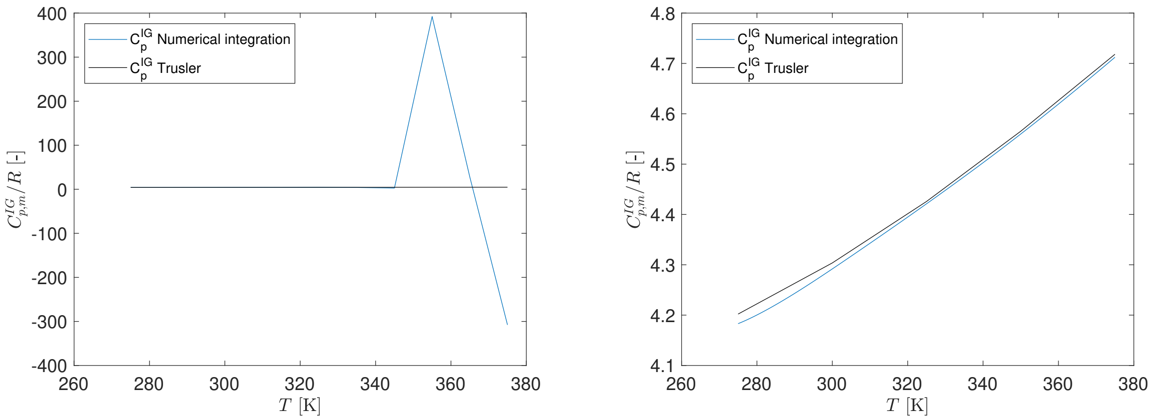

(a) dT = 10 K

(b) dT = 0.1 K

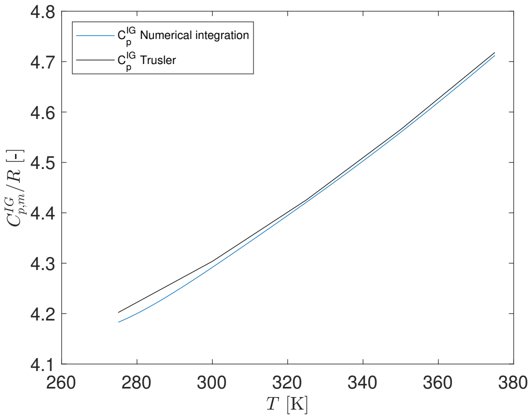

(c) dT = 0.001 K

Figure 5.5: $c_{p,m}^{IG}$ for varying temperature increments and comparing to Trusler's data [54]

From this analysis it was concluded that the recommended temperature increment of dT = 0.1 K should be used when solving the integration process. This is because a further reduction in step size does not significantly improve the results. Furthermore, the computational time remains acceptable, while using a larger step size quickly leads to an unstable solution.

The pressure step size also influences the stability of the integration method, due to the influence it has on the derivatives $\left(\frac{\partial Z}{\partial p}\right)_T$ and $\left(\frac{\partial c_p}{\partial p}\right)_T$. These are calculated four times per isotherm using the Runge-Kutta integration scheme. For methane, Trusler separated the isobars based on $p_c/10$, resulting in a pressure increment of dp = 4 bar [54]. In order to reduce the accuracy lost if an overly large step size is used, the upper limit for dp is set at 10 bar. During this analysis the temperature step size is kept constant at dT = 0.1 K.

The results of this analysis are shown in Fig. 5.6. From the figure it can be observed that using dp < 1 bar, results in an unstable solution of the integration process. In Fig. 5.6 it is shown that a pressure step size between 1-10 bar results in an identical and stable solution. The smallest possible step size in this range, dp = 1 bar, is used in order to best preserve the resolution of each of the isotherms.

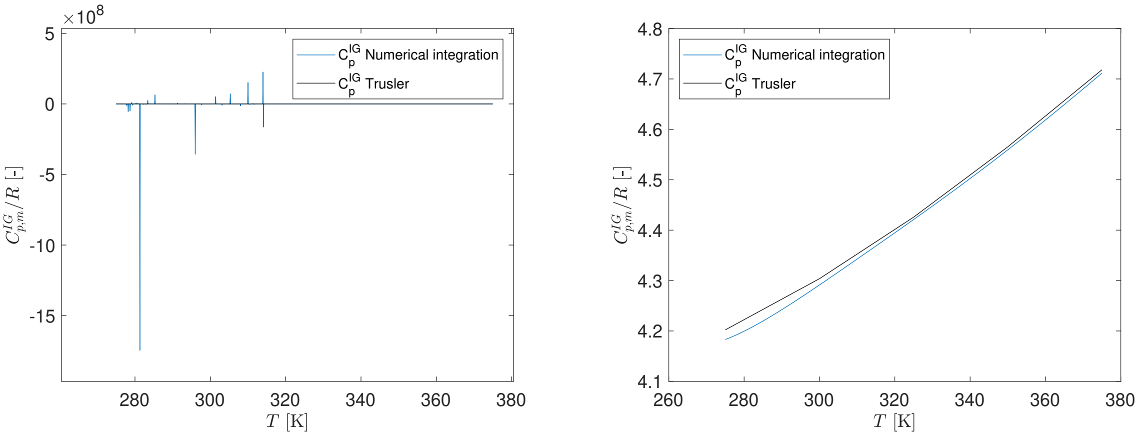

(a) dp = 0.1 bar

(b) dp = 1 bar

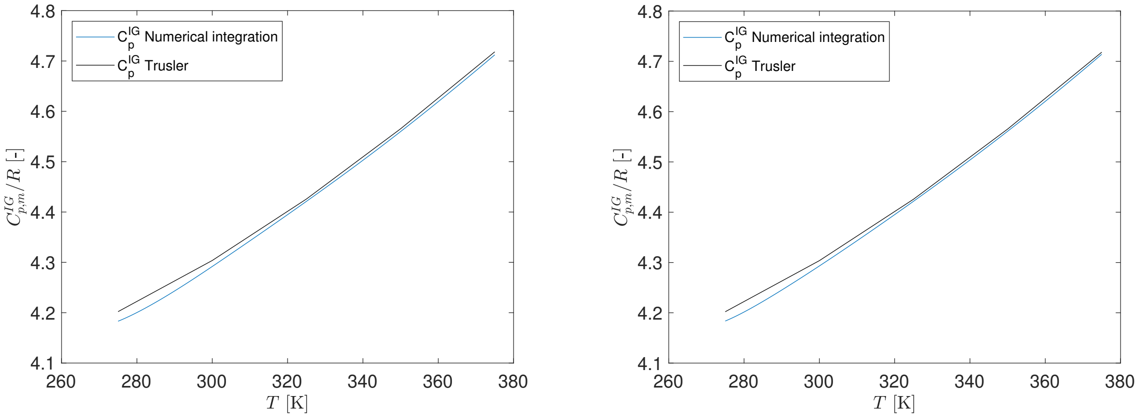

(c) dp = 5 bar

(d) dp = 10 bar

Figure 5.6: Altering the pressure step size, results in a stable and identical solution for dp 1-10 bar, while dp < 1 bar results in an unstable solution. Comparing the results of the alternative method with data obtained by Trusler [54]

5.3.5. Effects of the fitting order

Additionally, the introduced step requires the fitting of the isobaric heat capacity data as a function of the pressure. The heat capacity data is fitted to a polynomial, given by Eq. 5.14. Varying the order of the polynomial also changes the result for the ideal gas point, given by a in Eq. 5.14. Figure 5.7a shows the lines obtained by fitting the heat capacity data for a second, third, fourth and fifth order polynomial. Fitting of a sixth or higher order polynomial resulted in similar results as the fifth order polynomial. The fitted results for these order fits are shown isolated in Fig. 5.7b, in order to make these more visible. The figure shows that the results of these higher order fits overlap. In order to prevent over-fitting of the data, the fifth order fit is chosen as the limit.

In Fig. 5.7a, it is seen that the order of the fit affects the results more on the lower temperature end than at the higher temperature end. This is related to the explanation given in Chap. 4 regarding the increasing curvature of the isotherms at lower temperatures. This increase in curvature at lower temperatures means that the errors of the fitted polynomials for those isotherms increase as well. The reduction for higher order isotherms is caused by the increased number of terms to be fitted, which results in a better approximation of the curvature of the isotherm. This decrease in magnitude of the curvature is also shown in Fig. 5.8, where the second derivative of the second order fit is plotted for all the analysed isotherms.

Furthermore, a slight oscillation is present in the results fitted to a second, third or fourth order polynomial, shown in Fig. 5.7a. This is in contrast with the non-oscillating curve shown for the fifth or higher order polynomials in Fig. 5.8. This oscillating phenomenon for the lower order fits is numerically induced, as the results obtained from Trusler do not show these oscillations. The fifth order fitting method is used in the program for obtaining the ideal gas isobaric heat capacity, because it does not show these oscillations. Furthermore, the fifth order fitting method provides a more accurate solution compared to the lower order polynomials and limits the degree of overfitting.

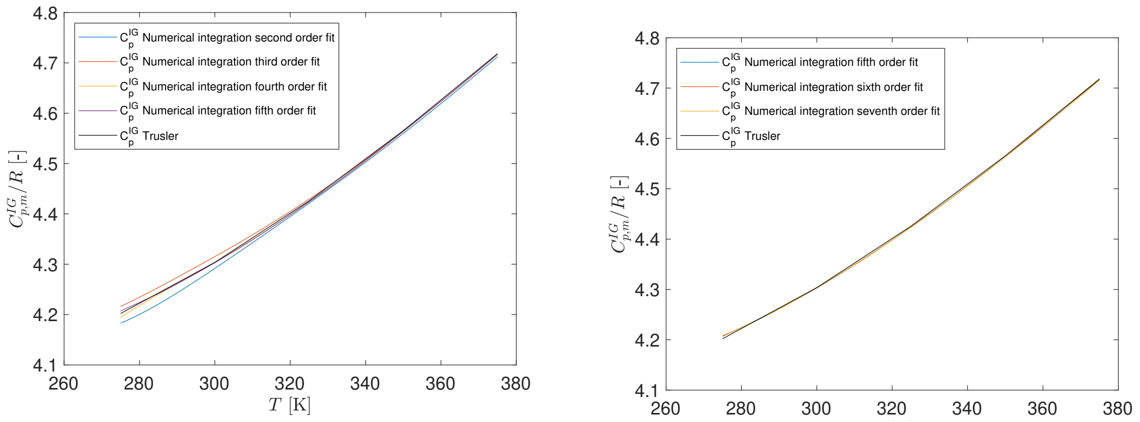

(a) c_p^{IG}/R, showing the different results obtained for using a different order polynomial function during the fitting process vs Trusler's results [54]

(b) c_p^{IG}/R, showing the result of the fifth, sixth and seventh order fit vs Trusler's results[54]

Figure 5.7: Effects of varying the fitting order of c_p

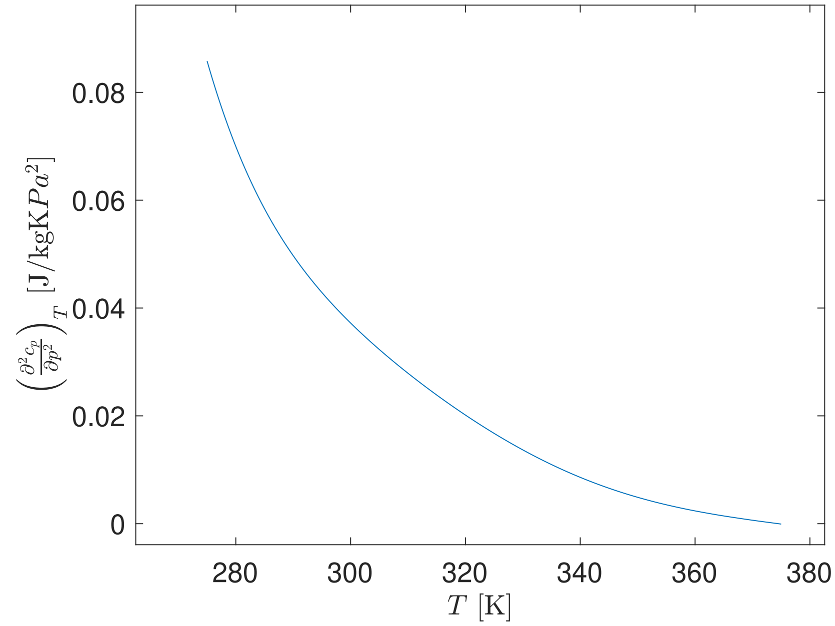

Figure 5.8: The second derivative of c_p with respect to pressure. Taken from the quadratic fitted curves for c_p. Indicating the decreasing magnitude of the curvature with increasing temperatures

5.4. Validation of the alternative method using methane

In Subsec. 5.1.2 the parameters of the integration affecting the stability were discussed. This showed that the integration procedure follows the Runge-Kutta scheme, with temperature and pressure step sizes of $\mathrm{d}T = 0.1$ K and $\mathrm{d}p = 1$ bar, respectively. This section features the validation of the method, using methane as the fluid to be analysed.

The validation process requires that not only the figure for c_p^{IG} is valid, but also for the figures Z and c_p. During the synthesis of the method, it was namely observed that even though there were significant discrepancies found for Z and c_p the values obtained for c_p^{IG} did not reflect those discrepancies. Thus, there are in essence three criteria that need to be met before the method is validated. The first criterion is the coherence of c_p^{IG} with respect to data from literature, as large deviation encountered result into an invalid result of the method. The second criterion is the coherence of Z with respect to data from literature, due to the importance of Z during the integration. The third and final criterion considered during the validation is the coherence of c_p with respect to data from literature, because of the fact that c_p^{IG} is directly determined from c_p by fitting. Thus, errors in c_p result in errors for c_p^{IG}. For all three variables the data used to for the comparisons is obtained from the article written by Trusler [54], investigating the speed of sound of methane. This data is found in Appendix B, in Tabs. B.1-B.5.

5.4.1. Ideal gas isobaric heat capacity vs Temperature

The developed approach adapted from a method specified by Trusler [54], was used to determine the ideal gas isobaric heat capacity differently than the method presented in Chap. 4. Following the steps explained in this chapter, the results of this alternative method are presented in Fig. 5.9. In the figure it is seen that the ideal gas isobaric heat capacity obtained using the alternative method closely follows the results presented by Trusler for methane [54]. Thus, it is shown that the alternative method can be used to determine the ideal gas isobaric heat capacity for methane.

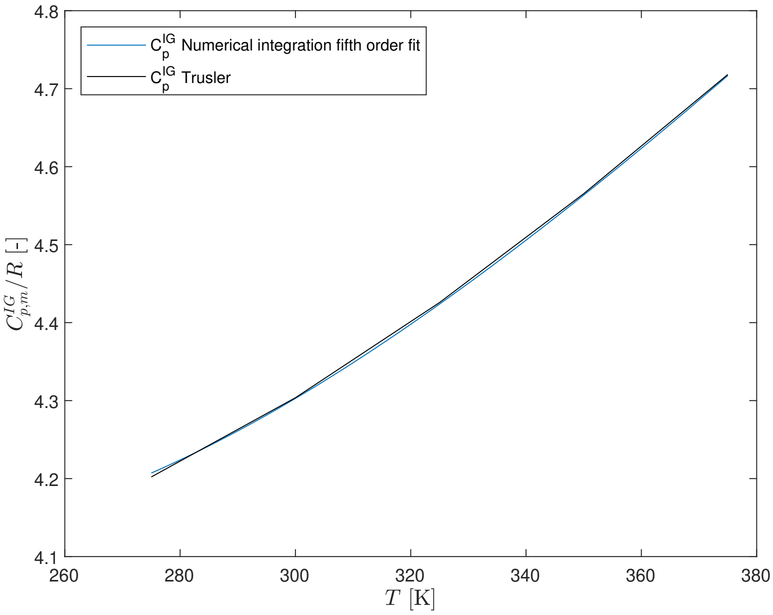

Figure 5.9: c_p^{IG} vs T, comparing the fifth order fit of the alternative method vs the results obtained by Trusler [54], using the conventional method explained in Chap. 4

5.4.2. Compressibility factor vs pressure

The compressibility factor is a direct result from the integration process and will show whether the integration is performed correctly or not. The results for Z obtained from the numerical integration are shown in Fig. 5.10. In this figure the data for Z is compared to the data obtained from Trusler. In the figure it can be seen that the numerically obtained results are identical to the results by Trusler. Therefore, no errors expressed in Z have affected the results for the ideal gas isobaric heat capacity.

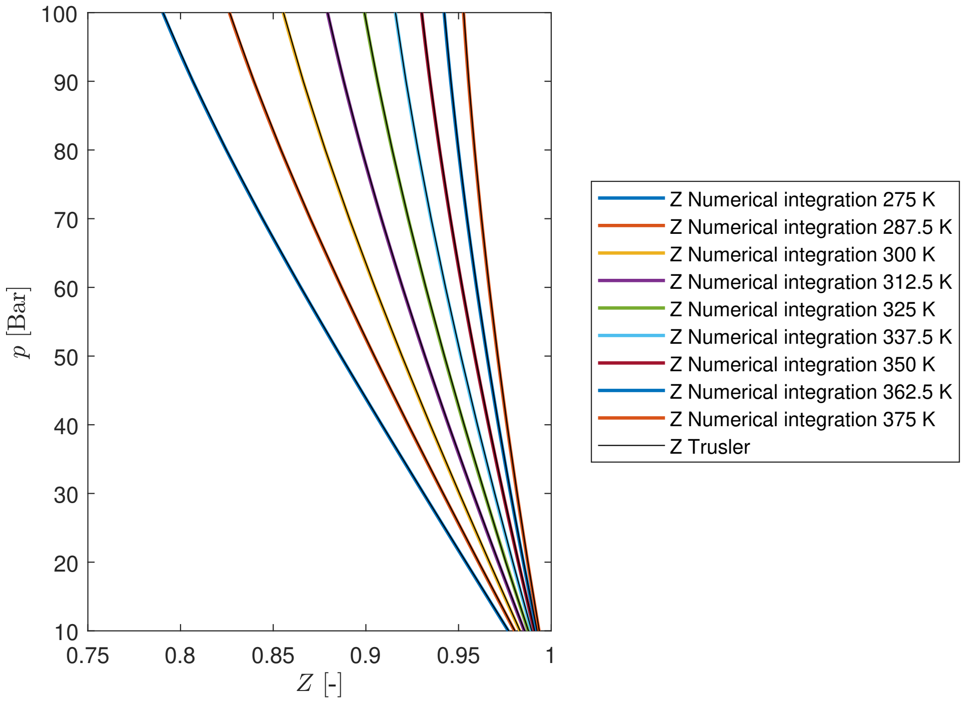

Figure 5.10: Z vs T, comparing the results obtained by numerical integration with the results obtained by [54], also via numerical integration

5.4.3. Isobaric heat capacity vs pressure

The newly developed method can only correctly determine the ideal gas isobaric heat capacity if the isobaric heat capacity is correctly obtained. The results for the numerically obtained c_p are shown in Fig. 5.11 and compared to Trusler's results [54]. From the figure it is observed that the lines match Trusler's results, with slight deviations. These deviations are caused by a different approach for determining the speed of sound for each of the isotherms and the different differentiation method used. The deviations from Trusler's lines increase with increasing pressure, as well as higher temperatures analysed. However, in the lower pressure section of the graph the numerically obtained values closely match those obtained from Trusler. This inspires confidence that the extrapolation to the ideal gas scenario is not greatly affected by the deviations seen at higher pressures.

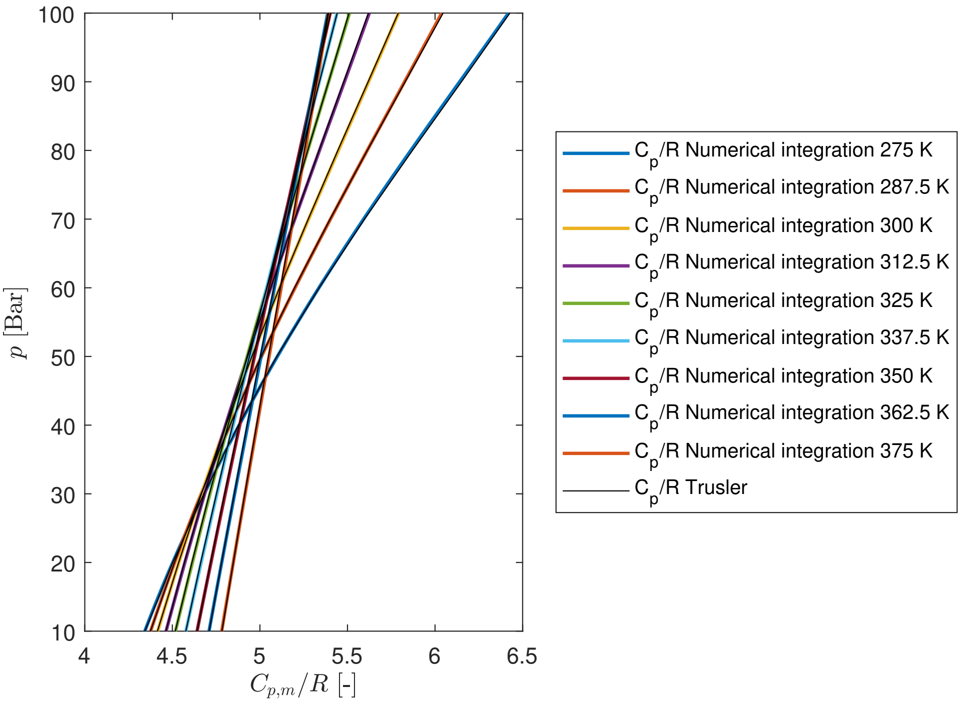

Figure 5.11: $C_{p,m}$ vs T, comparing the results obtained by numerical integration with the results obtained by [54], also via numerical integration

A similar figure to that presented by Fig. 5.11 was analysed by Estrada-Alexanders. In the article it is mentioned that oscillations occur at increasing temperatures [16]. These oscillations were also observed when the Lagrangian interpolation was used to estimate the speed of sound for the intermediate isotherms. However, changing this procedure to a polynomial fitted basis resulted in a reduction of the oscillation observed for the c_p data.

5.5. Summary

This chapter showed the development of the alternative analysis method of the ideal gas isobaric heat capacity using the speed of sound. The method was adapted from a method used by Trusler for the analysis of methane, with a new step added to determine the c_p^{IG}. The method by Trusler has as output the c_p, which can be fitted with respect to pressure in order to find c_p^{IG}. Following the steps described by Trusler and introducing a step to fit c_p gives the entire methodology required to find the c_p^{IG} from experimentally obtained speed of sound data. This requires a minimal of five isotherms are measured with 10+ homogeneously separated pressure points per isotherm.

Validation of this method has been performed by comparing data obtained by Trusler to the data obtained for the alternative method. This showed that the alternative fitting method works as intended for not only determining Z and c_p, but also for c_p^{IG}. c_p^{IG} was compared to the data obtained by Trusler using the conventional method.

6

Analysis of D4 using an alternative method

In Chap. 5, an alternative method for obtaining the ideal gas heat capacity from speed of sound data was introduced. The method is an adaptation of the method developed by Trusler [54]. Trusler used the method to determine the isobaric heat capacity of methane, from experimentally obtained speed of sound data. An additional step was added to this method to obtain the ideal gas isobaric heat capacity, as was shown in Chap. 5. The program that is written for this method was also verified and validated to work for methane in the previous chapter. However, this thesis regards the study of the fluid D4, so the validated program for methane is adapted to D4. This will provide an answer to the research question whether the alternative method is less sensitive to a fluctuation in speed of sound. The main focus of this chapter is on the adaptations of tailoring the program for D4 and the subsequent sensitivity analysis.

This chapter is structured as follows: Sec. 6.1 gives an overview of the changes made to the program in order to work for D4 and the identification of the stability region. This is followed by Sec. 6.2 with an analysis for the ideal gas isobaric heat capacity for D4, obtained by using the conventional and alternative method. The sensitivity analysis required to answer the research question is presented in Sec. 6.3.

6.1. Adapting the code to D4

In Sec. 5.3 the development of the alternative method is discussed. Even though the discussion on the development of the method presented in Sec. 5.3 is performed using methane, the topics addressed are also applicable to D4. Because D4 is a difference substance, the temperature and pressure ranges used are altered, thus new stability criteria are required to be found. This section touches upon the integration region used for D4, the integration and differentiation methods and the stability of the program.

6.1.1. Data input used for the analysis

In Sec. 5.3 the "square" region of integration was shown for methane. The conditions analysed for methane by Trusler [54], ran from 10 - 100 bar, for temperatures ranging from 275 K to 375K. For methane, these temperatures and pressure range are supercritical, as T_c = 190.6 K and p_c = 46.1 bar[1]. The analysis presented in Chap. 5 therefore did not have to consider conditions approaching the dew line. This differs from the conditions that are analysed for D4 using the alternative method. These conditions are closely related to the conditions of the conducted experiment of Chap. 4. For D4 the temperature range that is analysed is between 500 and 600 K. The critical temperature for D4 is ≈585 K, therefore most of the isotherms are sub critical. This limits the pressure range that can be used, because dual phase conditions must be avoided. The pressure range for the analysis of D4 is therefore between 0.5-1.5 bar; similar to the pressure range of the conducted experiment. The lower pressure limit is determined on the basis that for a realistic experiment the noise-to-signal ration increases significantly at lower pressures, therefore 0.5 bar is taken as this limit.

6.1.2. Differentiation and Integration schemes for D4

The several differentiation and integration schemes which were tried, are elaborately discussed in Sec. 5.3. These schemes are not changed during the adaptation of the program for D4. The numerical differentiation

---

[1] NIST page for methane `https://webbook.nist.gov/cgi/cbook.cgi?ID=C74828&Mask=4`, accessed on 7-12-2021

scheme used is the second order finite difference scheme, including the adaptation mentioned by Estrada-Alexanders [17]. The integration scheme for D4 remained the standard Runge-Kutta scheme. In Chap. 5, it was seen that the differentiation caused an unstable response due to the increasing error found in the second derivative of the c_p with pressure. This was resolved by the adaptation mentioned by Estrada-Alexanders. However, for D4 the results remained unstable, due to the error induced by the differentiation. This error is related to the pressure step size used for D4, $\mathrm{d}p = 0.01$ bar, which is much smaller than $1/10\ p_c$ recommended by Trusler [54]. The critical pressure of D4 is 13.20 bar[2], following Trusler's recommendation this results in a pressure step of 1.32 bar. This is an impractical step size considering the pressure range of 1 bar, due to the pressure limit imposed for the analysis of subcritical isotherms. In Chap. 5 it was shown that this unstable behaviour originates from the numerical differentiation method, thus showing that the results were altered by a non-physical effect. Because the underlying cause is non-physical, the instability was removed by performing a polynomial fit of the term $\left(\frac{\partial c_p}{\partial p}\right)_T$.

This term is fitted, because the oscillations originate from the determination of this term.

Besides introducing this intermediate fit of $\left(\frac{\partial c_p}{\partial p}\right)_T$, the program remained the same as the program verified and validated for methane. To use the method for any fluid, it is recommended to determine the speed of sound for five or more homogeneously separated experimentally obtained isotherms, for a homogeneously spaced pressure range. The experimental speed of sound data should then be used to determine the speed of sound for all the intermediate isotherms used for integration of the squared domain. Using the alternative method, the isobaric heat capacity for each point of the domain can be obtained. This can then be used to determine the ideal gas isobaric heat capacity, using a polynomial fit of the pressure and isobaric heat capacity data.

6.1.3. Determining the stability region of the program for D4

In the previous chapter, the effect of the step sizes for pressure and temperature are elaborately discussed. Due to the inclusion of the additional fitting procedure used to remove the unstable results, the effect of altering the pressure step size on the stability is reduced. The pressure step size is taken at 0.01 bar, so that the plotted figures in the pressure range of 0.5-1.5 bar have a clear resolution, resulting in smooth curves. The temperature step size remains of importance to the integration process. As discussed in Chap. 5, an increase of the temperature step-size could lead to an unstable result, due to the errors caused by an overly large step size for the differentials with respect to temperature. It is described in Chap. 5 that decreasing the temperature step-size slightly improves the accuracy of the results, but this comes at the price of an increased computational time. The temperature step size is therefore kept at 0.1 K, which provides accurate results while limiting the computational time.

6.1.4. Effects of starting conditions

The results for methane, shown in Chap. 5, indicate that the alternative analysis method is able to accurately determine the ideal gas isobaric heat capacity for the given temperature range. The temperature range used for methane in Chap. 5 ranges from 275 K to 375 K, which is entirely supercritical. For D4 the temperature range used for the analysis in this chapter ranges from 500 K to 600 K. However, the critical temperature $T_c \approx 585K$, meaning that most of the isotherms are subcritical. The effects of changing the starting conditions are analysed, because of this difference with methane. This analysis aims to reveal the difference between the subcritical and supercritical starting conditions. In order to perform this comparison a sufficiently large temperature range is required. Therefore, the temperature range starting at subcritical starting conditions ranges from 500 K to 670 K, while the supercritical temperature range used ranges from 590 K to 670 K.

Figure 6.1 shows the c_p vs p plane. It is observed that the results in Fig. 6.1a show relatively large deviations between the model data, compared to Fig. 6.1b. The cause of this difference is irrespective of the amount of integration steps, because no constantly increasing deviations are visible in Fig. 6.1. The actual cause of the increasing error with decreasing starting temperature is found in $\left[\frac{\partial c_p}{\partial p}\right]_T$ for the initial conditions. This is shown in Figs. 6.2a and 6.2b for the starting temperatures of 500 K and 590 K respectively. From both figures a periodic response is seen, signifying that the slope of Figs. 6.1a and 6.1b are oscillating. However, these oscillations are difficult to observe in Fig. 6.1, due the low values for $\left[\frac{\partial c_p}{\partial p}\right]_T$. Even though both Figs. 6.1a and 6.1b show oscillations, the amplitude of the oscillations shown in Fig. 6.1a is roughly 2 to 3 times larger than those shown in Fig. 6.1b. Furthermore, the period of the oscillation in Fig. 6.1a is shorter than that of Fig. 6.1b.

---

[2] NIST page for D4 `https://webbook.nist.gov/cgi/inchi?ID=C556672&Mask=4`, accessed on 25-1-2022

These are valuable observations due to the influence of term $\left[\frac{\partial c_p}{\partial p}\right]_T$ has on the integration, because of the presence in Eq. 5.11.

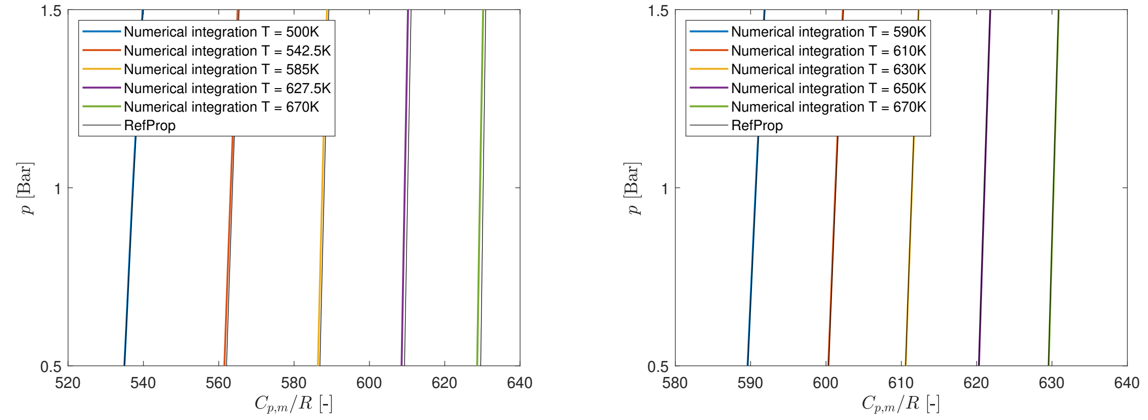

(a) 500 K - 670 K

(b) 590 K- 670 K

Figure 6.1: Comparing $C_{p,m}$ vs p for different temperature ranges, in order to identify the effect of changing the starting temperature

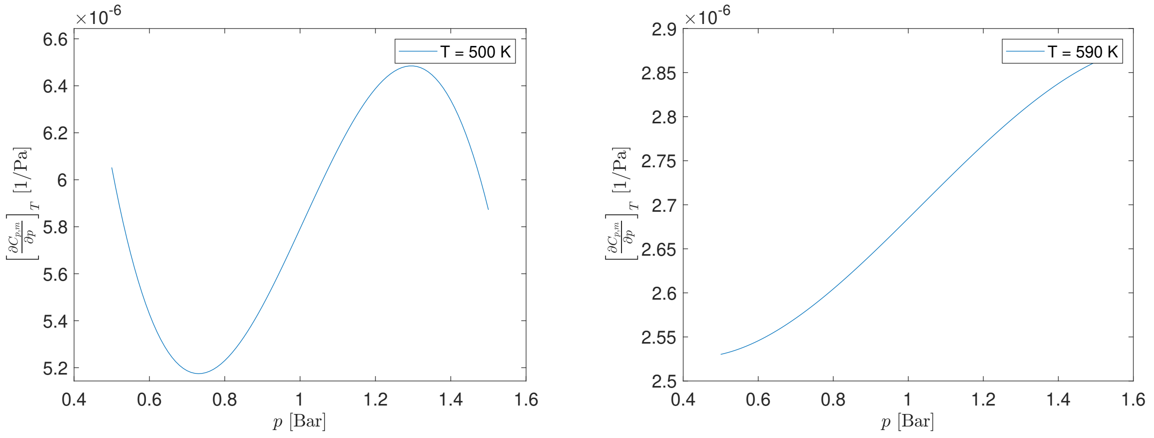

(a) $\left[\frac{\partial C_{p,m}}{\partial p}\right]_T$ at 500 K

(b) $\left[\frac{\partial C_{p,m}}{\partial p}\right]_T$ at 590 K

Figure 6.2: Comparing $\left[\frac{\partial C_{p,m}}{\partial p}\right]_T$ for 500 K and 590 K, indicating the origin for the deviations shown in Fig. 6.1a

The origin of the oscillations in the c_p vs p plane is related to the interpolation of the experimental speed of sound data for the intermediate isotherms required for integration. This is mentioned by Estrada-Alexanders [16] and the effect can be reduced by applying a filter, or as observed during this research by altering the interpolation method. It should be noted that the oscillations are a non-physical effect and the origin of the oscillations has not been identified. Furthermore, an alternative numerical method using boundary conditions instead of the initial values used in this research is brought up by Estrada-Alexanders [16].

The difference in strength of the oscillations shown in Figs. 6.2a and 6.2b is related to the explanation given in Chap. 4 regarding the curvature of the isotherms. It was observed that the curvature of isotherms in the c vs p plane, decreases with increasing temperatures. The stronger curvature at lower temperatures is translated to stronger oscillations shown in Fig. 6.2, because the oscillations are related to the speed of sound data.

The integration procedure is required to start at the lowest measured isotherm. This results in the induced oscillation at the initial isotherm being propagated through the integration steps taken. If this initial oscillation is stronger due to starting at a lower temperature, the error caused by this oscillation is propagated with the integration. This is observed in Fig. 6.1a, where the deviations are larger than the deviations observed in

Fig. 6.1b. Furthermore, Fig. 6.3 shows the effect of the propagation of the starting oscillation at the final temperature of the pressure range, at T = 670 K. In this figure the values for $\left[\frac{\partial c_p}{\partial p}\right]_T$ are shown, determined from the two different starting temperatures. For each of the starting conditions two lines are present, one line represents the differentiation using second order finite differences. The other line represents the fitting of $\left[\frac{\partial c_p}{\partial p}\right]_T$, which is used in the program to remove the unstable response. It is seen that the integration procedure starting at 500 K shows highly oscillating results of the finite difference of the values of c_p, compared to the fitted curve running through the its centre. For the results determined using the starting temperature of 590 K, both lines overlap. The purple line indicating the unfitted result still shows oscillations, but they are marginal compared to the results of the 500 k starting temperature.

The difference in oscillations, as shown in Fig. 6.3, shows the effect of changing the starting temperature of the method, where an oscillating slope of c_p is an unrealistic result. Furthermore, it is observed that the absolute values differ as well, indicating that the starting temperature affects the slope of the c_p curve. Because the results of the higher starting temperature show fewer oscillations, it can be concluded that the developed method is more accurate when used for analysing higher temperatures.

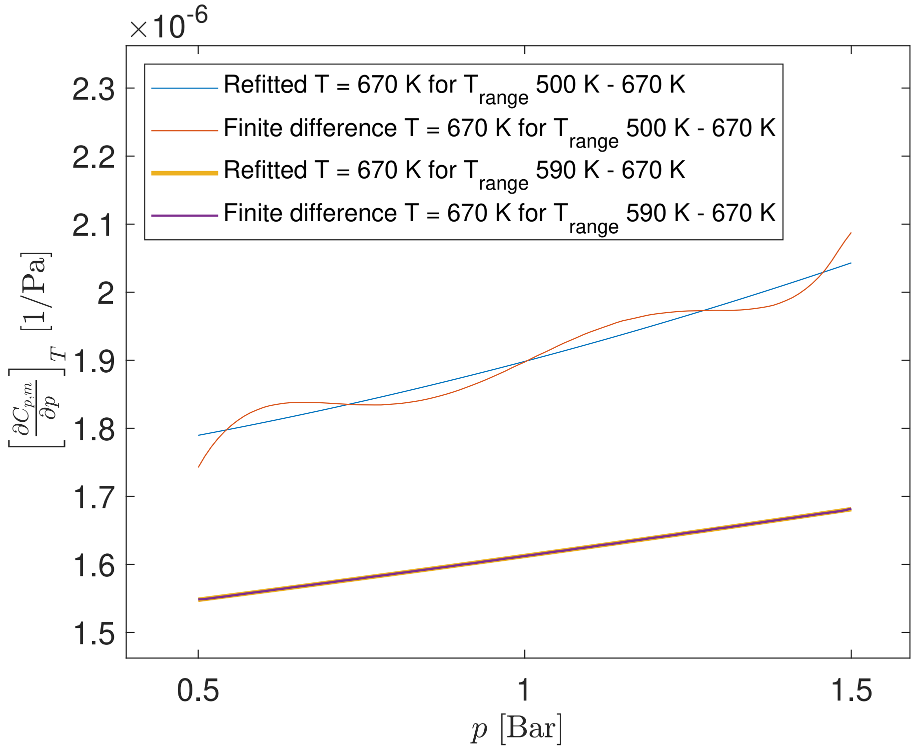

Figure 6.3: $\left[\frac{\partial c_p}{\partial p}\right]_T$ at 670 K. This figure indicates the difference in slope of $C_{p,m}$ vs p for the same temperature, but using a different starting temperature. These large oscillations originating from the temperature range of 500 K - 670 K, indicate the reduced accuracy of the alternative method when starting at low subcritical temperatures.

6.2. Analysis of the ideal gas heat capacity for D4 obtained using the numerical method

In the previous section the adaptations to the integration program for D4 were discussed, together with observations made when altering the starting temperature. In this section, the results of the comparison between the ideal gas heat capacity obtained using the alternative method and conventional method are shown. The data used for this analysis is obtained using RefProp for the temperature range of 500 to 600 K. For the alternative method a pressure range of 0.5 to 1.5 bar. For the conventional method a pressure range of $1 \cdot 10^{-5}$ to 1.5 bar is used, in order to get a good solution for the conventional method. The rationale behind this is further elaborated in Subsec. 6.3.3. Similar to Sec. 5.4 the results for c_p^{IG} will be discussed in combination with the results for Z and c_p, in order to show the validity of the results.

6.2.1. Numerical method vs conventional method

In this subsection the alternative method and the conventional method are compared. From Fig. 6.4 it is seen that the values for the c_p^{IG} closely match the results obtained using the conventional method. It can be observed that the conventional method is a straight line, while the results of numerical integration follow a more curved line, especially at lower temperatures. This is connected to the explanation regarding the increased curvature at of the isotherms at lower temperatures in the c vs p plane. This increased curvature results in slight deviations, due to increased fitting errors.

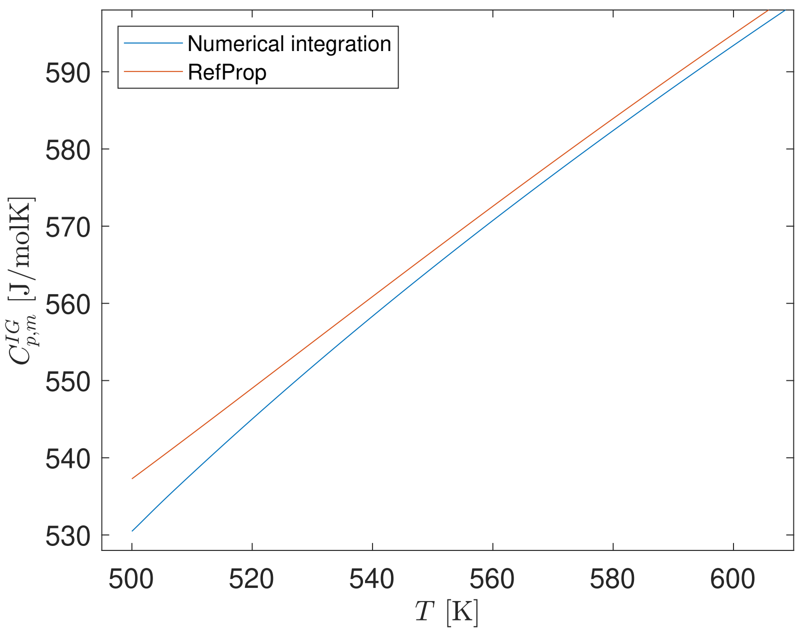

Figure 6.4: Comparison between the conventional method and alternative method for D4 for the temperature range of 500-600 K

In Fig. 6.5 the values for Z and c_p are shown, obtained by the alternative method. Similar to methane, the values for the compressibility factor and the model data are similar and perfectly overlap each other, indicating no large deviations caused by the integration, shown in Fig. 6.5a. However, slight deviations are found for the values of c_p, between the model and numerically integrated results, shown in Fig. 6.5b. This is related to the starting temperature of 500 K, as was discussed in Subsec. 6.1.4.

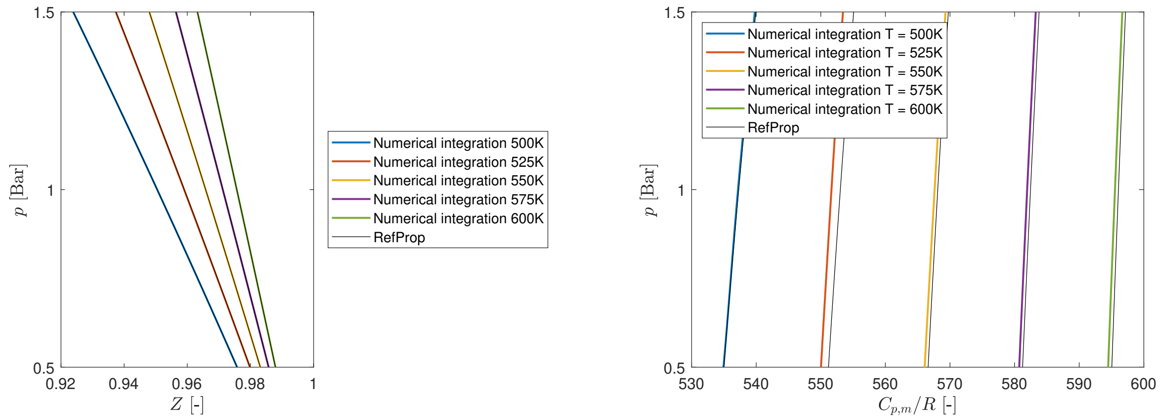

(a) Z vs p

(b) $C_{p,m}$ vs p

Figure 6.5: Comparison between the model data and the values obtained by numerical integration. Similar to Figs. 5.10 and 5.11

6.3. Sensitivity analysis of the numerical method and the conventional method

The development of the alternative method originated from the large sensitivity towards a fluctuation in ideal gas speed of sound of the conventional method, as explained in Chap. 4. The alternative method was developed with the aim of finding a method less sensitive to fluctuations in speed of sound. The main research question for this section of the thesis asks whether the alternatively developed method is less sensitive towards changes in speed of sound. Especially with regards to the determination of the ideal gas isobaric heat capacity. In order to answer this research question a sensitivity analysis is performed on both the conventional and alternative approaches. This section addresses the methodology and results of the sensitivity analysis carried out on the alternative method for D4.

6.3.1. Methodology of the sensitivity analysis

The sensitivity analysis is carried out in a such a manner that the inputs are equal for both methods analysed. The input values required for both methods originate from the same conditions and are sufficient to solve for c_p^{IG}. For the conventional method only the speed of sound data is required, while for the alternative method values for Z are also required to initialize the integration procedure. All of these data points are obtained from the thermodynamic model RefProp. In order for the alternative method to work as designed, five homogeneously spaced isotherms ranging from 500 K to 600 K are used. The error introduced is based on a thousand normally distributed points with an error of 0.3%, similar to the measurement uncertainty of the OVAR. This random error was applied to the speed of sound data obtained from the model RefProp. The ideal gas isobaric heat capacity was then determined for each method, described in Chaps. 4 and 5 accordingly.

The analysis for the conventional method follows the process outlined in Chap. 4. The randomised ideal gas speed of sound data is fitted to a second order polynomial, per isotherm. This results in a thousand different values for the ideal gas speed of sound per isotherm. These randomised ideal gas sound speeds are then applied in Eq. 4.8, to obtain a thousand randomised values for the ideal gas isobaric heat capacity per isotherm.

In Chap. 4, it was seen that for D4 an asymptote arises for the conditions close to the conditions of the experiment. This asymptote is governed by the term $\frac{(c^{IG})^2 M}{RT}$. When this term is equal to one, the denominator of Eq. 4.8 is equal to zero. For the sensitivity analysis, the ideal gas speed of sound is the only variable for each of the isotherms analysed. Certain points are affected by this asymptote for the used random distribution. This produced unrealistic and highly negative values for the ideal gas isobaric heat capacity. The removal of these outliers is required before the mean and standard deviation can be determined for the ideal gas isobaric heat capacity.

As explained in Chap. 5 the alternative method requires a set of five isotherms to accurately determine the speed of sound data for all of the intermediate isotherms used during the integration process. The randomised speed of sound data is therefore bundled together in sets of five to solve the integration process. For the sensitivity analysis of the alternative method, a temperature step size of 0.1 K and a pressure step size of 0.01 bar are used. A thousand different values for c_p^{IG} are obtained for each isotherm following this process. An unstable response is observed for eleven of the randomised runs. These outlying results are removed for further analysis, so that the mean and standard deviation of the c_p^{IG} data can be determined.

6.3.2. Results of the sensitivity analysis

Figure 6.6 shows the results of the sensitivity analysis before the removal of the outlier data points. In the figure, $C_{p,m}^{IG}$ is plotted versus c^{IG}. Even though the ideal gas speed of sound is not used for determining $C_{p,m}^{IG}$ using the alternative method, it is used in the figure to provide a direct comparison with the results of the conventional method. The coloured dots indicate the individual results obtained using the alternative method. The black dots indicate the results obtained using the conventional method. It should be noted that the Y-axis of the figure ranges from $-8 \cdot 10^5$ to $4 \cdot 10^5$ compared to 200-1400, in Fig. 6.7, caused by the removal of the outliers. From both figures it can be observed that the results from the alternative method follow the same curvature as the results obtained using the conventional method. Furthermore, it is seen that the alternative method follows the same asymptotic behaviour that appeared for the conventional method.

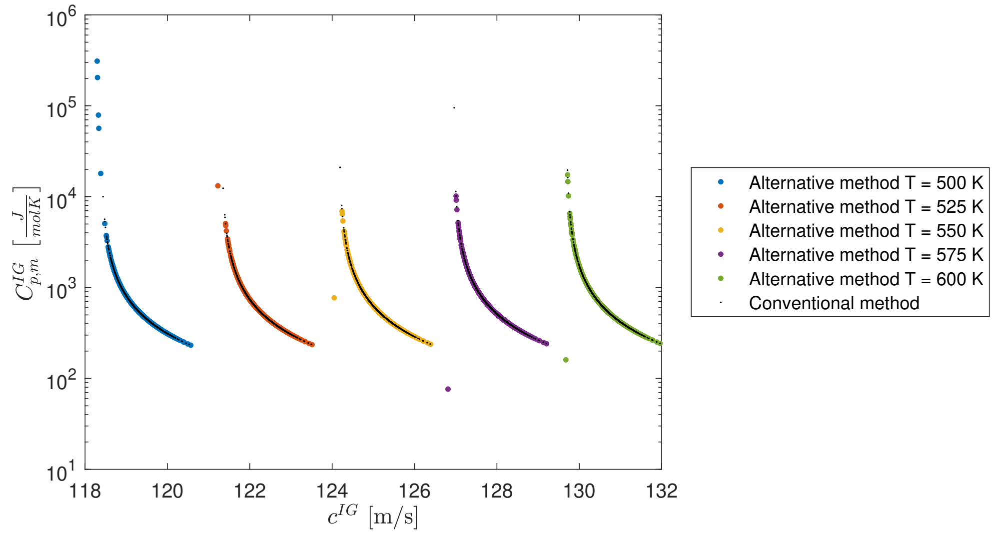

Figure 6.6: $C_{p,m}^{IG}$ vs c^{IG} for the conventional and alternative method for the full set of data points, including outliers. Expressing the results of the alternative method as if they are directly related to the ideal gas speed of sound, in order to determine whether the asymptotic behaviour is also present in the alternative method.

Figures 6.7 and 6.8 are obtained after removal of the outliers. Fig. 6.8 shows $\left(\frac{\partial C_{p,m}^{IG}}{\partial c^{IG}}\right)_T$, this shows the sensitivity of both methods is dependent on the ideal gas speed of sound. From both figures it is concluded that the sensitivity towards a change in speed of sound for both methods is similar. This is due to the fact that the spread of the data points for both methods is similar. This indicates that the response of both methods towards the randomised speed of sound input, results into a similar output. This is especially true for the higher temperature results of the alternative method, for which results of both methods overlap each other entirely. This is less the case for the isotherm at T = 500 K, where the spread of the results of the conventional method is only slightly larger than the alternative method. This is could be caused by the fact that for the alternative method no integration has been performed yet at this isotherm. Therefore, no induced errors caused by the integration of the randomized data set are yet visible, which are introduced to these randomized points at higher temperatures.

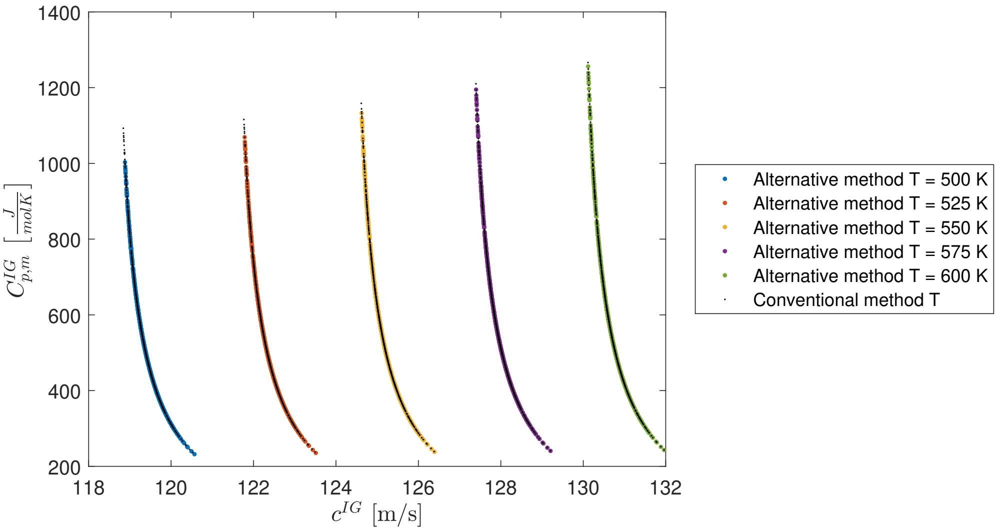

Figure 6.7: $C_{p,m}^{IG}$ vs c^{IG} for the conventional and alternative method after having removed the outliers. Expressing the results of the alternative method as a function of the ideal gas speed of sound, reveals that the methods have a similar sensitivity to altering the speed of sound, due to the similar range of datapoints.

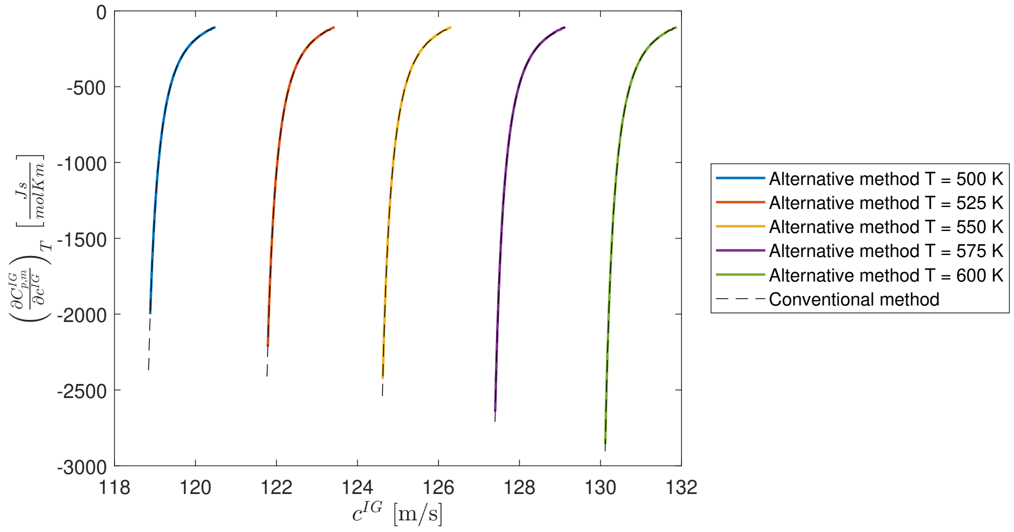

Figure 6.8: $\left(\frac{\partial C_{p,m}^{IG}}{\partial c^{IG}}\right)_T$ vs c^{IG}, indicating the sensitivity of both methods with respect to a change in ideal gas speed of sound.

The effects of this discussion are also observed in Fig. 6.9. The figure shows the mean and the upper and lower bounds for both methods. It can be observed that the bounds for the alternative method are smaller at lower temperatures compared to the conventional method, but these bounds increase with increasing temperature. At 600 K, the lines of the alternative and conventional method showing the mean and upper bound have converged, while for the lower bound this happens at around 530K. This shows that the alternative method is slightly less sensitive to a change in speed of sound at lower pressures, but due to the convergence this is valid only for a limited region. This indicates that the alternative method is not significantly less sensitive to a fluctuation in the speed of sound.

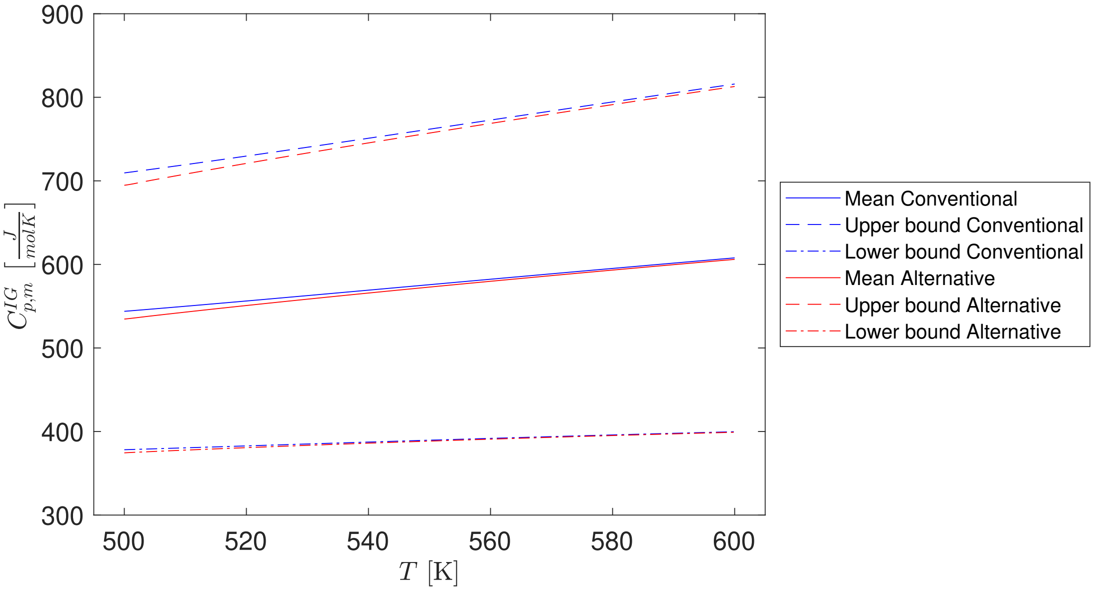

Figure 6.9: $C_{p,m}^{IG}$ vs T, for the sensitivity analysis of the conventional and alternative method. Including the upper and lower bound determined as one standard deviation from the mean.

Earlier this section, it was speculated that the number of integration steps could be the reason for the convergence of the alternative and conventional method at higher temperatures. Therefore, two additional runs are analysed in order to investigate the effect of the number of integration steps has on the sensitivity. The first extra run used an increased temperature step size, dT = 1 K, compared to dT = 0.1 K used thus far. The second extra run featured the same step size of dT = 0.1 K, but starting at 550 K. From the figure it can be deduced that the same trend is followed for the results of the extra runs, indicating that the convergence at higher temperatures towards the results of the conventional method is not caused by the error induced per iteration. The real cause of this convergence could be linked to the oscillating behaviour shown in Sec. 6.1, because of the link between the oscillations and the speed of sound data. Therefore, certain random data points can amplify the effect of these oscillations.

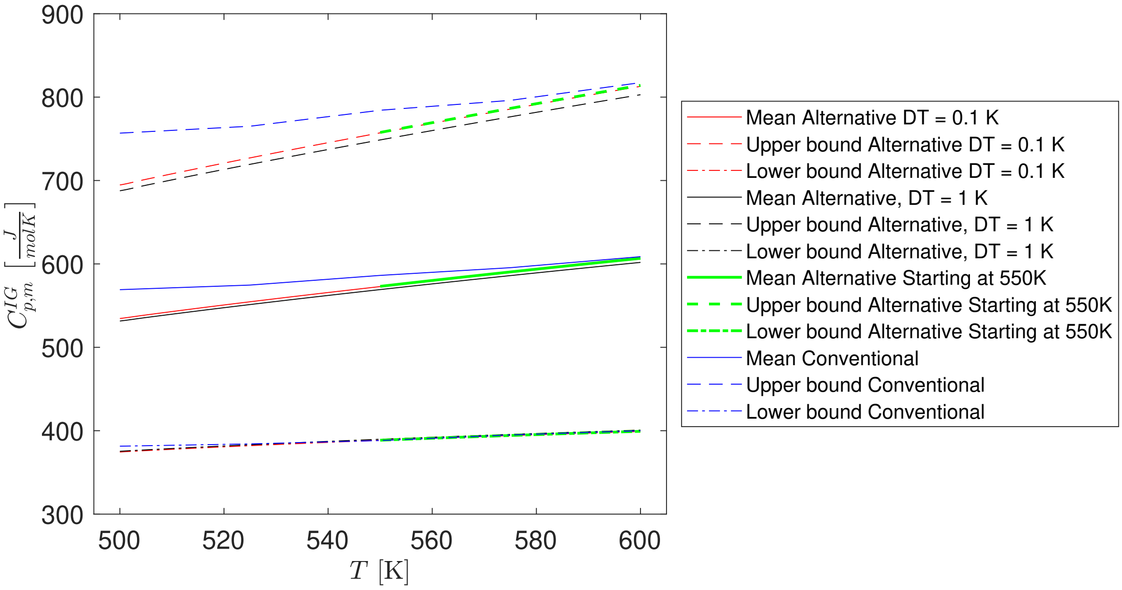

Figure 6.10: $C_{p,m}^{IG}$ vs T, for the conventional and alternative method with two additional results obtained using the alternative method, to determine the effects of changing the starting temperature and the step size on the sensitivity analysis.

Because of the similar sensitivity and the converging of the bounds, it is concluded that the alternative method does not provide a significant improvement over the conventional method. Furthermore, the alternative method provides a more complex method with higher computational cost compared to the conventional method, which does not result in a significant reduction in sensitivity to a fluctuation in the speed of sound.

6.3.3. Altered pressure range for the conventional method

The pressure and temperature conditions used in the sensitivity analysis were chosen to represent an actual experiment as accurately as possible. Besides the convergence shown in Figs. 6.9 and 6.10 at upper temperatures, divergence between the results of the two methods is shown at the lower temperature end. This divergence is caused by a change in the slope of the results obtained using the conventional method. The difference in slope at lower temperatures is caused by the lower pressure limit of the used pressure range, 0.5 bar. Lowering this lower pressure limit to $1 \cdot 10^{-5}$ bar results in the removal of this sudden change in the slope, shown in fig. 6.11.

For the pressure range of 0.5-1.5 bar this sudden change in slope is caused by the fitting of the data. When fitting the speed of sound and pressure data, the resulting curve tries to emulate the provided data set for the specified pressure range. However, fitting errors are always introduced. The fitted result used to extrapolate data can therefore induce errors or unrealistic behaviour. This procedure is required for obtaining c_p^{IG} at the ideal gas limit, $p \rightarrow 0$. The fitting error increases when the curvature of the line increases. From the analysis in Chap 4 it follows that the curvature of the isotherms increases at lower temperatures, which is also shown in Fig. 6.12. The combination of the larger fitting error and the known sensitivity of the alternative method results in errors for c_p^{IG}, leading to the observed change in curvature.

As mentioned, this effect is removed by changing the lower pressure limit to $1 \cdot 10^{-5}$ bar. This leads to a more accurate fit of the lower pressure part, resulting in a more accurate extrapolation to the ideal gas limit. This causes the ideal gas speed of sound to be more accurately obtained, because the errors induced during extrapolation are significantly limited. However, in reality it is not possible to measure at pressures of $1 \cdot 10^{-5}$ bar, because at very low pressures resonance measurements are not possible due to the increasing noise-to-pressure ratio that comes with decreasing pressure. In Fig. 6.4 this lower pressure limit of $1 \cdot 10^{-5}$ bar is also used for the solution of RefProp.

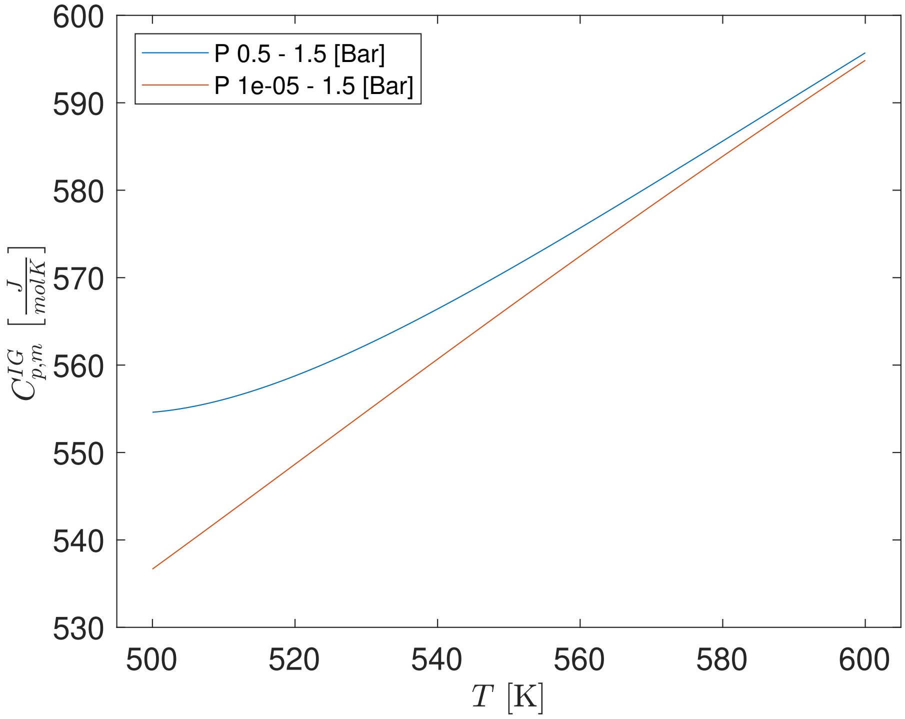

Figure 6.11: $C_{p,m}^{IG}$ vs T, obtained using the conventional method for different pressure ranges, indicating the error for the 0.5-1.5 bar pressure range due to extrapolation

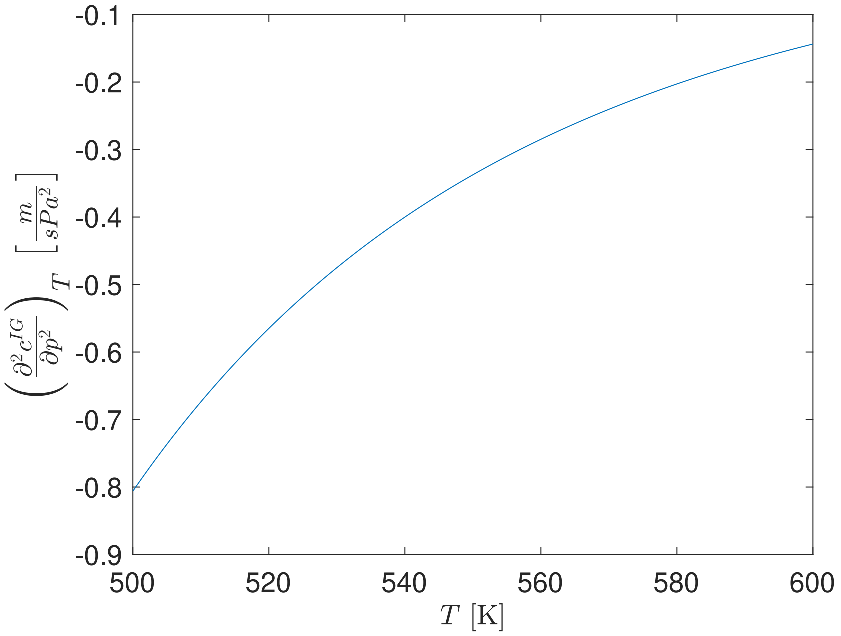

Figure 6.12: $\left[\frac{\partial^2 c}{\partial p^2}\right]_T$ vs T, showing how the curvature of speed of sound vs pressure isotherms decrease with increasing temperature.

6.3.4. Asymptotic behaviour for the alternative method

Looking at Fig. 6.6, the asymptotic behaviour is also observed for the solution obtained for the alternative method. It should be noted that in Fig. 6.6 the results of c_p^{IG} using the alternative method are plotted against c^{IG}, only for comparative reasons. The results of the alternative method for c_p^{IG} are not directly related to c^{IG}, as is the case for the conventional method. For the conventional method it was observed that this asymptote is inherent to the method, due to the presence of the ideal gas speed of sound in the denominator of Eq. 4.8. Because the alternative method is based on numerical integration it is *prima facie* less clear why the asymptotic behaviour occurs. Furthermore, it is seen in the figure that only the initial isotherm, at T = 500K, shows a clear asymptote, while the rest of the results at higher temperatures are affected by the truncation error due to integration.

The points in Fig. 6.6 showing the unstable behaviour stem from the runs shown in Fig. 6.13. From Fig. 6.13 it is observed that these runs are highly unstable. The errors introduced due to this highly unstable behaviour are propagated with the steps taken during integration, leading to the randomly placed outliers at the higher temperatures in Fig. 6.6.

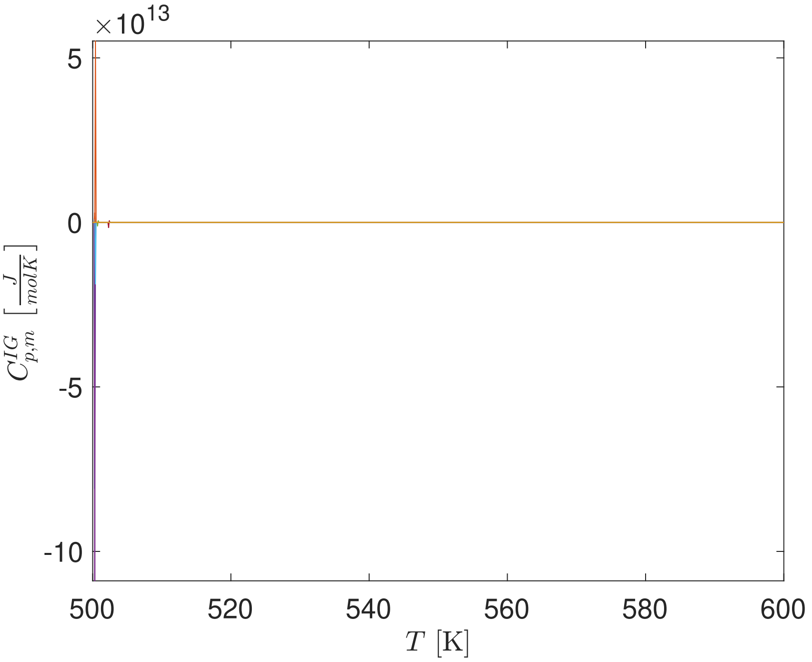

Figure 6.13: $C_{p,m}^{IG}$ vs T, obtained using the alternative method for all randomised speed of sound inputs. This figure highlights the non-physical result obtained by the outlier cases leading to the asymptote shown in Fig. 6.14

The asymptotic behaviour is only clearly shown for the initial isotherm at T = 500 K, thus the analysis on the origin of the asymptote for the alternative method is focused on this isotherm. In Fig. 6.14, the first isotherm of Fig. 6.6 is emphasised. In the figure all data points are observed, the results of the unstable isotherms of Fig. 6.13 are given in red. These unstable isotherms stem from the randomised speed of sound data and are shown in Fig. 6.15.

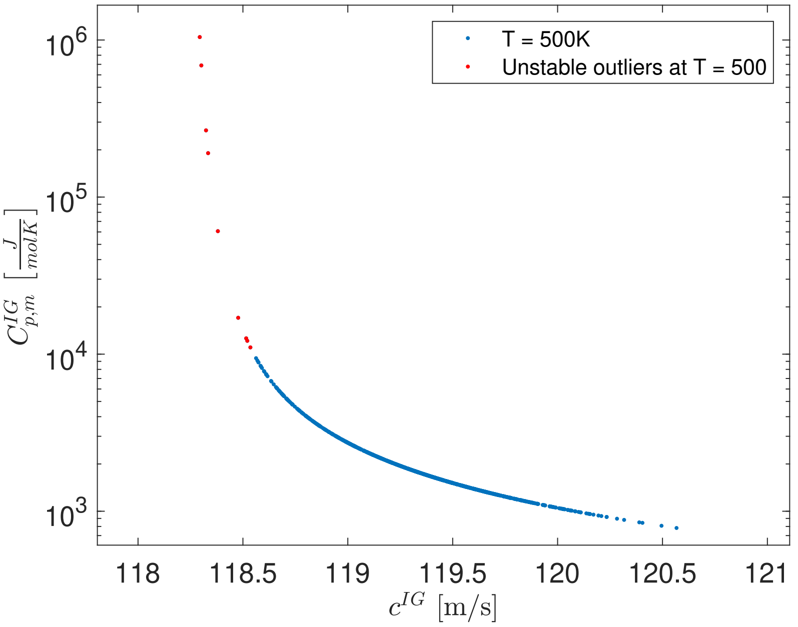

Figure 6.14: $C_{p,m}^{IG}$ vs c^{IG} at T = 500K obtained using the alternative method. The red dots indicate the results obtained from the unstable runs, shown in Fig. 6.13

From Fig. 6.15, it can be observed that the speed of sound data is separated from the mean by more than two times the standard deviation, meaning that these points in experimental measurements with the OVAR are highly unlikely to occur. Besides this, no unstable or unexpected trends are displayed, as the isotherms shown follow a similar trend to the mean.

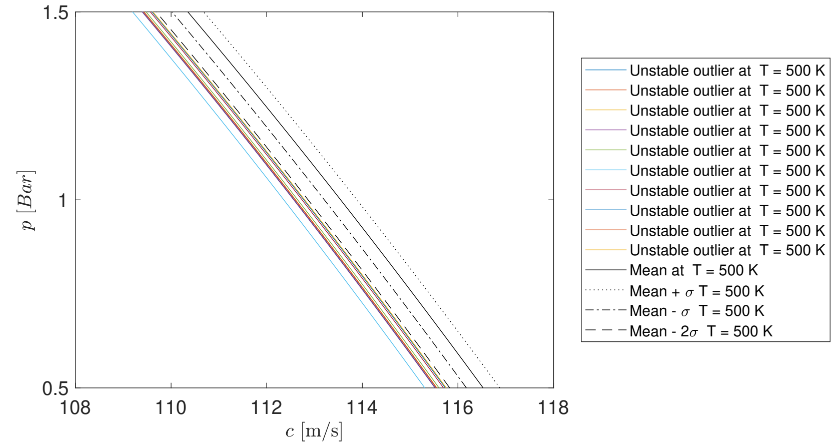

Figure 6.15: c vs p, showing the outlier isotherms, indicated by the solid coloured lines, versus the mean and the standard deviations. 2 σ is only included on the left-hand side of the mean, due to all of the outliers being present at that side of the mean.

These outliers result in unrealistic behaviour in the $C_{p,m}$ vs p plane, compared to the expected result, shown in Fig. 6.16. From the figure two observations can be made. The first observation is rightwards displacement of the unstable outliers compared to the mean value of $C_{p,m}$ at 500K. The second observation is the difference in trend and the magnitude for the outlier data. The increasingly diverging trend from the mean solution with decreasing pressure towards the right-hand side of the figure, indicates why the abnormally large values for the ideal gas heat capacity are obtained for the data shown in Fig. 6.14, when the data is extrapolated to $p = 0$ bar. This unrealistic behaviour shown in Fig. 6.14 and the fact that these results are obtained from outlier data, shown in Fig. 6.15, indicates that these results should be omitted from further analysis.

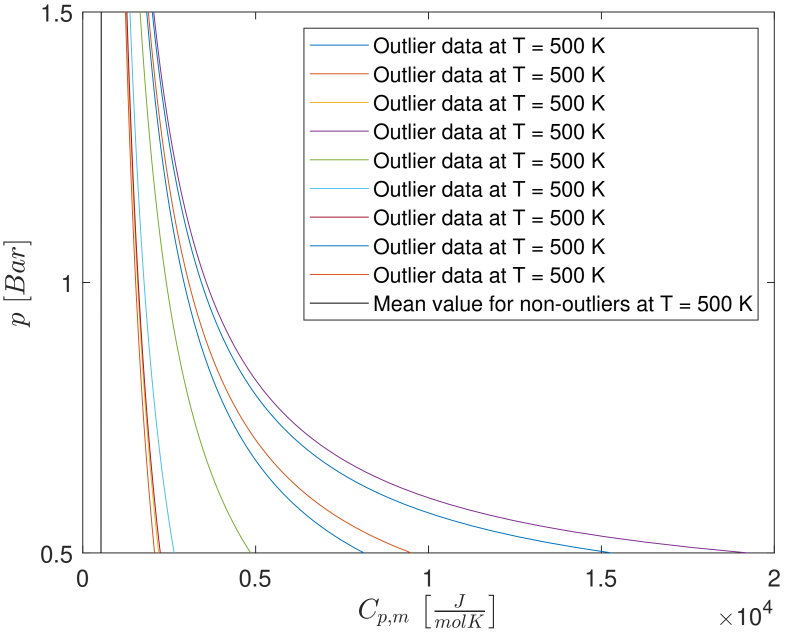

Figure 6.16: $C_{p,m}$ vs p, for the outliers. The vertical solid black line indicates how the mean value for $C_{p,m}$ should behave. The outlier data show large deviation from the mean, increasing with decreasing pressure.

6.4. Further reflection on the experiment

During the sensitivity analysis it was observed that the results for both methods are equally sensitive to a fluctuation in the speed of sound data. It was shown in Fig. 6.6, that both methods follow the same asymptotic behaviour, when the ideal gas isobaric heat capacity is plotted versus the ideal gas speed of sound.

For the alternative method, it was shown that the asymptotic behaviour originates from highly unstable results caused by outliers in the data set. For the conventional method this asymptotic behaviour stems from the denominator of Eq. 4.8 and is purely a numerical effect. This indicates that Eq. 4.8 has a validity boundary. If this boundary is exceeded, calculations using this method produce non-physical results. This is problematic with regard to the experiment analysed in Chap. 4, because with the uncertainty of the OVAR this limit is exceeded.

However, it should be noted that this is dependent on the fluid that is being analysed. Figure. 6.17 shows the asymptote for methane. The red boxes in the figure indicate the spread of the ideal gas speed of sound obtained with a 0.3% uncertainty, for T = 275 K. From the figure it follows that the margin between the asymptote and the spread of the results is significantly large, so that it doesn't cause any interference on the results. This shows that with moderately accurate equipment the ideal gas isobaric heat capacity can be determined, without suffering from non-physical effects induced by Eq. 4.8.

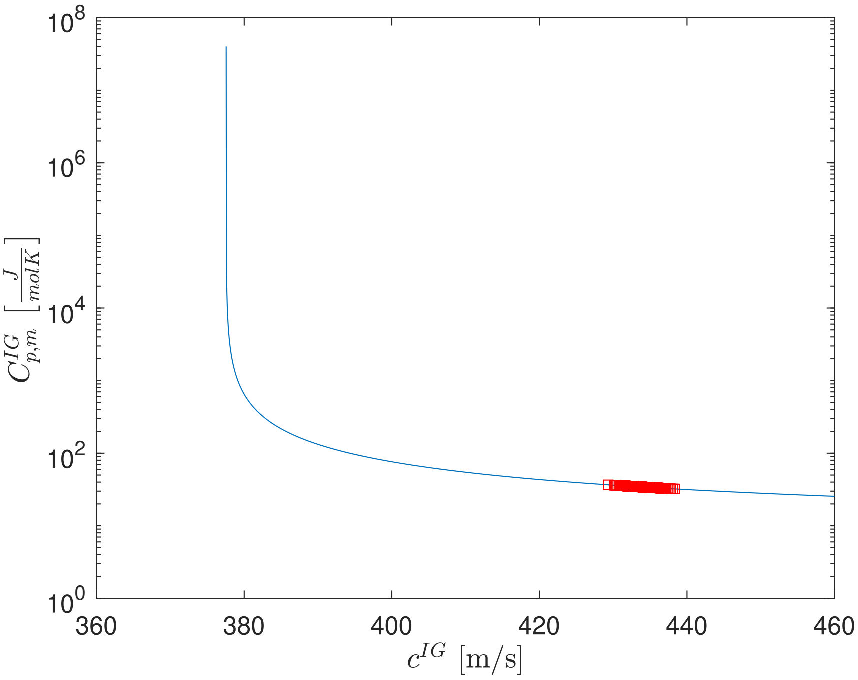

Figure 6.17: $C_{p,m}^{IG}$ vs c^{IG}, the asymptote for methane obtained using the conventional method. The red squares show the data range as if similar sensitivity analysis was conducted for methane as for D4. These points were determined using an experimental uncertainty of 0.3% for speed of sound values obtained using RefProp at 275 K and a pressure range of 1-10 MPa.

Figure 6.17, only indicates the margin at 275 K, however it is relevant to identify how this margin behaves with respect to increasing temperatures. This is shown in Fig. 6.18, where the asymptotic and average measured ideal gas speeds of sound are plotted for D4 and CH4 in 6.18a and 6.18b, respectively. The ideal gas speed of sound values for the asymptote are determined by

$$u_{\text{asy}} = \sqrt{\frac{RT}{M}}. \tag{6.1}$$

Comparing Figs. 6.18a and 6.18b, it can be seen that the margin between the average ideal gas speed of sound and the asymptotic speed of sound is much smaller for D4 than for CH4. For the temperature range shown for D4 this difference is 0.9251 m/s on average, compared to a 56.2638 m/s difference for CH4. Therefore, the results of D4 are affected by this asymptotic behaviour more significantly than the results for methane. This means that highly accurate equipment is required in order to accurately determine the ideal gas isobaric heat capacity.

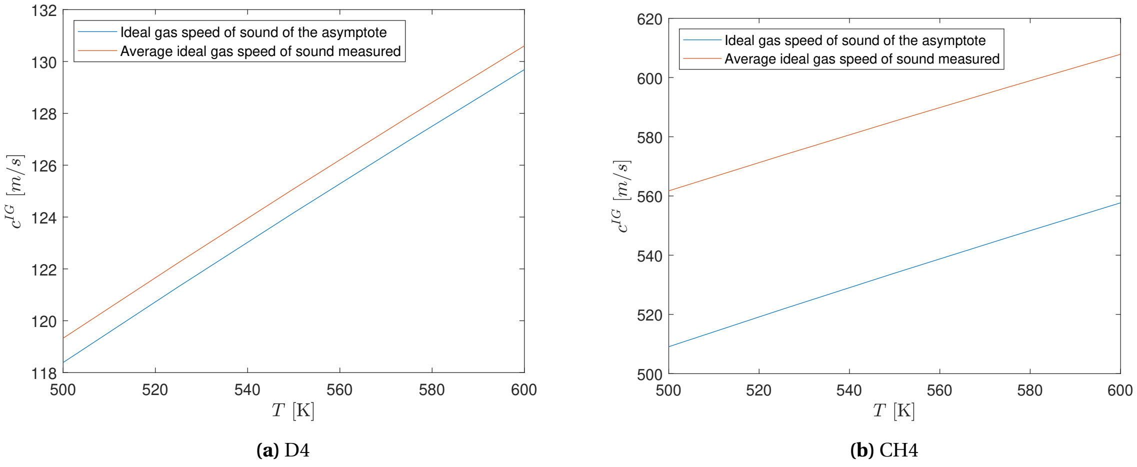

(a) D4 **(b)** CH4

Figure 6.18: c^{IG} vs T, showing the margin between the average obtained ideal gas speed of sound and the asymptotic speed of sound.

Reflecting this analysis on the earlier provided analysis of the experimental results in Chap. 4, explains why the quadratic fitting of the experimental data did not provide correct results. The combination of the accuracy of the OVAR and the limited margin between the asymptote and the average measured ideal gas speed of sound for D4, causes the experimental results to fall within this region where the asymptote is formed. This results in a highly sensitive response to c_p^{IG}, indicated by the large uncertainty bounds in the figures of Chap. 4. Furthermore, as was shown in Subsec. 6.3.3, the pressure range used introduces an additional error for the extrapolation to the ideal gas pressure. This is the reason why the curvature of the experimental results was predicted erroneously in Chap. 4, which was corrected by the alternative fitting method. Even though it was seen that the error due to fitting is insignificant when expressed in ideal gas speed of sound, this error becomes significant due to the asymptotic behaviour of Eq. 4.8 . It should be noted that this is only valid for D4, as it was seen in Fig. 6.18b, that the boundary between the averaged measured ideal gas speed of sound and asymptotic speed of sound is much larger for methane than for D4. This means that the problems observed with D4 are not a problem for methane, so the OVAR is accurate enough to be used for speed of sound measurements of CH4, but not for D4.

6.5. Summary

This chapter showed the adaptations made to the program developed in Chap 5 to accommodate for D4. This required changing the pressure step size, the temperature range and introduced fitting for $\left(\frac{\partial c_p}{\partial p}\right)_T$ to remove the numerically induced error caused by differentiation. Furthermore, it is shown that altering the starting temperature alters the results obtained for c_p. Discrepancies are observed in Fig. 6.1 between the numerically obtained values and the model values for the results obtained at the starting temperature of 500 K. These discrepancies do not exist for the run starting at 590 K. This reveals that the developed method performs better for higher temperatures. The discrepancies are caused by oscillations induced through Eq. 5.10, which reduce with starting temperature as shown in Fig. 6.2. These oscillations are connected to the interpolation method of the speed of sound data, required to construct a square integration domain.

A comparison between the conventional and alternative method based on input data obtained from RefProp revealed that both methods produce similar results for c_p^{IG}. The sensitivity analysis had a similar outcome for both methods. Therefore, it was concluded that the newly developed alternative method does not reduce the sensitivity towards a change in speed of sound. This answers the second research question for this part of the thesis, regarding the sensitivity of the newly developed method. Even though no improvement was made regarding the sensitivity of the method compared to the conventional method, the conventional method is unable to accurately determine the ideal gas heat capacity at lower temperatures for the temperature and pressure conditions used, as is shown in Fig. 6.11. This shows that the alternative method is more capable of analysing the ideal gas heat capacity at low temperatures based on model data simulating experimental data.

The formation of the asymptote for the alternative method, shown in Fig. 6.6, was investigated. The origin of the asymptote for the conventional method is a numerical effect of varying the ideal gas speed of sound such that the denominator of Eq. 4.8 equals zero. Since the ideal gas speed of sound is not used in the alternative method, the origin for the formation of the asymptote was caused by strong outliers in the speed of sound input. These strong outliers were removed in the analysis of the results, therefore removing this strong asymptotic behaviour from the alternative method.

Even though the sensitivity analysis was conducted only using data obtained through RefProp, a reflection was made with regard to the experiment. The data of the sensitivity analysis revealed that D4 is inherently more sensitive towards a fluctuation in the sound speed. This is caused by the small margin between the average ideal gas speed of sound and the ideal gas speed of sound of the asymptote. This margin for D4 is on average around 1 m/s, which is significantly smaller compared to the average margin for CH4 of 55 m/s. The margin between the ideal gas speed of sound and the asymptotic speed of sound is shown in Fig. 6.18.

7

Conclusion and recommendations

This chapter concludes the research preformed in this thesis and brings up recommendations for future research. The conclusion is structured as follows. Section 7.1 concludes the experimental analysis and Sec. 7.2 concerns the development and analysis of the alternative method. This conclusion is finished by the recommendations for future work, provided in Sec. 7.3.

7.1. Conclusion on experimental analysis of D4

The discussion about the results of the experiment answered the research question regarding the validity of the thermodynamic models when these are used outside of the region of accurately available data used for the creation of those models. The presented analysis reveals that the models can qualitatively predict the thermodynamic conditions for the temperature range of 495 to 603 K, because no large deviations between the model and experimental data are observed. However, due to the large uncertainties of the ideal gas isobaric heat capacity data and the required use of the alternative fitting method, no claims can be made regarding the accuracy of the models. Furthermore, the alternative fitting method was required because the experimentally obtained speed of sound data could not be fitted correctly using a second order polynomial. This was observed by errors in the curvature of the fitted isotherms, which does not correspond to the correct curvature shown by Nannan and the thermodynamic models.

Though, the analysis regarding the validity of the models was performed straightforwardly, observations made regarding the sensitivity of the method during the analysis revealed an asymptote on the $C_{p,m}^{IG}$ vs c^{IG} plane, close to obtained ideal gas speed of sound from the experiment. This asymptotic behaviour is caused by the $\frac{(c^{IG})^2 M}{RT}$ term. The presented analysis studied the effects of the variation of c^{IG} on c_p^{IG}. Even though the formation of this asymptote is a non-physical effect, it does affect the results of $C_{p,m}^{IG}$ for D4 significantly, because the margin between the asymptotic ideal gas speed of sound and measured speed of sound is less than 1 m/s. This is significantly smaller compared to the same margin for methane, which is 50 m/s.

7.2. Conclusion regarding the alternative method

The limited margin between the asymptote and the measured ideal gas speed of sound and the uncertainty introduced due to fitting of the speed of sound data, led to the adaptation of an alternative method for the analysis of the speed of sound data. This new method was developed with the aim of reducing the sensitivity towards a fluctuation in the speed of sound. The method was developed from research performed by Trusler and adapted to determine the ideal gas isobaric heat capacity. The development of the alternative method showed the steps required for the method to function for methane. The additional step added to the method by Trusler regards the fitting of the c_p data, in order to obtain the ideal gas isobaric heat capacity. Adapting the method for D4, however, requires fitting of the term $\left(\frac{\partial c_p}{\partial p}\right)_T$, due to the unstable behaviour caused by numerical differentiation. The discussion addressing the development of the alternative method and the adaptations to accommodate for D4 answer the research question regarding the steps required to obtain c_p^{IG} using numerical integration.

A sensitivity analysis was performed to answer the question whether the newly developed method is less sensitive to a fluctuation to the speed of sound. From the presented analysis it is concluded that the newly developed method is equally sensitive towards the same fluctuations in the speed of sound as the conventional method. This conclusion is made through observing the same behaviour and the similarity of spread of the data points for $C^{IG}_{p,m}$ vs c^{IG}, indicating that no major improvement is made with regard to the sensitivity to a fluctuation in the speed of sound data. However, the results for the conventional method revealed that for a realistic experimental pressure range significant deviations were observed for the lower temperature regions. This discrepancy between the results of the conventional method using two different pressure ranges means that the newly developed alternative method provides a better result for a realistically measurable pressure range.

The performance of the alternative method increases with a higher starting temperature, mainly at supercritical temperatures. This is observed in the comparison between the subcritical and supercritical starting conditions of the numerical integration. It was observed that discrepancies between the numerical and model data exist on the c_p vs p plane, for the temperature range of 500 K - 670 K, while for the results obtained using a supercritical, temperature range of 590 K - 670 K, these discrepancies are reduced. These discrepancies are caused by oscillations induced through the alternative method, and are shown by the partial derivative of c_p with respect to pressure. It is observed that the oscillations subcritical starting conditions are significantly larger in amplitude and have a shorter period compared to the supercritical starting conditions. Furthermore, it is seen that these oscillations originating from the subcritical starting conditions are more persistent than the oscillations from the supercritical starting conditions. Thus, showing why the supercritical starting conditions result in less discrepancies with data from literature compared to the subcritical starting conditions.

It was shown that the sensitivity of the alternative method with respect to a fluctuation in the speed of sound did not improve significantly over the conventional method. This analysis was based on simulated experimental data obtained from the thermodynamic model RefProp. However, comparing the performance of the conventional method to the alternative method on a simulated experimental data set showed that the alternative method was better able to predict the ideal gas isobaric heat capacity. This is because the conventional method shows discrepancies for the lower temperature region, originating from the fitting of the speed of sound data. It follows from this that there is potential for the alternative method to be used in future research.

7.3. Recommendations

The research conducted showed that analysing the ideal gas isobaric heat capacity for D4 is highly sensitive to a change in the measured speed of sound for both of the methods utilised. Consequently, the uncertainty of the measured speed of sound is amplified when c_p^{IG} is determined. A general improvement for a repetition of this experiment is to use a highly accurate resonator, because of the highly sensitive behaviour inherent to D4. An estimated figure for the recommended measurement uncertainty is based on the amplification of the uncertainty of the OVAR. The uncertainty of the OVAR is 0.3% for the measured speed of sound, which is roughly multiplied by 100, when the ideal gas isobaric heat capacity is obtained. Therefore, in order to obtain an insignificant error for c_p^{IG}, <5%, it is recommended to use a resonator with a known measurement uncertainty of <0.005%. This could required the development of a new resonator, with a preference for an cylindrical resonator due to the fact that these are inherently more accurate than the box type resonator used in the experiment conducted in this research.

Because the data presented in this study is not without its flaws, it is recommended for future work to analyse the same temperature range again so that more accurate data can be obtained. This more accurate data can then be further used for the development and improvement of the thermodynamic models. This requires more measurement points per isotherm, as well as a minimum of five isotherms homogeneously spread. This provides a data set that can be used by both the conventional method and the alternative method, developed in this research. Furthermore, enough data points per measurement point should be provided, such that an accurate outlier detection can be performed. This also provides enough data to determine the uncertainty of the experiments carried out, instead of relying on known data from previous tests with the same equipment.

For the experimental results it was observed that the point measured at 603K showed a slight deviation from the trend that was followed by the subcritical points. Furthermore, the range where $\Gamma < 0$ is supercritical, thus it is recommended for future research to investigate the supercritical area in more detail. This also allows for the measurement of a larger pressure range, since saturation effects are eliminated for supercritical isotherms. The supercritical region is also the region where the alternative method performs best.

This allows for extension of the pressure range that is analysed as well, which could solve the stability problems observed during the adaptation of the alternative method to D4 regarding the pressure step size. An increased pressure range allows for a larger pressure step size, such that the $\mathrm{d}p = 0.1p_c$ recommendation by Trusler can be achieved. For methane it was shown that $\mathrm{d}p < 1$ bar resulted in an unstable response, where the recommended value for $\mathrm{d}p$ according to $\mathrm{d}p = 10\%p_c$, was ≈ 4 bar. It follows from this that the recommendation made by Trusler is close to the stability limit of $\mathrm{d}p$. Following $\mathrm{d}p = 10\%p_c$ results in $\mathrm{d}p \approx 1.3$ bar, while 0.01 bar is currently used due to the limited pressure range. Increasing the pressure range allows for a larger pressure step to be used, which could eliminate the unstable response and therefore the need for fitting of $\left(\frac{\partial c_p}{\partial p}\right)_T$.

Observations made during tests of the alternative method for methane revealed oscillations on the c_p vs p curve, which increased in magnitude at higher temperatures. These oscillations are reduced by changing the method of interpolating the speed of sound data and are removed by applying a higher order fit on the experimental speed of sound data. This is in accordance with research conducted by Estrada-Alexanders, who reported the formation of ripples at higher temperatures originating from the interpolation of the speed of sound data. Estrada-Alexanders mentions that these ripples can also be removed by introducing a filter to the program. However, it should be noted that the introduction of this filter or changing the interpolation procedure did not remove the cause of the ripples. Thus, a boundary condition method is introduced to determine the thermodynamic properties from speed of sound data. The research by Estrada-Alexanders focuses on obtaining the same thermodynamic properties as the alternative method, Z and c_p. The conclusion drawn by Estrada-Alexanders is that the boundary condition method proved to be an accurate alternative to determine thermodynamic properties in a single-phase region. Therefore, a similar procedure as developed with the introduction of the alternative method for obtaining the ideal gas heat capacity in this research could be applied to the boundary condition method developed by Estrada-Alexanders. Because the same thermodynamic properties are being used and determined in this boundary condition method, a similar fit to the c_p data could be done in order to obtain the ideal gas isobaric heat capacity. Researching this boundary condition method in a similar fashion as the initial value method in this research, could provide a method which is more accurate in determining c_p. This boundary condition method could remove the cause of the oscillations on the c_p vs p plane, which are induced by the fitting or interpolation of the speed of sound data.

A

Appendix A: Nannan Data

This Appendix feautures the data obtained by Nannan for D4 [40].

Table A.1: Experimental speed of sound data as obtained by Nannan [40]

T [K]	p [kPa]	c [m/s]	σ
450	38.90	110.351	252.0
	46.70	109.656	89.8
	57.41	108.801	72.2
	62.89	108.299	17.0
	69.33	107.727	16.4
465	31.29	113.043	638.9
	40.99	112.320	123.0
	49.18	11.723	69.2
	58.99	110.976	20.2
	70.69	110.062	16.5
	77.48	107.535	14.3
	92.89	108.286	9.9
	101.01	107.535	14.3
	111.40	106.695	5.3
	121.67	105.761	7.4
465	36.51	112.753	138.6
	47.85	111.913	37.2
	57.21	111.202	25.3
	68.51	110.332	14.4
	74.87	109.829	10.7
	81.72	109.278	26.5
	97.68	107.963	270.8
	106.95	107.179	89.7
	116.93	106.300	335.1
465	32.63	112.986	242.5
	46.84	111.935	53.3
	61.46	110.824	18.8
	73.59	109.872	15.3
	87.87	108.720	9.0
	105.11	107.277	15.0
	123.48	105.664	17.4
480	42.70	114.022	56.2
	54.67	113.202	18.1
	65.08	112.478	36.
	71.30	112.038	24.6
	85.50	111.071	24.9
	92.46	110.502	12.1
	109.21	109.241	4.5
	118.88	108.493	3.1
	129.21	107.675	6.8
	140.39	106.769	11.2
	152.36	105.769	8.6
	165.42	104.642	6.3
495	27.45	117.135	200.8
	36.20	116.658	71.6
	47.54	115.985	15.6
	143.41	109.744	283.3
	159.70	108.434	20.5
	160.40	108.391	105.0
	174.53	107.346	44.6
	186.64	106.439	78.7
	198.61	105.492	1287.4
	224.52	103.408	31.8

B

Appendix: Trusler data

This appendix features the data by Trusler used for methane [54, 55].

Table B.1: Experimental speed of sound data as obtained at T = 275 K by Trusler [54, 55]

T [K]	P [kPa]	c [m/s]
275	10.03660	416.4693
	9.28123	416.5507
	8.48529	414.4408
	7.55257	413.1386
	6.79170	412.9209
	5.99172	413.4119
	5.17575	414.5824
	4.38058	416.2865
	3.59523	418.4386
	2.78223	421.0833
	2.39056	422.4883
	1.99285	423.9925
	1.59567	425.5683
	1.20231	427.1919
	0.81522	430.7198

Table B.2: Experimental speed of sound data as obtained at T = 300 K by Trusler [54, 55]

T [K]	P [kPa]	c [m/s]
300	9.96690	444.5084
	9.23575	442.3876
	8.38280	440.5471
	7.61667	439.4563
	6.80724	438.8416
	6.00990	438.7382
	5.20812	439.0979
	4.40630	439.8821
	3.59759	441.0621
	2.79741	442.5757
	2.40724	443.4274
	2.00355	444.3816
	1.60162	445.4003
	1.20625	446.4657
	0.80836	447.5973
	0.40237	448.8030

Table B.3: Experimental speed of sound data as obtained at T = 325 K by Trusler [54, 55]

T [K]	P [kPa]	c [m/s]
325	10.00958	467.1599
	9.19295	465.0207
	8.42680	463.4061
	7.64200	462.1393
	6.79616	461.1911
	5.98937	460.6722
	5.19704	460.5084
	4.39606	460.6707
	3.62073	461.1382
	2.80071	461.8932
	2.39559	462.3782
	1.99953	462.9154
	1.60087	463.5166
	1.18571	464.2038
	0.79938	464.9891
	0.39338	465.6774

Table B.4: Experimental speed of sound data as obtained at T = 350 K by Trusler [54, 55]

T [K]	P [kPa]	c [m/s]
350	9.99178	487.2842
	9.22309	485.3390
	8.38278	483.5357
	7.59459	482.1499
	6.78365	481.0220
	6.00128	480.2127
	5.18819	479.6527
	4.39378	479.3682
	3.62073	479.3302
	2.75485	479.5542
	2.237593	479.7369
	1.99204	479.9721
	1.57626	480.2834
	1.20488	480.6084
	0.80234	481.0094
	0.40123	481.4545

Table B.5: Experimental speed of sound data as obtained at T = 375 K by Trusler [54, 55]

T [K]	P [kPa]	c [m/s]
375	10.13942	506.0105
	9.17623	503.5756
	8.40282	501.8701
	7.24325	499.7280
	6.80446	499.0455
	6.00088	497.9725
	5.20716	497.1360
	4.34932	496.4693
	3.62002	496.0944
	2.84282	495.8799
	2.43474	495.8413
	1.97507	495.8591
	1.60248	495.9161
	1.22021	496.0175
	0.79453	496.1778
	0.40305	496.3696

Table B.6: The ideal gas isobaric heat capacity data obtained by Trusler [54]

T [K]	$C_{p,m}^{IG}$ [-]
275	4.2021
300	4.3037
325	4.4258
350	4.5653
375	4.7182

C

Appendix Derivation of conventional method

This appendix shows the entire derivation of the of Eq 4.8 used for the conventional method

$$\left(\frac{c}{a_0}\right)^2 = \frac{A_0 + A_1 p + A_2 p^2 + \ldots}{a_0^2}, \tag{C.1}$$

where A_n are the coefficients to be fitted and a_0 is the mean linear expansivity coefficient. In the ideal gas limit of $p \rightarrow 0$, this results in

$$\left(c^{IG}\right)^2 = A_0, \tag{C.2}$$

where A_0 is given by:

$$A_0 = \frac{RT\gamma^{IG}}{M}, \tag{C.3}$$

and γ^{IG} is defined as

$$\gamma^{IG} = \frac{c_p^{IG}}{c_v^{IG}}. \tag{C.4}$$

Furthermore, it is known that

$$c_v^{IG} = c_p^{IG} - R. \tag{C.5}$$

Substituting Eq. C.5 into Eq. C.4 results in

$$\gamma^{IG} = \frac{c_p^{IG}}{c_p^{IG} - R}. \tag{C.6}$$

Substituting this into Eq. C.3 together with Eq. C.2 gives

$$\left(c^{IG}\right)^2 = \frac{RT}{M}\frac{c_p^{IG}}{c_p^{IG} - R}. \tag{C.7}$$

This equation needs to be rewritten, using the following steps in order to obtain Eq. 4.8

$$\frac{\left(c^{IG}\right)^2 M}{RT} = \frac{c_p^{IG}}{c_p^{IG} - R}. \tag{C.8}$$

Moving the denominator to the left-hand side gives

$$\frac{\left(c^{IG}\right)^2 M}{RT}(c_p^{IG} - R) = c_p^{IG}. \tag{C.9}$$

and eliminating the brackets on the left hand-side results in

$$\frac{\left(c^{IG}\right)^2 M}{RT}c_p^{IG} - \frac{\left(c^{IG}\right)^2 M}{T} = c_p^{IG} \tag{C.10}$$

Rearranging the terms gives

$$\left(\frac{\left(c^{IG}\right)^2 M}{RT} - 1\right) c_p^{IG} = \frac{\left(c^{IG}\right)^2 M}{T}. \tag{C.11}$$

Finally, this results in the corresponding relation given by Eq. 4.8

$$c_p^{IG} = \frac{\left(c^{IG}\right)^2 M}{T\left[\frac{\left(c^{IG}\right)^2 M}{RT} - 1\right]}. \tag{C.12}$$

Therefore, demonstrating that the ideal gas isobaric heat capacity can be obtained from a polynomial fit of the speed of sound data.

D

Appendix Derivation of alternative method

In order to gain better understanding of Equations 5.1 and 5.2, the derivation of these formulas is required. Starting with the Eq. 5.1, for which the derivation starts from the definition of the speed of sound given by[45, 55]:

$$c^2 \equiv \left(\frac{\partial p}{\partial \rho}\right)_s . \tag{D.1}$$

It is known that [7]

$$\left(\frac{\partial p}{\partial \rho}\right)_s = \frac{c_p}{c_v}\left(\frac{\partial p}{\partial \rho}\right)_T . \tag{D.2}$$

Combining the previous two equations results in:

$$c^2 = \frac{c_p}{c_v}\left(\frac{\partial p}{\partial \rho}\right)_T . \tag{D.3}$$

The isobaric and isochoric heat capacities are related to each other by[38]:

$$c_p - c_v = -T\left(\frac{\partial v}{\partial T}\right)_p^2 \left(\frac{\partial p}{\partial .v}\right)_T . \tag{D.4}$$

Rewriting this equation in terms of density instead of specific volume results in the following relation

$$c_p - c_v = \frac{T}{\rho^2}\left(\frac{\partial \rho}{\partial T}\right)_p^2 \left(\frac{\partial p}{\partial \rho}\right)_T . \tag{D.5}$$

Reordering the terms of this equation gives:

$$c_v = c_p - \frac{T}{\rho^2}\left(\frac{\partial \rho}{\partial T}\right)_p^2 \left(\frac{\partial p}{\partial \rho}\right)_T . \tag{D.6}$$

insert Eq. D.6 into Eq. D.3

$$c^2 = \frac{c_p \left(\frac{\partial p}{\partial \rho}\right)_T}{c_p - \frac{T}{\rho^2}\left(\frac{\partial p}{\partial \rho}\right)_T \frac{T}{\rho^2}\left(\frac{\partial \rho}{\partial T}\right)_p^2} . \tag{D.7}$$

Rewriting the right-hand side of this equation results in:

$$c^2 = \left[\frac{c_p - \frac{T}{\rho^2}\left(\frac{\partial p}{\partial \rho}\right)_T \left(\frac{\partial \rho}{\partial T}\right)_p^2}{c_p \left(\frac{\partial p}{\partial \rho}\right)_T}\right]^{-1} . \tag{D.8}$$

Further eliminating the fraction on the right-hand side results in the relation given by:

$$c^2 = \left[\left(\frac{\partial \rho}{\partial p}\right)_T - \frac{T}{\rho^2 c_p}\left(\frac{\partial p}{\partial \rho}\right)_T^2 \left(\frac{\partial \rho}{\partial T}\right)_p^2\right]^{-1} . \tag{D.9}$$

Following the chain rule, the following identity may be used

$$\left(\frac{\partial p}{\partial \rho}\right)_T \left(\frac{\partial \rho}{\partial T}\right)_T \left(\frac{\partial T}{\partial p}\right)_\rho = -1. \tag{D.10}$$

Isolating $\left(\frac{\partial \rho}{\partial T}\right)_T$ results in:

$$\left(\frac{\partial \rho}{\partial T}\right)_T = -\left(\frac{\partial \rho}{\partial p}\right)_T \left(\frac{\partial p}{\partial T}\right)_\rho. \tag{D.11}$$

Squaring the identity following the chain rule given by Eq. D.11 results in:

$$\left(\frac{\partial \rho}{\partial T}\right)_T^2 = \left(\frac{\partial \rho}{\partial p}\right)_T^2 \left(\frac{\partial p}{\partial T}\right)_\rho^2. \tag{D.12}$$

Equation D.12 is then substituted into Eq. D.9, resulting in:

$$c^2 = \left[\left(\frac{\partial \rho}{\partial p}\right)_T - \frac{T}{\rho^2 c_p}\left(\frac{\partial \rho}{\partial T}\right)_T^2\right]^{-1}. \tag{D.13}$$

It is favourable to replace the density in Eq. D.13 with the compressibility factor given by:

$$Z = \frac{Mp}{\rho R T}. \tag{D.14}$$

The compressibility factor is used over the density, because it varies less to the state inputs compared to the density [55]. Rewriting Eq. D.14, such that ρ becomes a function of Z. This is done to express $\left(\frac{\partial \rho}{\partial p}\right)_T$ and $\left(\frac{\partial \rho}{\partial T}\right)_p$ in terms of Z.

$$\rho = \frac{Mp}{ZRT}. \tag{D.15}$$

Deriving $\left(\frac{\partial \rho}{\partial p}\right)_T$ is simply done using the quotient rule, yielding the following relation

$$\left(\frac{\partial \rho}{\partial p}\right)_T = \frac{M}{RTZ^2}\left(Z - p\left(\frac{\partial Z}{\partial p}\right)_T\right). \tag{D.16}$$

Deriving $\left(\frac{\partial \rho}{\partial T}\right)_p$ is a more complex procedure and requires the following identity to be used:

$$\frac{d}{dx}\left(\frac{1}{xy(x)}\right) = -\frac{1}{x^2 y(x)} - \frac{\frac{\partial y(x)}{\partial x}}{xy(x)^2}. \tag{D.17}$$

Applying the identity for $\left(\frac{\partial \rho}{\partial T}\right)_p$, results in the following:

$$\left(\frac{\partial \rho}{\partial T}\right)_p = \frac{Mp}{R}\left(-\frac{1}{T^2 Z} - \frac{1}{TZ^2}\left(\frac{\partial Z}{\partial T}\right)_p\right). \tag{D.18}$$

Eliminating the fractions inside of the brackets gives:

$$\left(\frac{\partial \rho}{\partial T}\right)_p = -\frac{Mp}{RT^2 Z^2}\left(Z + T\left(\frac{\partial Z}{\partial T}\right)_p\right). \tag{D.19}$$

After deriving $\left(\frac{\partial \rho}{\partial p}\right)_T$ and $\left(\frac{\partial \rho}{\partial T}\right)_p$ in terms of Z, in Equations D.16 and D.19 respectively. These relations are then substituted into Eq. D.13 yielding:

$$c^{-2} = \frac{M}{RTZ^2}\left(Z - p\left(\frac{\partial Z}{\partial p}\right)_T\right) - \frac{T}{\rho^2 c_p}\frac{M^2 p^2}{R^2 T^4 Z^4}\left(Z + T\left(\frac{\partial Z}{\partial T}\right)_p\right)^2. \tag{D.20}$$

Inserting Eq. D.15 for ρ^2 results in

$$c^{-2} = \frac{M}{RTZ^2}\left(Z - p\left(\frac{\partial Z}{\partial p}\right)_T\right) - \frac{1}{c_p T Z^2}\left(Z + T\left(\frac{\partial Z}{\partial T}\right)_p\right)^2. \tag{D.21}$$

Clearing up the right-hand side of the equations gives the following relation corresponding to Eq. 5.1.

$$c^{-2} = \frac{M}{RTZ^2}\left[\left(Z - p\left(\frac{\partial Z}{\partial p}\right)_T\right) - \frac{R}{c_p M}\left(Z + T\left(\frac{\partial Z}{\partial T}\right)_p\right)^2\right]. \tag{D.22}$$

The derivation of Eq. 5.2 originates from the need of an expression for the heat capacities, required for relating the speed of sound to an equation of state [7, 55]. For the isobaric heat capacity, the following relation is used:

$$c_p = c_{p,0} + \int_{p,0}^{p}\left(\frac{\partial c_p}{\partial p}\right)_T \mathrm{d}p, \tag{D.23}$$

where the differential $\left(\frac{\partial c_p}{\partial p}\right)_T \mathrm{d}p$ is expressed as:

$$\left(\frac{\partial c_p}{\partial p}\right)_T = -T\left(\frac{\partial^2 \rho^{-1}}{\partial T^2}\right)_p. \tag{D.24}$$

Expressing this relation in terms of compressibility coefficient requires the second derivative, $\left(\frac{\partial^2 \rho^{-1}}{\partial T^2}\right)_p$, given by:

$$\left(\frac{\partial^2 \rho^{-1}}{\partial T^2}\right)_p = \frac{R}{Mp}\left[2\left(\frac{\partial Z}{\partial T}\right)_p + T\left(\frac{\partial^2 Z}{\partial T^2}\right)_p\right]. \tag{D.25}$$

Inserting this back into Eq. D.24 yields:

$$\left(\frac{\partial c_p}{\partial p}\right)_T = -\frac{R}{Mp}\left[2T\left(\frac{\partial Z}{\partial T}\right)_p + T^2\left(\frac{\partial^2 Z}{\partial T^2}\right)_p\right], \tag{D.26}$$

which is Eq. 5.2.

Relations D.22 and D.26 need to be rewritten in order to be of use in the integration process. Equation D.22 is used in this process to determine the isobaric heat capacity. Rewriting Eq. D.22 requires c_p to be isolated on the left-hand side, this is given by:

$$c_p = \left[\frac{M}{R}\frac{\left(Z - p\left(\frac{\partial Z}{\partial p}\right)_T\right)}{\left(Z + T\left(\frac{\partial Z}{\partial T}\right)_p\right)^2} - \frac{TZ^2}{c^2\left(Z + T\left(\frac{\partial Z}{\partial T}\right)_p\right)^2}\right]^{-1}. \tag{D.27}$$

Similarly, Eq. D.26 requires isolation of $\left(\frac{\partial^2 Z}{\partial T^2}\right)_p$ on the left-hand side, in order to provide data for the integration steps, required for the determining the initial conditions at the next temperature step. This rewritten relation is given by:

$$\left(\frac{\partial^2 Z}{\partial T^2}\right)_p = -\frac{Mp}{RT^2}\left(\frac{\partial c_p}{\partial p}\right)_T - \frac{2}{T}\left(\frac{\partial Z}{\partial T}\right)_p. \tag{D.28}$$

The relations given by Equations D.27 and D.28 are used in the integration process to not only determine the values for c_p and $\left(\frac{\partial^2 Z}{\partial T^2}\right)_p$, but also for Z and $\left(\frac{\partial Z}{\partial T}\right)_p$ for the next temperature step.

Bibliography

[1] Airbus. Cities, airports and aircraft 2019-2038, 2019.

[2] G. Angelino. Multicomponent working fluids for organic rankine cycles (orcs). *Energy*, 23, 1998.

[3] G. Angelino and C. Invernizzi. Cyclic methylsiloxanes as working fluids for space power cycles. *Journal of Solar Energy Engineering*, 115, 1993.

[4] J. Bao. A review of working fluid and expander selections for organic rankine cycle. *Renewable and Sustainable Energy Reviews*, 24, 2012.

[5] G. Benedetto, R.M. Gavioso, and R. Spagnolo. Precision measurement of the speed of sound and thermodynamic properties of gases. *RIVISTA DEL NUOVO CIMENTO*, 22, 1998.

[6] H.A. Bethe. On the theory of shock waves for an arbitrary equation of state. *Classic Papers in Shock Compression Science*, 1942.

[7] M. Bijedic and S. Begic. Thermodynamic properties of vapors from speed of sound. *Journal of Thermodynamics*, 2014, 2014.

[8] Boeing. Commercial market outlook 2020–2039, 2020.

[9] P. Bombarda, C. Invernizzi, and M. Gaia. Performance analysis of otec plants with multilevel organic rankine cycle and solar hybridization. *Journal of Engineering for Gas Turbines and Power*, 135, 2013.

[10] W.E. Boyce and R.C. DiPrima. *Elementary Differential Equations and Boundary Value Problems*. Wiley, 10 edition, 2013.

[11] G.P. Brasseur, R.A. Cox, D. Hauglustaine, I. Isaksen, J. Lelieveld, D.H. Lister, R. Sausen, U. Schumann, A. Wahner, and P. Wiesen. European scientific assessment of the atmospheric effects of aircraft emissions. *Atmospheric Environment*, 32, 1998.

[12] P. Colonna. Multiparameter equations of state for selected siloxanes. *Fluid Phase Equilibria*, 244, 2006.

[13] P. Colonna and A. Guardone. Molecular interpretation of nonclassical gas dynamics of dense vapors under the van der waals model. *Phyiscs of Fluids*, 18, 2006.

[14] P. Colonna, E. Casati, C. Trapp, T. Mathijssen, J. Larjola, T. Turunen-Saaresti, and A. Uusitalo. Organic rankine cycle power systems: From the concept to current technology, applications, and an outlook to the future. *Journal of Engineering for Gas Turbines and Power*, 137, 2015.

[15] I.M.T. Davidson and J.F. Thompson. Kinetics of the thermolysis of octamethylcyclotetrasiloxane in the gas phase. *Journal of the Chemical Society*, 85, 1975.

[16] A.F. Estrada-Alexanders and D. Justo. New method for deriving accurate thermodynamic properties from speed-of-sound. *Journal of Chemical Thermodynamics*, 36, 2004.

[17] A.F. Estrada-Alexanders, J.P.M Trusler, and M.P. Zarari. Determination of thermodynamic properties from the speed of sound. *The International Journal of Thermoplastics*, 16, 1995.

[18] M.B. Ewing and J.P.M. Trusler. Speeds of sound in cf4 between 175 and 300 k measured with a spherical resonator. *The Journal of Chemical Physics*, 90, 1989.

[19] M.B. Ewing and J.P.M. Trusler. Interaction second acoustic virial coefficients (n 2 + ar) between 90 and 373 k. *Physica A*, 184, 1992.

[20] F.J. Fernandez. Thermodynamic analysis of high-temperature regenerative organic rankine cycles using siloxanes as working fluids. *Renewable and Sustainable Energy Reviews*, 36, 2011.

[21] K.A. Gillis. Thermodynamic properties of two gaseous halogenated ethers from speed-of-sound measurements: Difluoromethoxy-difluoromethane and 2-difluoromethoxy- 1,1, l-trifluoroethane. *International Journal of Thermophysics*, 15, 1994.

[22] A. R. H. Goodwin. Speed of sound measurements and heat capacities of gases. *Heat Capacities: Liquids, Solutions and Vapours*, 2010.

[23] A.R.H. Goodwin, K.N. Marsh, and W.A. Wakeham. *MEASUREMENT of the THERMODYNAMIC PROPERTIES of SINGLE PHASES*. Elsevier, 2003.

[24] M.M.A. Hussein. Sound speed measurement using photoacoustic effect. *INDIAN JOURNAL OF APPLIED RESEARCH*, 4, 2014.

[25] U. Ingard. On the theory and design of acoustic resonators. *Journal of the Acoustical Society of America*, 25, 1953.

[26] Y. Kano, Y. Kayukawa, and K. Fujii. Ideal gas heat capacity derived from speed of sound measurements in the gaseous phase for trans-1,3,3,3-tetrafluoropropene. *Journal of chemical & engineering data*, 58, 2013.

[27] T. Kottas, M.N. Bozoudis, and M.A. Madas. Turbofan aero-engine efficiency evaluation: An integrated approach. *Omega*, 92, 2020.

[28] A.J.X. Lim, M.B.C. Khoo, W.L. Teoh, and A. Haw. Run sum chart for monitoring multivariate coefficient of variation. *Computers and Industrial Engineering*, 109, 2016.

[29] K. Lovegrove and J. Pye. *Concentrating Solar Power Technology*, chapter 2. Woodhead Publishing Series in Energy. Elsevier, 2020.

[30] T. Mathijsen, M. Gallo, E. Casati, N. R. Nannan, C. Zamfirescu, A. Guardone, and P. Colonna. The flexible asymmetric shock tube (fast): a ludwieg tube facility for wave propagation measurements in high-temperature vapours of organic fluids. *Experiments in Fluids*, 56, 2015.

[31] I.A. McLure and J.F. Neville. The critical temperatures and pressures of hexamethyldisilmethylene, octamethylcyclotetrasiloxane, and decamethylcyclpentasiloxane. *Journal of Chemical Thermodynamics*, 14, 1982.

[32] J.B. Mehl. Spherical acoustic resonator: Effects of shell motion. *The Journal of Acoustical Society of America*, 78, 1985.

[33] K. Meier. *The Pulse-Echo Method for High Precision Measurements of the Speed of Sound in Fluids*. PhD thesis, Helmut-Schmidt-University – University of the Federal Armed Forces Hamburg, 2006.

[34] B. Mercier, N.B. Chandrasekaran, and P. Colonna. A novel acoustic resonator for speed of sound measurement in dense organic vapours. In *3rd International Seminar on Non-Ideal Compressible Fluid Dynamics for Propulsion & Power*, 2020.

[35] M.R. Moldover, J.B. Mehl, and M. Greenspan. Gas-filled spherical resonators: Theory and experiment. *The Journal of Acoustical Society of America*, 79, 1986.

[36] M.R. Moldover, J.P.M. Trusler, and T.J. Edwards. Measurement of the universal gas constant r using a spherical acoustic resonator. *Physical Review Letters*, 60, 1988.

[37] M.E. Mondéjar, M.O. McLinden, and E.W. Lemmon. Thermodynamic properties of trans-1-chloro-3,3,3-trifluoropropene (r1233zd(e)): Vapor pressure, (p, ρ, t) behavior, and speed of sound measurements, and equation of state. *Journal of Chemical and Engineering data*, 60, 2015.

[38] M.J. Moran, H.N. Shapiro, D.D. Boettner, and M.B. Bailey. *Fundamentals of Engineering Thermodynamics*. Wiley, 8 edition, 2014.

[39] D.M. Moss and K. Cornely. Determination of the universal gas constant, r. *Journal of Chemical education*, 78, 2001.

[40] N.R. Nannan. Ideal-gas heat capacities of dimethylsiloxanes from speed-of-sound measurements and ab initio calculations. *Fluid Phase Equilibria*, 257, 2007.

[41] NIST. Reference fluid thermodynamic and transport properties database. `https://www.nist.gov/srd/refprop`, 2020.

[42] J.E. Penner, Intergovernmental Panel on Climate Change. Working Group III., and Intergovernmental Panel on Climate Change. *Aviation and the Global Atmosphere*. Intergovernmental Panel on Climate Change, 1999.

[43] R.A. Perkins and M.O. McLinden. Spherical resonator for vapor-phase speed of sound and measurements of 1,1,1,2,2,3,3-heptafluoro-3-methoxypropane (re347mcc) and trans-1,3,3,3-tetrafluoropropene [r1234ze(e)]. *The Journal of Chemical Thermodynamics*, 91, 2015.

[44] V.S. Reddy, S.C. Kaushik, S.K. Tyagi, and N.L. Panwar. An approach to analyse energy and exergy analysis of thermal power plants: A review. *Smart Grid and Renewable Energy*, 1, 2010.

[45] W.C. Reynolds and P. Colonna. *Thermodynamics Fundamentals and Engineering applications*. Cambridge University Press, 2018.

[46] R. Sausen and U. Schumann. Estimates of the climate response to aircraft CO2 and NO(x) emissions scenarios. *Climatic Change*, 44, 2000.

[47] A. Schuster. Energetic and economic investigation of organic rankine cycle applications. *Applied thermal engineering*, 29, 2009.

[48] C.E. Smit, C.J.A.M. Posthuma-Doodeman, and E.M.J. Verbruggen. Environmental risk limits for octamethylcyclotetrasiloxane in water. Technical report, Dutch Ministry of Health, Welfare and Sport, 2012.

[49] R. Span. Simultaneous optimization as a method to establish generalized functional forms for empirical equations of state. *International Journal of Thermophysics,*, 19, 1998.

[50] R. Span and W. Wagner. Equations of state for technical applications. i. simultaneously optimized functional forms for nonpolar and polar fluids. *International Journal of Thermophysics*, 24, 2003.

[51] M. Suchenek and T. Borowski. Measuring sound speed in gas mixtures using a photoacoustic generator. *International Journal of Thermophysics*, 39, 2018.

[52] P. A. Thompson. A fundamental derivative in gasdyanamics. *The Physics of Fluids*, 14, 1971.

[53] P.A. Thompson and K.C. Lambrakis. Negative shock waves. *The Journal of Fluid Mechanics*, 60, 1973.

[54] J. P. M. Trusler and M. Zarari. The speed of sound and derived thermodynamic properties of methane at temperatures between 275 k and 375 k and pressures up to 10 mpa. *J. Chem. Thermodynamic*, 24, 1992.

[55] J.P.M. Trusler. *Physical Acoustics and Metrology of Fluids*. Adam Hilger, 1991.

[56] C.L. Young. Equilibrium properties of octamethylcyclotetrasiloxane near its critical point and applicability of the principle of corresponding states. *Journal of Chemical Thermodynamics*, 4, 1972.

[57] H. Yu, G.D.A. Giuliani, and G.A. Csáthy. An acoustic resonator with a closed geometry. *American Journal of Physics*, 84, 2016.

[58] X. Zheng, Y. Zhang, and M. He. Speed of sound measurement in ethyl tert-butyl ether and tert-amyl methyl ether by brillouin light scattering. *Fluid Phase Equilibria*, 1, 2015.